Aalborg Universitet
Masters Thesis
Water and Environmental Engineering

Hydraulic Capacity of Meandering Streams

Authors:
Igor Nepela
Mads Leth-Wahl
Tomás Visciarelli Eroles

Supervisors:
Torben Larsen
Jesper Ellerbæk Nielsen

June 9, 2023

AALBORG UNIVERSITY
STUDENT REPORT

Department of the Built Environment
Water and Enviromental Engineering
Thomas Manns Vej 23
9220 Aalborg Ø
https://www.en.build.aau.dk/

Title: Hydraulic Capacity of Meandering Streams

Project: Masters Thesis
Period: September 2022 - June 2023
Project group: build-22-vm-8-3

Supervisors:
Torben Larsen
Jesper Ellerbæk Nielsen

Authors:
Igor Nepela
Mads Leth-Wahl
Tomás Visciarelli Eroles

Pages: 101
Appendix: 26

Synopsis:

An important factor in maintaining the balance between sustaining a healthy biome in Danish streams and ensuring adequate drainage and prevention of flooding depends on the degree of curvature allowed in meandering streams. This study aims to describe the impact of the degree of curvature on the resistance to flow in a stream through a series of analytical and numerical methods, as well as investigate the pros and cons of two methods for measuring hydraulic parameters in streams. Both the Propeller Current Meter and the Acoustic Doppler Current Profiler (ADCP) were found to return similar results, although the data obtained using the ADCP was found to be more versatile and useful in the analyses carried out further on in the project. Data obtained from Binderup Å was used in a series of analytical and 1-D modelling approaches, where the resistance to flow was found to be higher in the meandering section of the stream by up to 39%, although this difference was found to be lower under low-flow conditions. To isolate the effect of the curvature of a meander, a series of flat-bedded channels with varying curvatures were modelled in the CFD program Star CCM+. Although the hydraulic structures were not directly comparable with a natural stream, the results showed that increasing degrees of curvature led to increased resistance to flow.

Preface

This Master's thesis was conducted by a group of 4^{th} semester students on the Master's Degree of Water & Environmental Engineering at Aalborg University under the guidance of Torben Larsen, professor at the Department of the Built Environment and Jesper Ellerbæk Nielsen, associate professor at the Department of the Built Environment.

We would like to express our sincere appreciation to the individuals and organizations whose contributions made this thesis possible.

First and foremost, we would like to extend our deepest gratitude to our supervisors, Torben and Jesper, for their guidance, expertise, and unwavering support throughout the duration of this study. Their valuable insights and constructive feedback significantly influenced the direction and quality of our research.

We are also thankful to Lasse Lehm of Aalborg Municipality for providing us with relevant data and information relating to the project site. Additionally, we would like to give a big thank you to Uffe Westerberg and Lystfiskeriforeningen Binderup Å for their generosity in providing us with access to their cabin so we could get some shelter during some very cold days in the field. Their hospitality and assistance created a conducive environment for our data collection and analysis, and we are truly grateful for their cooperation.

Last but not least, we would like to express our appreciation to Morten Lauge Fejerskov for setting aside his time and expertise to train us in the use of the ADCP. His guidance and hands-on training were vital in enabling us to collect accurate and reliable data for our research.

Once again, our heartfelt appreciation goes out to everyone who played a part in this thesis, directly or indirectly. Your contributions have been invaluable, and we are sincerely grateful for your support.

Contents

List of Abbreviations and Symbols

A	Cross-sectional area
ADCP	Acoustic Doppler Current Profiler
a.s.l.	Above sea level
C	Curvature
CFD	Computational fluid dynamics
Fr	Froude number
g	Gravitational acceleration
h	Water depth
HEC-RAS	Hydrologic Engineering Center's River Analysis System
h_m	Hydraulic mean depth
h_v	Velocity head
I	Energy gradient
K	Conveyance
M	Manning's number (inverse of n)
MBS	Mesh base size
MSE	Mean square error
n	Manning's roughness coefficient
NSE	Nash-Sutcliffe efficiency
P	Wetted perimeter
Q	Volumetric flow
R	Hydraulic radius
RANS	Reynolds Averaged Navier-Stokes
Re	Reynolds number
TS	Time step
v	Average velocity
VMT	Velocity Mapping Toolbox
VOF	Velocity of Fluid
WSE	Water surface elevation
α	Velocity distribution coefficient

1 Introduction

1.1 Historical framework of Danish streams

Rich biodiversity is an important social, economic and ecological factor, with many social clubs and hobbies, each with its associated industry, relying on a healthy biosphere. For example, the recreational fishing industry in Denmark was worth a total of DKK 2.9 billion in 2010 alone, with foreign tourists contributing an estimated DKK 275 million while employing 2,473 people [Jacobsen, 2010]. This, of course, relies on healthy fish populations in Danish streams, making it important to ensure the availability of suitable habitats for these socioeconomically important organisms.

During the 1800s and up until the late 1960s, at least 90% and up to 97% of streams in Denmark were modified to maximise flow capacity, drainage, and farmable land area, in an effort to optimise the agricultural sector [Miljøstyrelsen; Brookes, 1990; Hofmeister, 2012]. This increased capacity was achieved by reducing the resistance to flow in a stream through the straightening and deepening of channels as well as cutting vegetation along the banks. This, however, proved to have detrimental effects on the ecological systems in and around these water bodies [Miljøstyrelsen].

The restoration of previously channelised waterways to their natural meandering state has, however, been shown to effectively improve biodiversity [Pedersen et al., 2005], which is precisely what the 'Vandløbslov' (English: 'Stream Law') of 1982 was introduced to achieve. This law aimed to restore the natural condition of many of the previously channelised streams in Denmark, enforcing measures that aim to maintain both the flow capacity and biodiversity. This included reducing the trimming of vegetation along stream banks, restoring streams to a more natural meandering shape, and ensuring the shape of streams would not be artificially altered. Additionally, 28,000 of the 64,000 kilometres of streams in Denmark are protected by the 'naturbeskyttelseslov' (English: Nature Protection Law) § 3, which prevents changes to the condition of the water body, aside from routine maintenance. This regular maintenance includes some cutting of vegetation, but in a way that ensures that the shape and particularly the flow capacity remains unchanged [Miljøstyrelsen].

In order to describe the physical quality of a stream, the Danish Physical Index is utilized. The index is based on assessments of a number of physical parameters, such as the degree of meandering, cross-sectional shape, width variation, stream velocity, and grain size distribution, among others, in and around the stream. Then, the physical quality can be estimated on the basis of the values for the individual parameters and their weight in the index [Wiberg-Larsen and Kronvang, 2016].

In a larger context, the EU Water Framework Directive, in place since 2000, has the objective of restoring and protecting the condition of water bodies throughout the EU.

Specifically, it aims at achieving a 'good' chemical and ecological status in bodies of water ranging from coastal waters to groundwater aquifers. This involves maintaining hydro-morphological quality, including stream bank structure, continuity and substrate, maintaining healthy populations of fish, invertebrates and flora, as well as identifying and monitoring pollutants to achieve a set of objectives set by the individual member states.

1.2 Physical and biological factors contributing to biodiversity

There is indeed a complex set of interactions between physical, chemical, and biological components making up the ecological systems around these waterways. These systems depend on heterogeneous conditions [Verdonschot and Nijboer, 2002; Brookes, 1990], one major aspect of which is hydraulic complexity. This can be effected by a range of factors such as diverse vegetation and irregularities in the streambed topography, as illustrated in Figure 1.1.

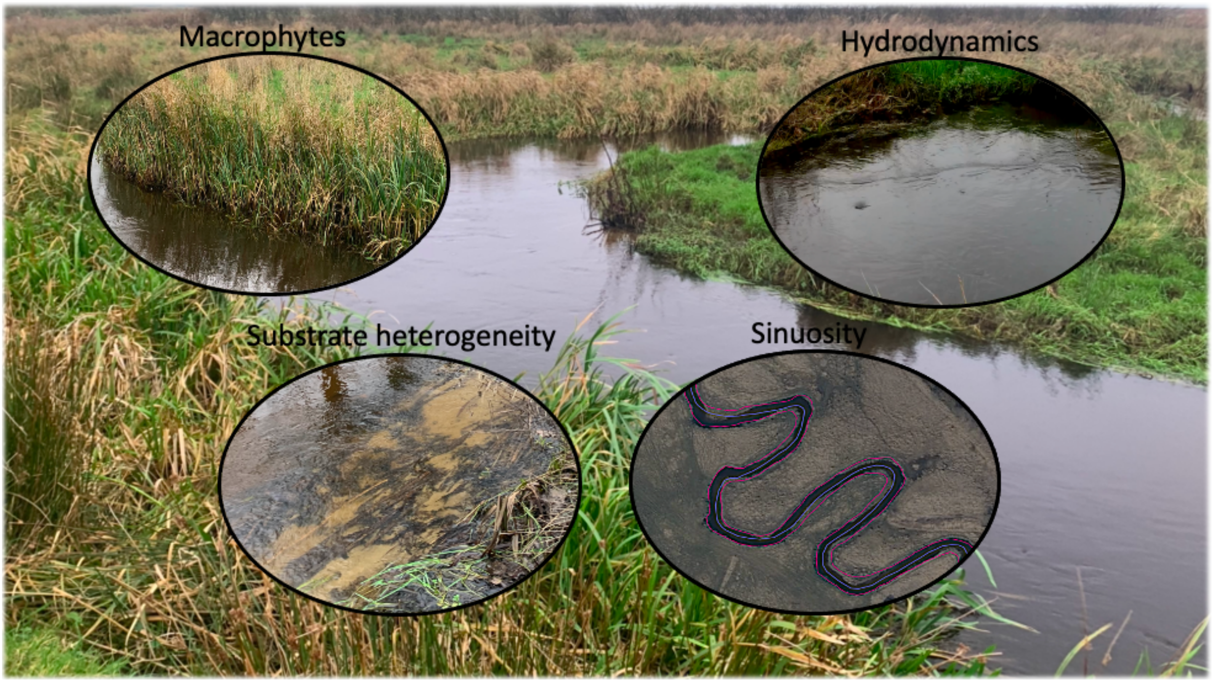

Figure 1.1. Overview of the physical and biological components

Different macrophytes prefer different flow velocities, depths, and substrate types [Chambers et al., 1991], all of which are homogenised as a result of channelisation, leading to a less diverse macrophyte community profile [Baattrup-Pedersen and Riis, 1999]. Macrophytes significantly impact the physical conditions of a stream, increasing the hydraulic complexity in a stream by reducing the current velocity in the areas in which the macrophytes are growing, commonly referred to as the macrophyte stands. This increases sedimentation of fine particles in these areas while increasing velocity around the stands, which can increase sediment transport, leaving behind coarser substrate types around the stands [Champion and Tanner, 2000; Jensen and Mebus, 1996]. This increased substrate heterogeneity has shown to be directly correlated with increased macroinvertebrate diversity in natural streams [Pedersen et al., 2014].

Similarly, certain fish prefer specific hydraulic conditions to thrive. For example, fish such as brook and brown trout prefer resting positions, or "focal points", with low velocities where minimum energy expenditure is required to stay in position, but adjacent to a high velocity gradient to areas where high units of feed are carried [Fausch and White, 1981; Hayes and Jowett, 1994].

1.3 Hydraulic complexity and Manning's roughness coefficient

The hydraulic complexity of a stream is also impacted by the degree of meandering of the reach. As the water flows along the curves of a meander reach, the water at the outer bank circulates at a larger velocity than at the inner bank. As a result, sediments are transported downstream from high velocities zones, known as pool zones, towards more calm zones of sedimentation called point bars [Ferguson and Parsons, 2003]. Over time, the combined action of erosion of the outer bank and deposition at the inner bank produced the migration of the bends in the outer bank direction.

Inside a bend, the velocity distribution acquires a complex three-dimensional profile due to the combined action of various forces. As the water enters a bend, two opposite mechanisms take place. The centrifugal forces, proportional to the squared velocity, and the centripetal pressure gradient generated by the transverse water surface slope. These combined effects produce the water in the upper part of the water column to move towards the outer bank and the water close to the bottom to be pushed towards the inner bank. Overall, a transversal secondary flow circulation path through the river bend [Ottevanger, 2013].

Close to the bed, the velocity loses some of its momentum at a greater rate due to friction forces than at the surface. This differential effect of the centrifugal forces on the water at the surface and near the bed causes a secondary flow circulation down along the outside bank, along the bottom of the streambed towards the inside of the bend, and up and back across to the outside along the water surface, as illustrated in Figure 1.2. This creates a helical corkscrew pattern following the length of the meander. In some instances, a smaller cell of secondary flow can be observed towards the outer bank rotating in the opposite direction to the larger central cell as illustrated in Figure 1.2.

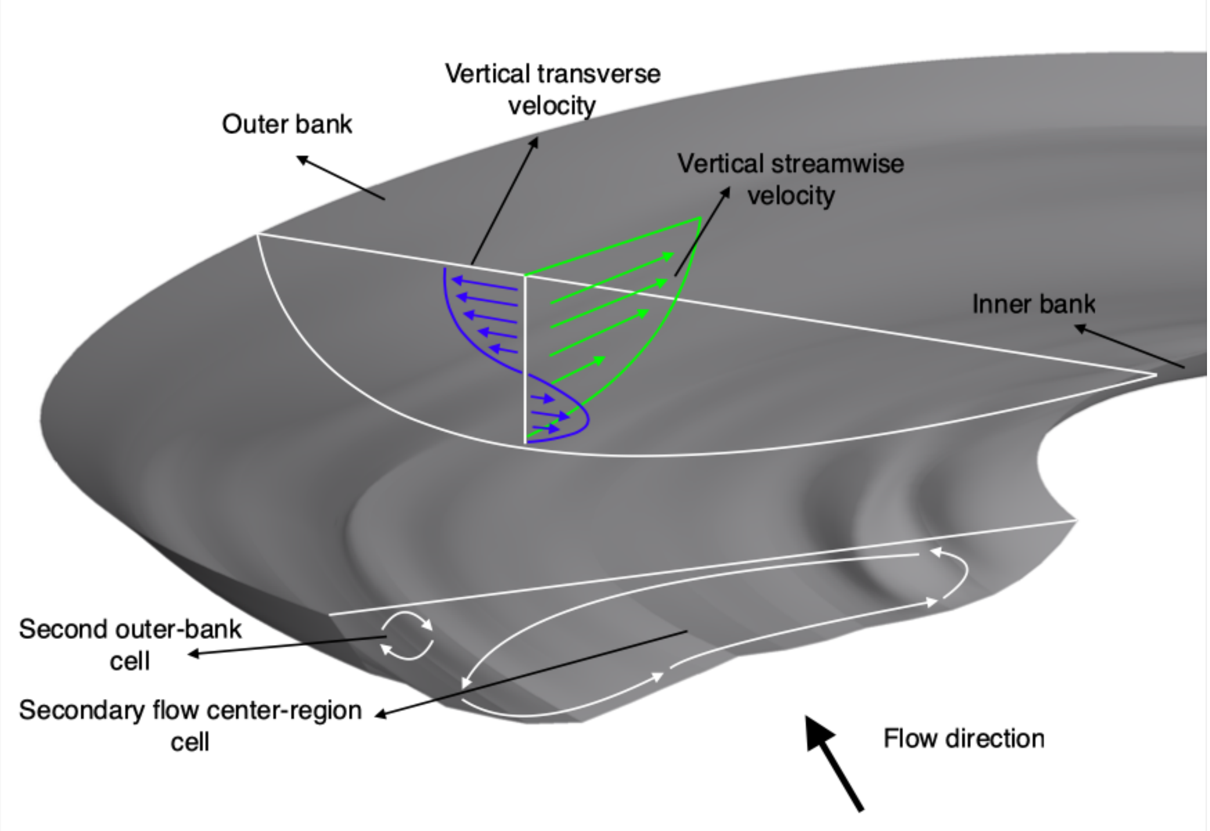

Figure 1.2. Definition sketch of curved open-channel flow and illustration of velocity decomposition.

The aforementioned point bar has an important role in the distribution of the stream-wise velocities along the bend through a process called topographic steering. This process forces the flow around the point bar, generating a redistribution of the momentum towards the outer bank, increasing the velocity [Ottevanger, 2013], as shown in plane B-B' of Figure 1.3. The turbulence generated by irregularities in a stream bed comes in the form of eddies which impart kinetic energy against the direction of flow. Under turbulent conditions, higher velocities lead to increased eddy viscosity in the near-wall region, increasing the amount of wall shear stresses and, thereby, the kinetic energy being imparted against the direction of flow [Blanckaert, 2010].

This process is enhanced by a rise in water level outwards of the bend, which generates an area of higher pressure compared with the inner bank. In the inner bank after the apex, the water level rises as a consequence of the flattening of the transverse slope. Therefore, a low-pressure zone appears immediately following the point bar, and the horizontal velocity gradient inflects, as seen in plane C-C' of Figure 1.3, causing a zone of horizontal recirculation and the formation of eddies [Zhou and Endreny, 2020].

This recirculation zone is important for the trapping of sediments and as an area for animals to shelter. Sediment accumulation occurs due to the combined effect of low velocities and secondary flow that tends to concentrate the sediments at the centre of the recirculation zone [Zhou and Endreny, 2020].

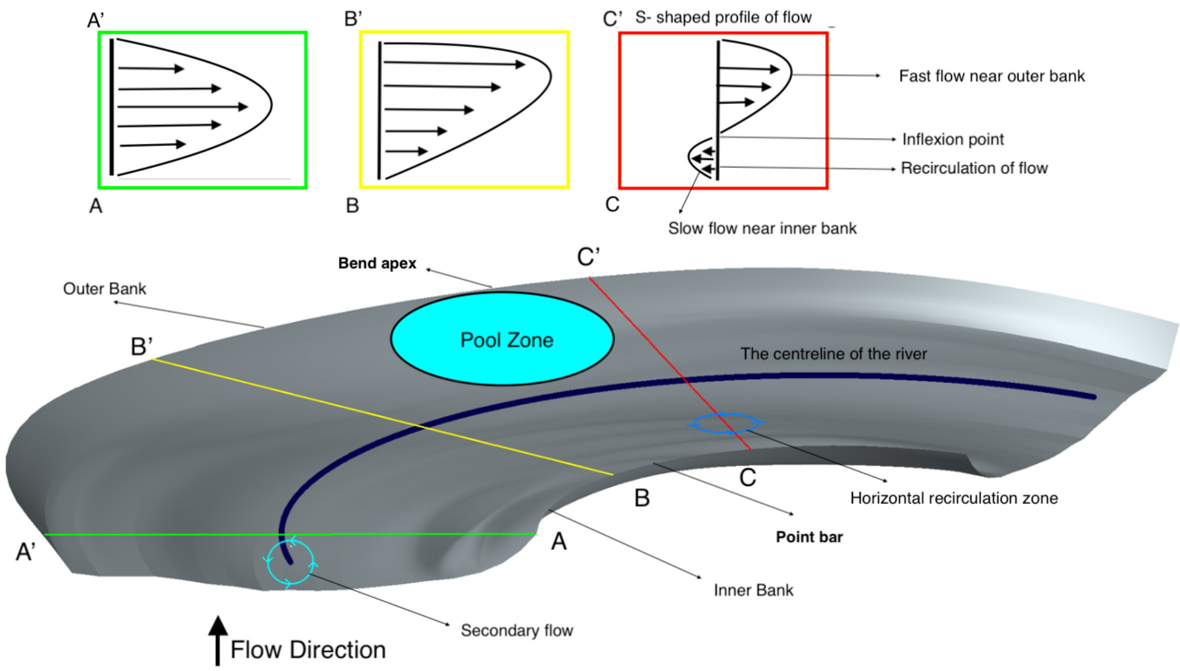

Figure 1.3. Schematic overview of processes and features in meandering channels, with schematic top view of typical velocities distribution.

The estimated resistance to flow in a stream system is defined by Manning's roughness coefficient n. Many parameters can be accounted for in determining this number, some being more important than others when considering a natural stream.

All of these components of a stream, from the type of vegetation, substrate, and changes in cross-sectional area and shape, either due to bending or other obstructions, contribute to resistance to flow in the stream. This resistance is characterised by the Manning's roughness coefficient, n, which is used in various calculations related to hydraulic engineering, such as flood discharge, velocity distribution, determining energy losses, the design of structures and ecological habitat prediction [Chow, 1959]. It is defined by the Manning's Equation, 1.1, assuming uniform steady-state flow, where water surface slope, friction slope and energy gradient are parallel to the stream bed and the area, hydraulic radius, and depth remain relatively constant throughout the stream reach.

$$Q = \frac{1}{n} \cdot A \cdot R^{2/3} \cdot I^{1/2} \tag{1.1}$$

Q	Discharge $[m^3/s]$
n	Roughness coefficient $[s^3/m^{1/3}]$
A	Cross-sectional area $[m^2]$
R	Hydraulic Radius $[m]$
I	Energy gradient

Although it is possible to identify the factors affecting the total resistance, the individual contributions of each individual parameter to n are difficult to quantify [Coon, 1997].

One of the early studies that attempted to do this was carried out by Cowan [1956], who proposed a general approach according to the equation 1.2.

$$n = (n_0 + n_1 + n_2 + n_3 + n_4) * m \tag{1.2}$$

This method consists of a base n value (n_0), followed by a series of modifying values to account for cross-sectional variations (n_1), size and shape variations (n_2), surface irregularities and obstructions (n_3), the type and density of vegetation (n_4) and finally the sinuosity of the stream (m). Each of these values are evaluated subjectively based on a series of look-up tables with standardised descriptions and values.

Several methods with similar aims have emerged since. Frasken [1963] proposed a method for accounting for meander losses by adjusting the basic n value on the basis of sinuosity, while Limerinos [1970] proposed a method that considered the stream bed-particle size and size distribution, and hydraulic radius. Bray [1979] developed an equation that relates n to water surface slope alone. The selected sites had almost no vegetation in the channel bed and minimal sediment transport.

For high-gradient mountain streams, Jarrett [1984] related the roughness coefficient with the energy gradient and hydraulic radius of the stream. This equation is applicable to channels with energy gradients from 0.002 to 0.09 and a hydraulic radius from 0.15 to 2.15 m. Jarrett and Petsch Jr. [1985] in cooperation with the U.S. Geological Survey developed a method that considered changing cross-sectional areas and channel shape.

Shiono et al. [1999] developed a model to predict discharge by considering Manning's coefficient in the case of longitudinal slope and the meandering effect of the channel. Khatua et al. [2011] formulated a mathematical equation for roughness coefficients by varying the sinuosity and geometry of the meandering compound channel, while Dash and Khatua [2016] modelled Manning's roughness coefficient by considering the width to depth ratio, viscosity, the slope of the bed, and sinuosity.

Besides these methods of estimating the roughness coefficient based on the physical condition of the stream, it can also be estimated by field measurements of discharge and water level using Manning's equation [Kim et al., 2010].

The three-dimensional nature of the flow and the non-uniform distribution of wall shear stress caused by the free surface and secondary currents can lead to variability in the roughness coefficient across the channel [Chow, 1959; Bilgil and Altun, 2008], making it difficult to determine their precise discharge capacity [Lai et al., 2008]. Furthermore, many factors contributing to roughness are dynamic and can change over time, further complicating the estimation of the roughness coefficient in open-channel flow [Doncker et al., 2009].

These studies have all attempted to provide a more accurate and precise way to estimate the roughness coefficient for open channel flows in both straight and meandering channels. However, disagreements about the best way to estimate n exist among researchers nowadays. The selected method should be carefully thought out, taking into consideration the particularities of the stream under study [Ferguson, 2010]. Moreover, slight variations in the n values can significantly change the calculated discharge and water levels, especially in small streams [Kim et al., 2010]. Consequently, careful attention should be paid to the selection of the method and relevant uncertainties should be considered when estimating n values.

Problem Statement 2

In Denmark, meandering streams were straightened in the 19th century to improve their capacity and reduce the risk of flooding. However, with increased public awareness of the importance of biodiversity in the Danish ecosystem, efforts were made in the 20th century to return the streams to their meandering form in order to provide suitable habitats for native fish and other invertebrates. The restoration of these habitats not only benefits the local ecosystem but also has a positive impact on the fly-fishing industry and tourism. However, these actions lead to a decrease in the flow capacity of the streams, leading to an increased risk of flooding.

This study aims to evaluate the impact of the curvature of meanders on the resistance to flow by determining Manning's roughness coefficient n through various methods, including both analytical and numerical approaches.

Additionally, the accuracy and reliability of measurement instruments will be assessed while comparing their strengths in attaining insights into hydraulic behaviour in a bend.

How does the curvature of a meandering stream contribute to Manning's roughness coefficient (n) ?

- How reliable and accurate are the Propeller Current Meter and Acoustic Doppler Current Profiler (ADCP) in collecting data in meandering sections of a stream, and what are the advantages of each method?
- What are the limitations of using Manning's equation for natural streams, and how does the NCALC method provide a more comprehensive analytical approach?
- How can the 1-D HEC-RAS model, incorporating detailed bathymetry and ADCP measurements, be used to estimate n value?
- How can CFD modelling be used to isolate the effect of curvature on n in meandering streams?

3 Methodology

Various methods and approaches were employed to evaluate Manning's roughness coefficient and understand the hydraulic behaviour of the meandering stream. The following is a summary of the reasons behind the choice of these methods and the expected outcome of each, along with the overall structure illustrated in Figure 3.1:

- Chapter 4 provides a description of the project site and information relevant to the outcome of the project, as well as an overview of the project site selection process. The objective was to identify a well-suited site that would fulfill the essential requirements for data collection, analysis, and experimentation, utilizing instruments like the Propeller Current Meter and Acoustic Doppler Current Profiler under varying flow conditions.
- Chapter 5 presents the methodology for assessing the accuracy and reliability of the ADCP compared to the conventional propeller current meter. Three different software were introduced to efficiently process raw data measurements collected by the ADCP. The goal was to compare various parameters such as bathymetry, flow measurements, and water velocity in both meandering and straight reaches of the stream to ensure the accuracy of the ADCP data for further use.
- Chapter 6 includes the process of determining Manning's roughness coefficient in natural streams using the numerical one-dimensional hydraulic model developed in HEC-RAS and analytical Manning's and NCALC equations. The limitations of using Manning's equation for natural streams were considered. Therefore, the USGS's NCALC method was introduced as a more comprehensive analytical approach, as the method considers variation in cross-sectional area. Moreover, the ADCP measurements of bathymetry and flow were utilized to construct and validate the 1-D HEC-RAS model, which considers detailed bathymetry measurements and terrain elevation data. The objective was to estimate Manning's roughness coefficient n by the three methods between straight and meandered sections.
- Chapter 7 investigates how simplified three-dimensional models with varying curvatures can be used to understand the effect of bending on Manning's roughness coefficient. The Star CCM+ software was utilized for modelling, enabling a detailed examination of hydraulic behaviour, including turbulence, water displacement within the bend, and complex flow patterns. The primary objective of this chapter was to compare the obtained results of n value and velocity profiles with the theory.

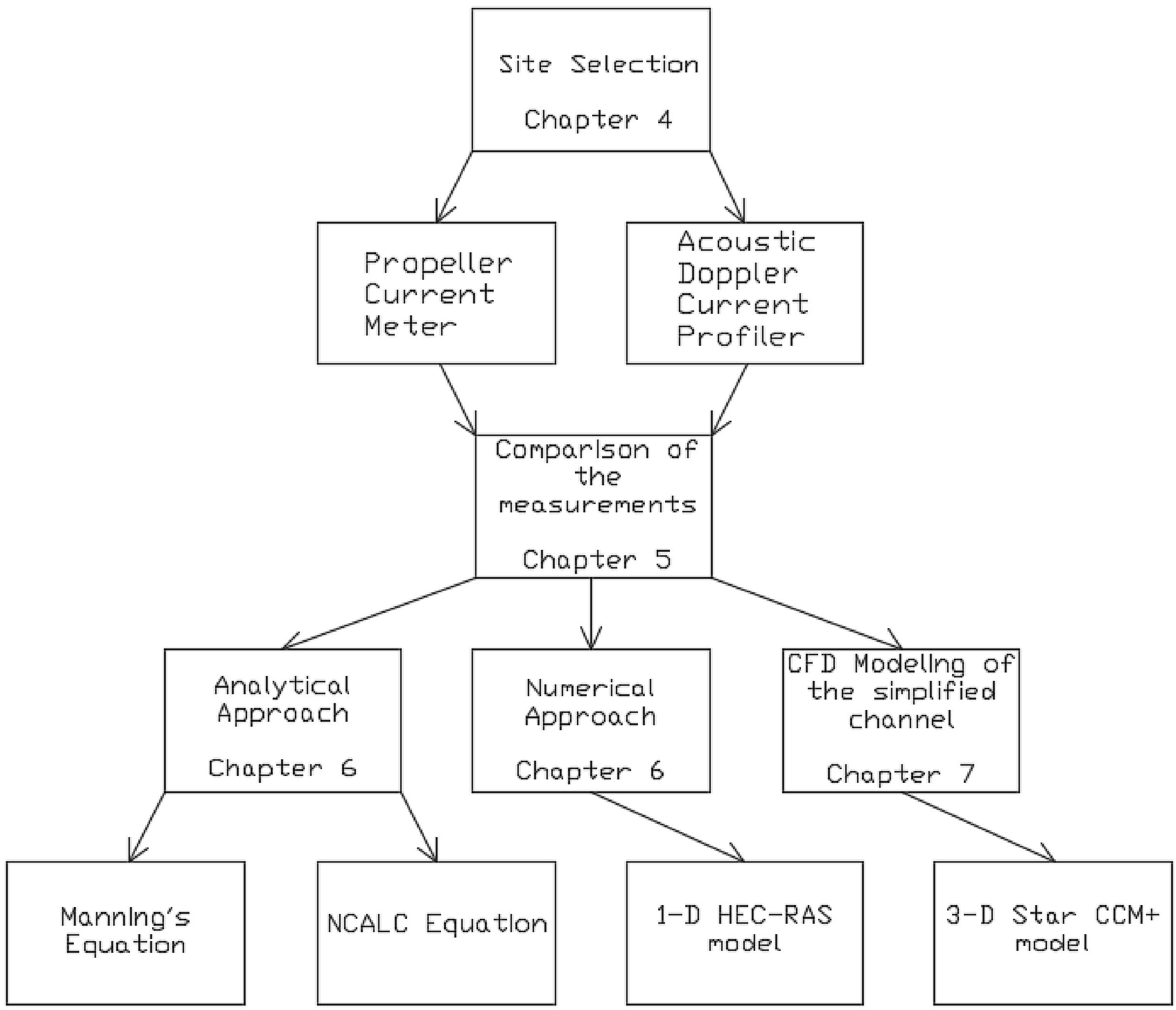

Figure 3.1. Overall structure of the project going forward, where the different chapters are illustrated in the figure.

Project Site: Binderup Å 4

The process of selecting the project area included consideration of multiple factors, including the presence of both meandering and straight sections of stream and the proximity to Aalborg University. Additionally, the availability of information from previous studies, such as an analysis by the engineering consultants WSP [Madsen, 2021a], could be used to gain a better understanding of the area and any potential challenges or opportunities that might have arisen during the project. In addition, available data from WSP and Miljøstyrelsen and measured during field days were analysed.

4.1 Background information about Binderup Å

The project site is an approximately 520-meter-long stretch of the stream Binderup Å, approximately 500 meters south of the outlet to the Limfjord, as shown in Figure 4.1. It is located off Klitgårdvej in a secluded agricultural area in the municipality of Aalborg in northern Denmark, east of Nibe Bredning. Two water level stations are placed near the site, which were be used to collect reference data. The first of these is St. 10.17, run by Miljøstyrelsen and placed near Binderup Mølle, approximately 750 metres south of the site. The second water level station is placed at the upstream end of the project site and is maintained by the municipality. This station will be referred to as 'Cabin St.' due to its close vicinity to the local fishing club's cabin. As Binderup Å flows north towards the Limfjord, it passes through chalk deposits, patches of forest, bogs, hills, and open expanses. The stream has an average winter flow of 12 $l/s/km^2$ and a catchment area of 82.6 km^2 at Binderup Mølle and 92.6 km^2 at the outlet to the Limfjord [Madsen, 2021b].

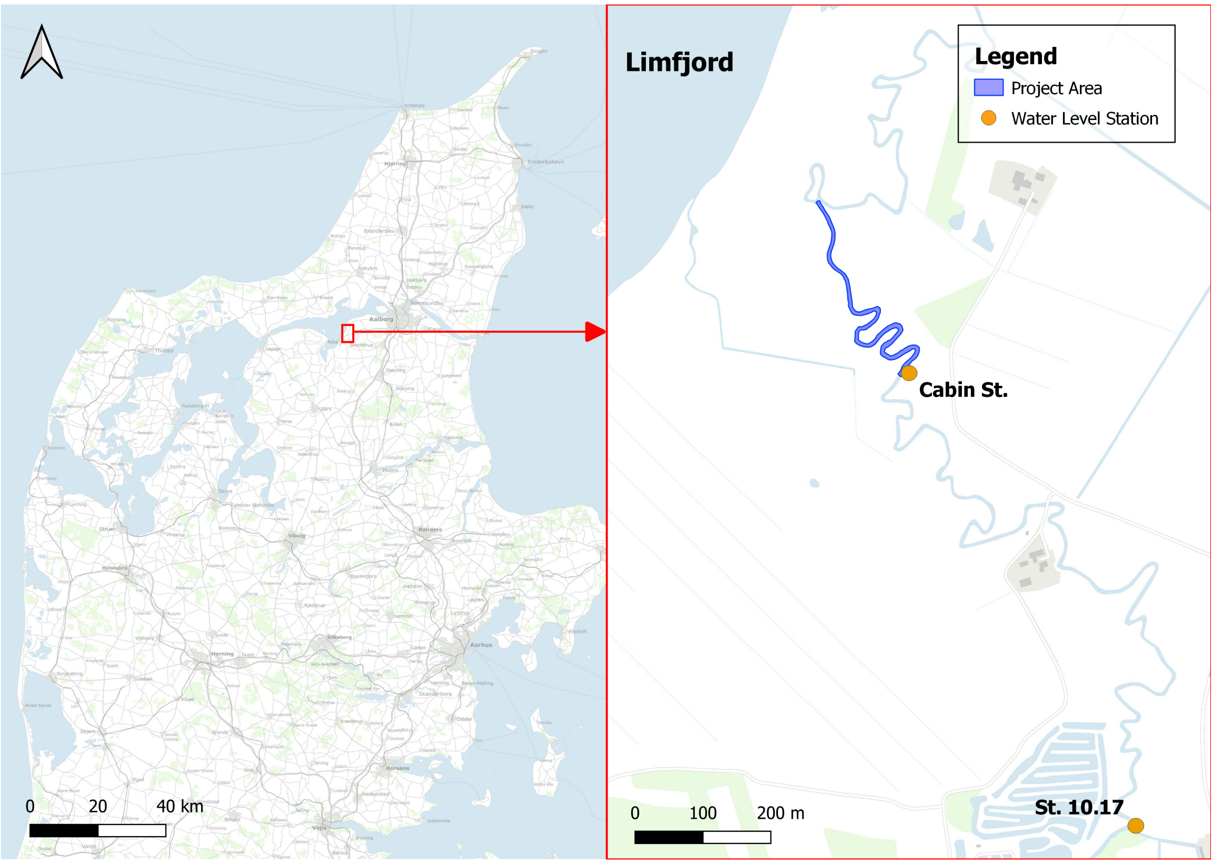

Figure 4.1. Location of the project site (blue shaded area) and water level stations (yellow dots).

Figure 4.2 shows a comparison of aerial photos from 1954 and 2020, revealing that the project area has undergone significant changes over this period. Due to the poor soil conditions and frequent flooding, the area has not been used for farming. Therefore, it is unlikely that human intervention has been a major contributor to the changes to the stream.

The aerial photos allow to observe the morphological changes suffered by the steam over the years. In the one from 1954, it can be observed that the stream has changed from a more meandered shape towards a straighter at the most downstream part of the project site. In the year 2020, upstream meanders have been moved in the outer bank direction. Also, an oxbow lake was generated at the end of the project site reach.

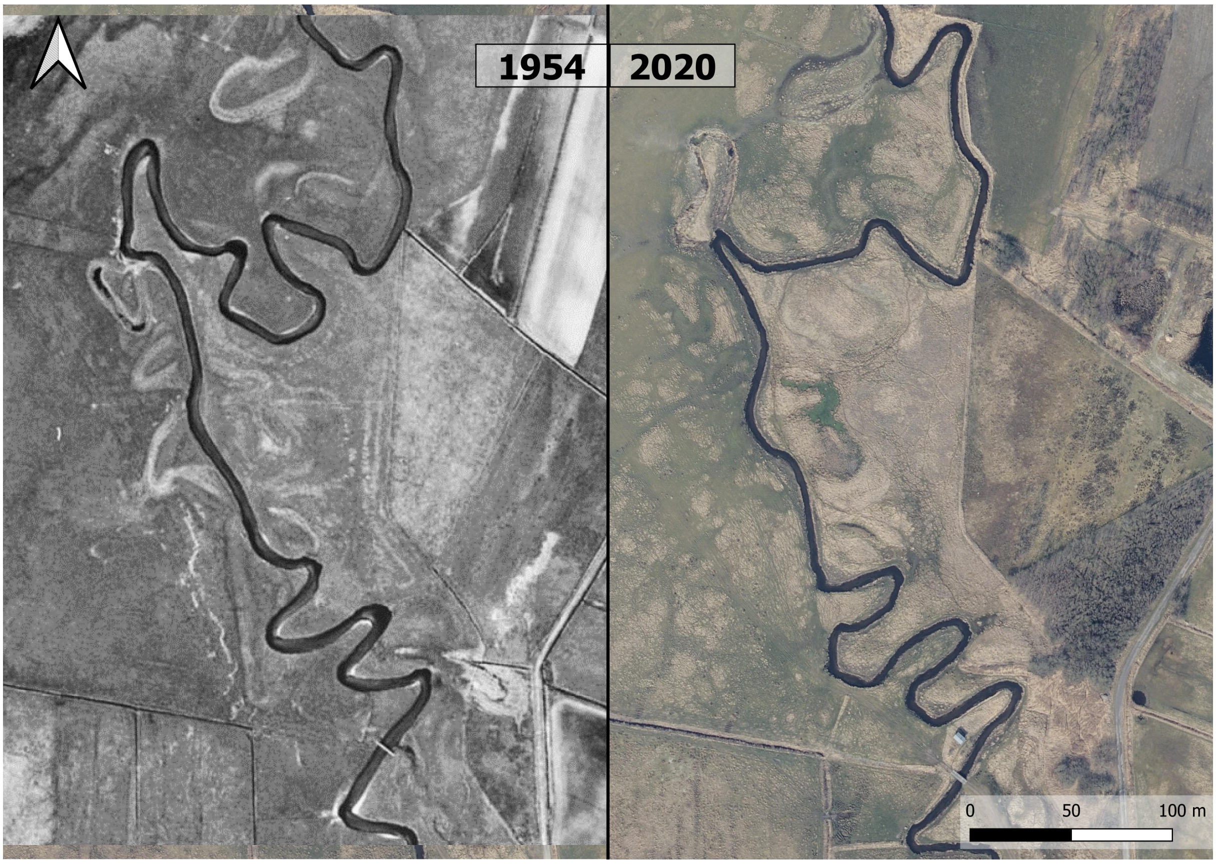

Figure 4.2. Aerial photos of the project area in 1954 and 2020.

WSP's analysis from 2021 focused on the stream's flow condition and any changes that occurred between 2001 and 2021. The analysis provides the stream's width, depth, slope, and flow capacity information. The width of the stream was found to vary significantly over short distances, ranging from approximately 3 to 6 meters, with depths varying from 40 centimetres and up to approximately 1.5 meters. The energy gradient was measured to be 0.7‰from the downstream end of the project site and upstream 2 kilometres, while in the lower section of the stream, from the downstream end of the project site and to the outlet to the Limfjord, it was found to be 0.3‰, meaning that the slope is very gentle [Madsen, 2021a]. This is supported by the fact that the surrounding area is relatively flat, as shown in Figure 4.3, and is mostly covered by protected wetland habitats that are characterized by slow-moving water and low-lying vegetation [U.S. EPA]. These environments do not provide the conditions necessary for a stronger flow in the stream.

In a follow-up report, Madsen [2021b] found that the flow capacity of the stream had improved since 1987. This was determined by observing a reduced water surface elevation of 10 cm in the lower section and 15-20 cm in the upper section of the stream. The stream had become slightly narrower and deeper, which had led to an improved flow capacity. Additionally, the creation of two oxbow lakes in the period between 1995 and 2016 resulted in a reduction of the stream length by approximately 300 meters, causing an increase in the slope over this section, leading to higher velocities and a lower water level.

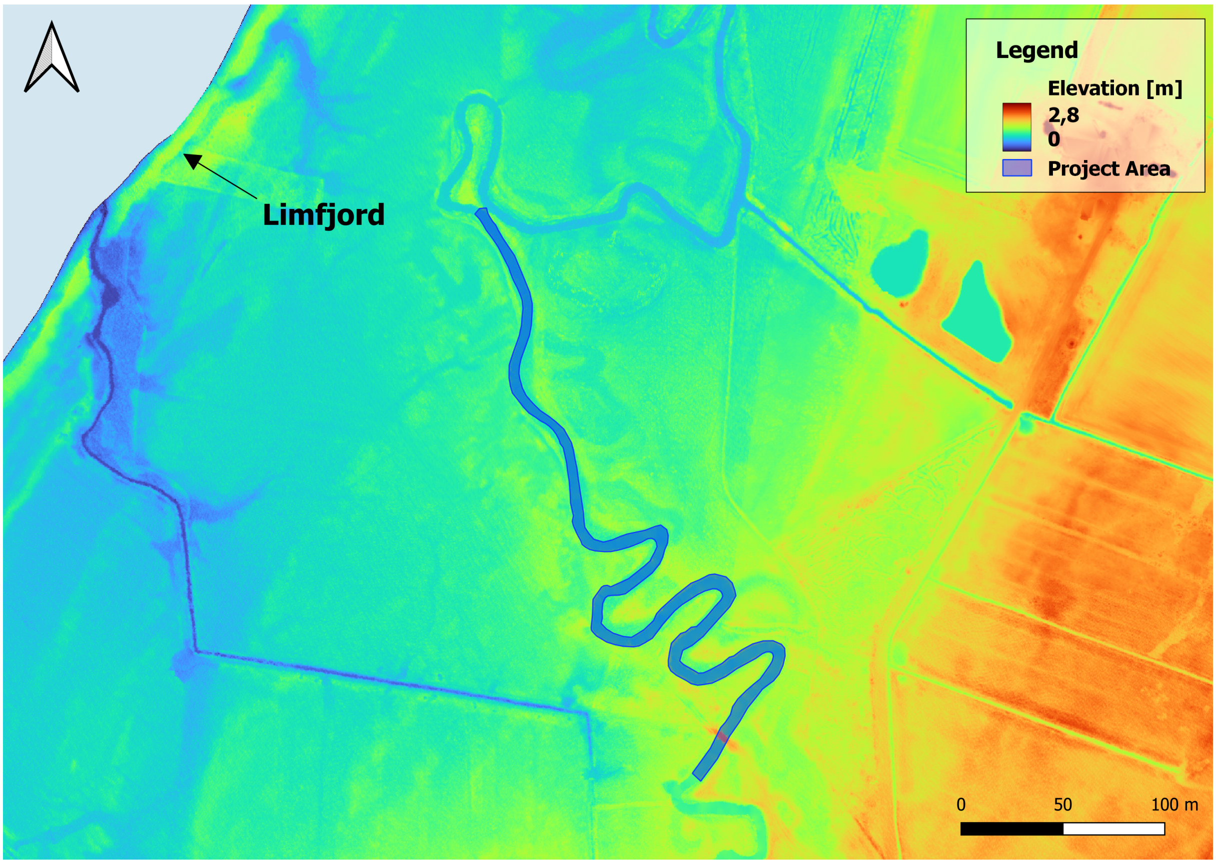

Figure 4.3. Elevation map of the project site.

4.2 Hydrological properties of Binderup Å

Data from 'Station 10.17' [WSP and Miljøstyrelsen] shows that major seasonal differences in water level discharge are present in Binderup Å. A larger minimum and maximum flow are present during winter compared to summer, being up to 100% higher in the case of maximum discharge, as shown in Figure 4.4. However, despite these seasonal differences in discharge, the range of water levels is quite similar for both periods. During both winter and summer, an increase in flow and a corresponding rise in water level is observed, however the increase in water level for the same increase in flow is more significant in summer. This could be related to periods of low maintenance of the stream, where the higher presence of vegetation and sediments could have reduced the available flow area, resulting in an increase in water level. For the majority of the time, the stream has a water level between 1.75-2.25 m with a discharge of 0.5-1.5 m^3/s. Used flow and water level time series can be found in Appendix A.

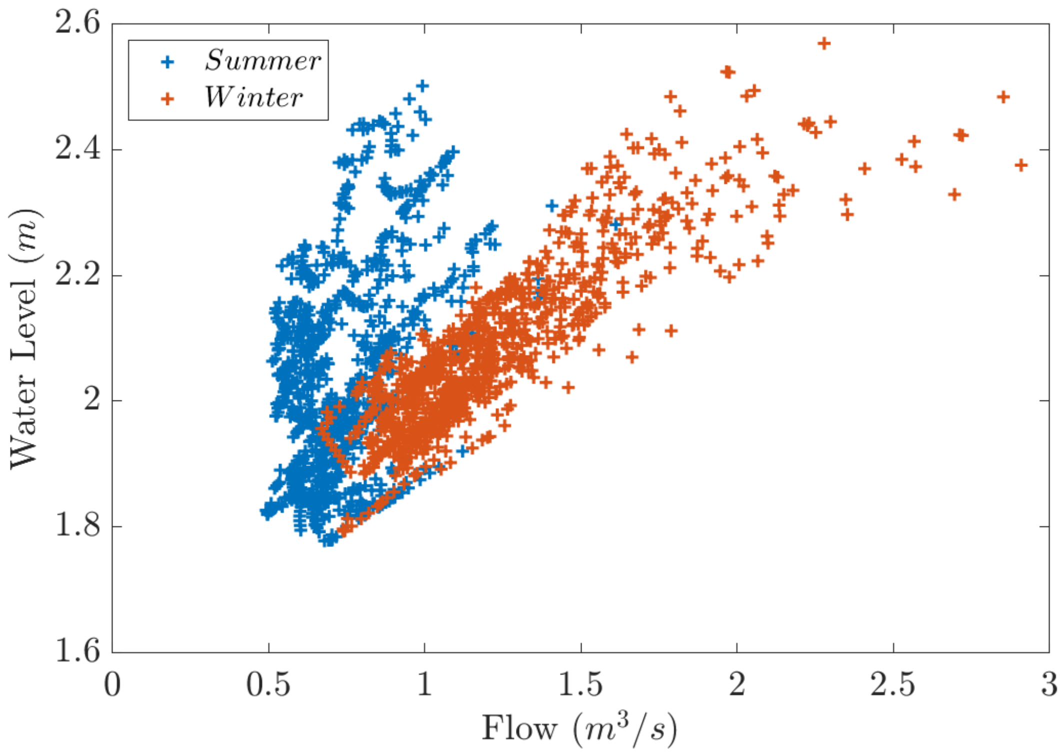

Figure 4.4. Summer and Winter rating curve for Binderup Å made with 2012-2021 data from "Station 10.17 Binderup Å, Ns Binderup Mølle" measuring station. Made with data from WSP and Miljøstyrelsen.

Seasonal variations of daily average discharge at Binderup Å for the 2012-2021 period are displayed in Figure 4.5a. Throughout the period, a clear pattern of fluctuations in water flow can be observed as the data suggests that during summer the flow falls to minimum values. Following this, it continuously increases until the maximum during December and January when it starts to drop once again. During lower flow months, the observed variability in flow is smaller than in higher discharge seasons.

Figure 4.5b indicates that the highest water levels occur in August and last over the winter, while the lowest water levels are measured in April and May. These findings are consistent with the typical seasonal fluctuations in water levels that are observed in many regions, which are often influenced by factors such as precipitation, evaporation, and temperature [Sand-Jensen and Lindegaard-Petersen, 2004]. Moreover, backwater effects from the Limfjord may be present during certain periods of the year. This could be relevant during summer and be another reason for the observed high water level with low-flow conditions.

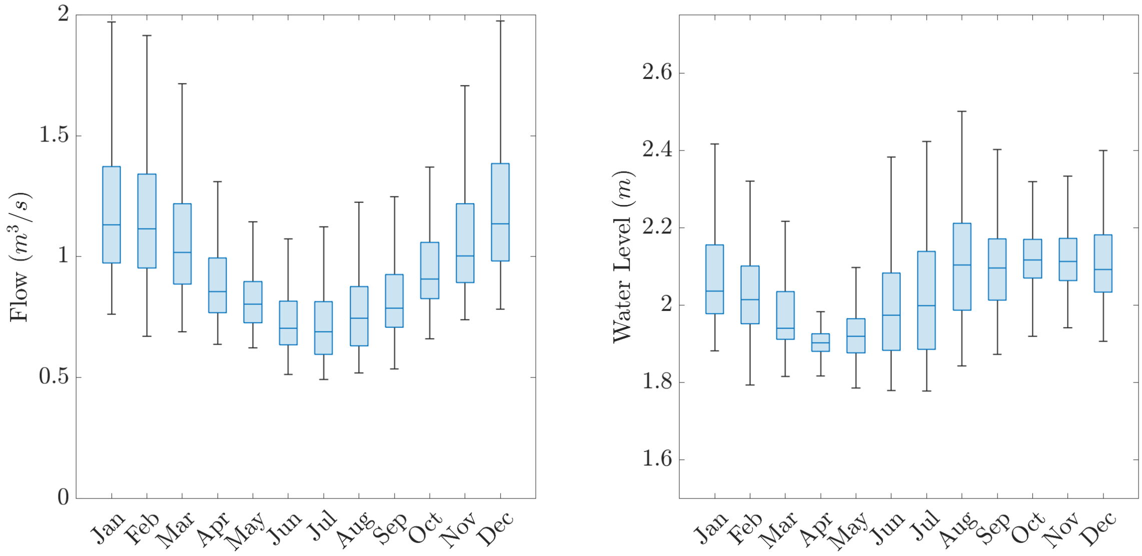

(a) Discharge ***(b)*** Water Level

Figure 4.5. Seasonal variation in (a) average daily discharge; and (b) average daily water lever, with median values, 25th and 75th percentiles, and the minimum and maximum values for each month, during 2012-2021. Data from WSP and Miljøstyrelsen at "Station 10.17 Binderup Å, Ns Binderup Mølle".

The stream was split up into two sections; the meandering upstream section and the straighter downstream section, as illustrated in Figure 4.6. This provided two distinct cases from which the effect of meanders on resistance to flow could be assessed.

A meandering channel can be defined by as a stream with a sinuosity larger than 1.5 [Wilzbach and Cummin, 2019]. The sinuosity of a stream is defined as the ratio between the channel length and its valley length, i.e. the stream-wise length from point A to point B, and the straight-line distance between points A and B, as given by equation 4.1.

$$Sinuosity = \frac{StreamwiseLength}{StraightLineLength} \tag{4.1}$$

The sinuosity of the full length of the project site was 1.82, while for the meandering and straight sections it was 2.74 and 1.06 respectively. This confirms that the 'meandering' section can be regarded as highly sinuous, and the 'straight' section as straight.

The degree of curvature of individual bends is defined as the ratio between the channel width, B, to the centerline radius of channel curvature, r_c, as given by Equation 4.2. The value of C for a straight channel will thereby be approaching 0, with highly meandering bends approaching 1 [Zhou and Endreny, 2020].

$$C = \frac{B}{r_c} \tag{4.2}$$

Two meanders in stream were selected for analysis, as displayed in Figure 4.6; Meander 1, with a mean width of 5.24 and a radius of 7.00 meters, returning a curvature of 0.75, and Meander 2 with a width of 5.02 meters and a radius of 8.03 meters, resulting in a curvature of 0.625.

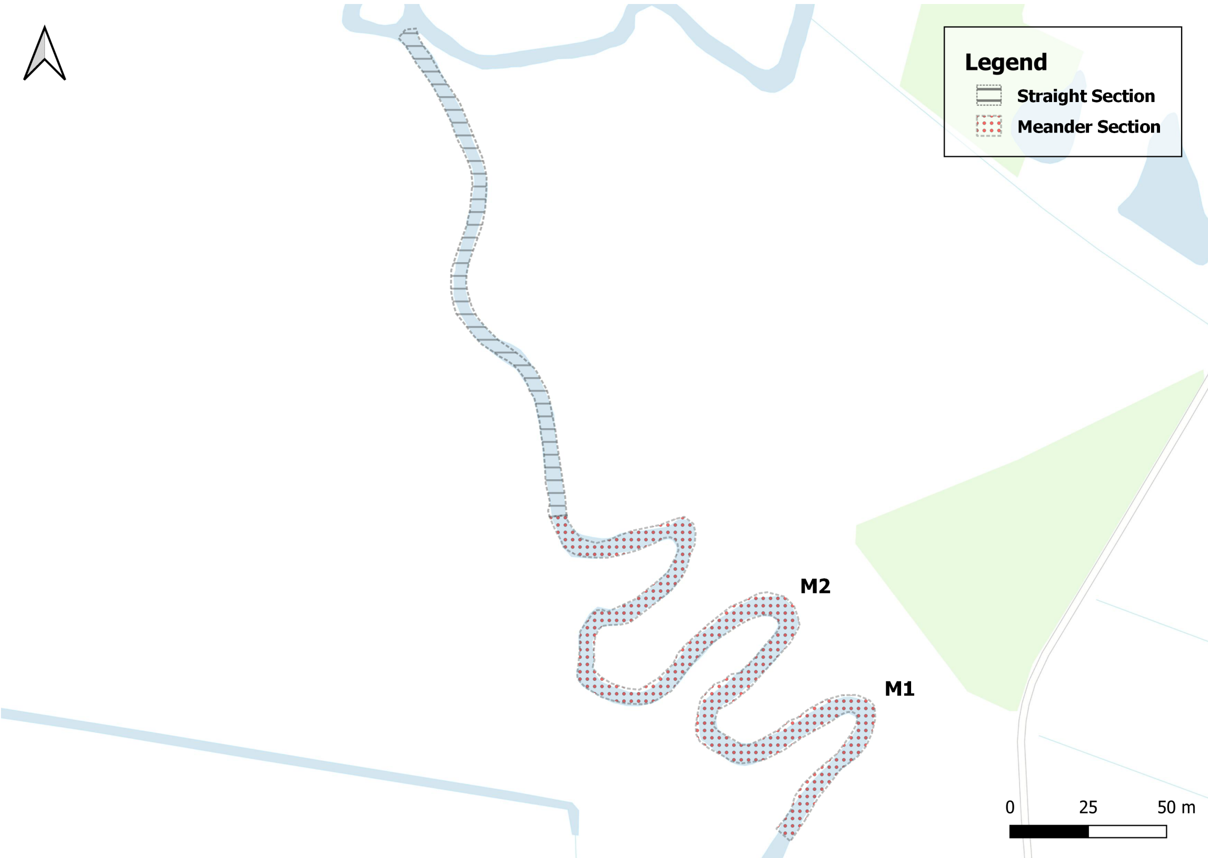

Figure 4.6. Division of area between meandered and straight sections.

The water surface elevation and slope throughout the project site were measured during two distinct periods that were classified as high and low flow conditions, respectively. The low-flow measurements were taken between the 15th and 18th of December, 2022, while the high-flow measurements were taken on the 9th and 10th of January, 2023. Figure 4.7 shows a comparison of the conditions between these days.

During the low-flow conditions, the water level was below the bank limits of the Binderup Å. As is observed in Figure 4.7a, a thin layer of ice was present at the surface close to the banks. Moreover, a larger presence of vegetation was observed at the left bank of the stream. During high-flow conditions, the water level was above the bank limits in some areas, as seen in Figure 4.7b, reaching the flood plain. For that reason, the vegetation at the banks was partially covered by the water.

(a) Low-Flow Condition

(b) High-Flow Condition

Figure 4.7. Pictures of Binderup Å taken during field days at (a) low-flow conditions; and (b) high-flow conditions.

As seen in Figure 4.8, under high flow conditions, the meandering section had an energy gradient of 0.56‰, compared to the straight sections 0.48‰. Under low flow conditions, the gradient was 0.58‰ in the meandering and 0.4‰ in the straight. In both cases, the meandering section showed a higher energy gradient than the straight, confirming that the energy losses in this meandering portion of Binderup Å were higher than in the straight portion. The average energy gradient of the water surface across the entire project site was measured to be slightly lower under high-flow conditions at 0.50‰, compared to 0.53‰ under low-flow conditions. Meanwhile, it was higher than that measured by WSP, although this could be explained by the significantly longer reach including the upstream weir which was not included in this project area.

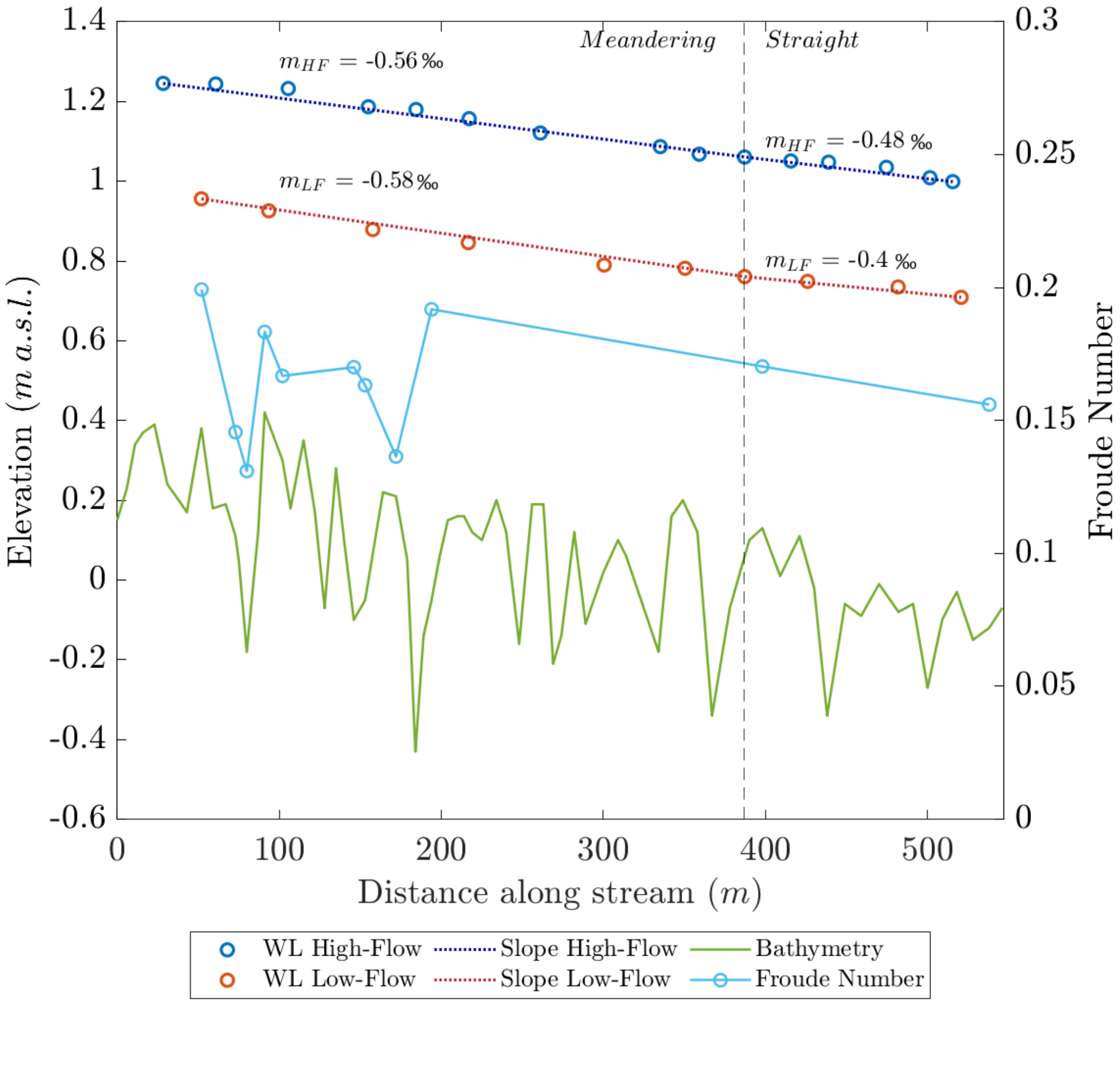

Figure 4.8. Surface slope under high (m_{HF}) and low (m_{LF}) flow conditions, as well as measured water level (WL) and bathymetry throughout meandering and straight sections. Calculated Froude Number from measurements is also displayed. The dashed black vertical line defines the division between meandering and straight portions of the study area in Binderup Å.

Using water level and slope measurements taken at the project site along with water level stations in nearby areas of the Limfjord allowed an evaluation of whether the Limfjord had an impact on the hydraulic conditions in the selected section of the stream during the project period.

Using the average slope for each period and the water measurements taken from the 'Cabin St.' measurement station, the lowest surface elevation at the downstream end of the project site on any of the field days could be predicted. The lowest water levels measured at 'Cabin St.' were 0.87 meters a.s.l. for low-flow conditions (days between the 15th and 18th of December), and 1.20 meters a.s.l. under high-flow (days between the 9th and 10th and January). Given the calculated slope and a stream-wise distance of 520 meters, this would equate to a minimum water level of 0.61 meters and 0.94 meters at the end of the project site each day.

The water level in the Limfjord near the outlet of the stream was estimated by interpolating data from water measuring stations at Aalborg Øst Harbour and Løgstør Harbour, available from DMI [Danish Meteorological Institute].

During the 'low-flow' fieldwork period, the highest water level at the outlet of Binderup Å to Limfjorden was estimated to be a maximum of 0.26 meters with a minimum of -0.09 meters, while during the 'high-flow' period, it was found to be 0.59 meters with a minimum of 0.30 meters.

Table 4.1. Summary of data used for interpolating water elevation at the mouth of Binderup Å, and determining the risk of backwater from the Limfjord. WL = water level.

Condition	**Slope** [‰]	**Elevation at Cabin St.** [$m a.s.l.$]	**WL at downstream end of project site** [$m a.s.l.$]	**WL range at mouth of Binderup Å** [$m a.s.l.$]
Low Flow	0.53	0.87	0.61	-0.09 - 0.26
High Flow	0.50	1.20	0.94	0.30 - 0.59

As the water level calculated at the outlet to the Limfjord was below that of the project site, it was assumed that the Limfjord did not have any influence on the hydraulic conditions in the selected section of the stream, at least during the time when measurements were taken.

Finally, to know the nature of the flow present at Binderup Å, the Froude Number (F_r) was calculated for each condition using measured data, as illustrated in Figure 4.8. This number is defined as the ratio between inertial and gravitational forces [Brorsen and Larsen, 2009]. Expressed by the average velocity (v), hydraulic mean depth (h_m, ratio between area and width) and gravitational acceleration (g), as described in Equation 4.3. As at every section of the stream, the calculated Froude number was lower than 1, then the flow could be defined as sub-critical flow. This type of flow is dominated by gravitational and frictional forces and behaves in a stable way.

$$F_r = \frac{v}{\sqrt{g h_m}} \tag{4.3}$$

In summary, the project site at Binderup Å was deemed appropriate to evaluate the effects of meanders on resistance to flow for several reasons. First of all, it had two adjacent sections that could be distinctly defined as either meandering or straight, each of which demonstrated varying energy gradients, the higher of which was found in the meandering section as would be expected. Additionally, the site was assumed to not be affected by any backwater effects from the Limfjord, at least not in the period during which measurements were taken.

5 Validation of ADCP Flow Measurements

An essential parameter for managing and monitoring a stream is the water flow, quantified in terms of both volume and velocity. Several measurement methods exist, although modern technologies present more efficient and less intrusive ways to achieve the same and often more detailed results. One of these modern technologies is the Acoustic Doppler Current Profiler (ADCP) which is a device that uses acoustic pulses to measure flow velocities and bathymetry in bodies of water. In this case, it was used to gather data on water flow, 3-D velocity profiles and bathymetry data from Binderup Å. Three separate programs, WinRiver II, QRev and Velocity Mapping Toolbox (VMT) were used in data acquisition, quality control and data processing. The process of using WinRiver II and QRev is described in Appendix B, while VMT is described in more detail in Appendix C. Walkthrough videos for each can be found at WinRiver II & QRev Walkthrough[1] and VMT Walkthrough[2].

The reliability of the ADCP measurements was verified against a previously verified method, namely a propeller current meter. Therefore, water velocity measurements were performed simultaneously with the ADCP and propeller current meter methods at twelve cross-sections, as illustrated in Figure 5.1, the coordinates of which can be found in Table B.2 of the Appendix B. The comparison between the two methods was based on volumetric flow, the velocity profile through the cross-section, and the bathymetry identified by each method.

Measurements were taken between the 15-18th of December of 2022. To ensure that the hydraulic conditions were as similar as possible between measurements in any one cross-section location, it was essential to conduct current meter and ADCP measurements in close temporal proximity. Additionally, water level measurements were carried out to control for variations in flow due to upstream conditions and meteorological factors. Water level fluctuations were recorded during the fieldwork, with a range of +/- 2.5 centimetres.

[1]https://urbanwater.aau.dk/ADCP/WinRiver$_Q Rev_T utorial.mp4$
[2]https://urbanwater.aau.dk/ADCP/VMT$_T utorial.mp4$

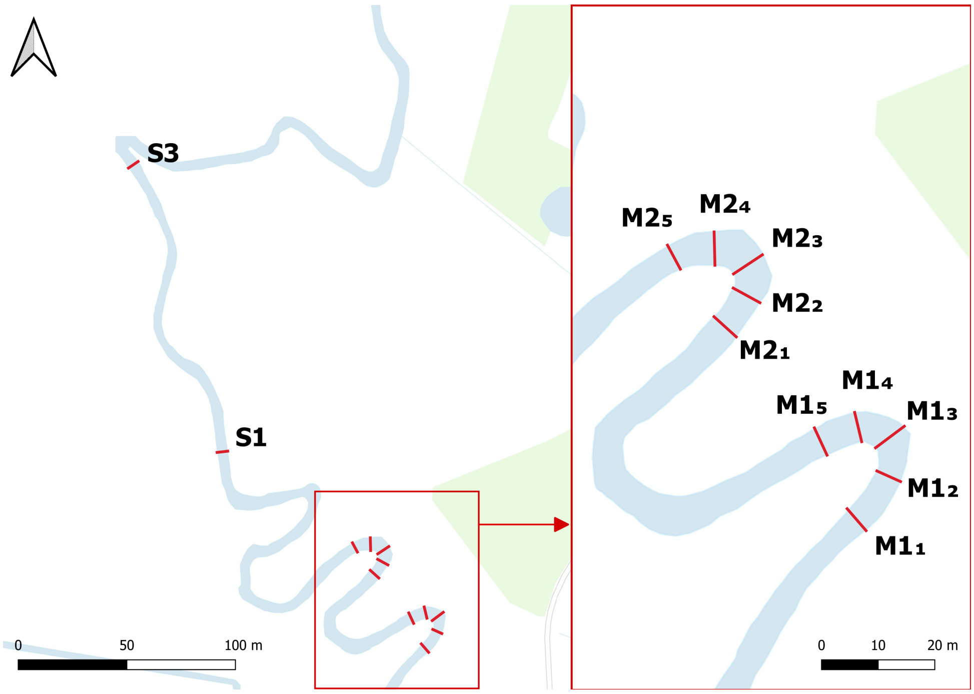

Figure 5.1. Overview of the twelve cross-sections taken at Binderup Å, where $M1/2_{1-5}$ are cross-sections in the respective meanders, and S1/3 are in the straight section.

5.1 Discharge measurement using current meter

The propeller current meter method involves a propeller being submerged into the water at regular spatial intervals along the cross-section being studied, as demonstrated in Figure 5.2. The device consists of a propeller connected to a computer counting its RPM, which in turn is converted to a velocity.

The cross-section where the flow is measured must to be divided into a number of equally spaced vertical intervals from which velocity is measured at regularly spaced depths [Chauhan et al., 2014]. According to international standards such as DS/EN ISO 748, the selected number of verticals is established as a function of the stream's width. While for the measuring points in each vertical, there must be at least three points in each. The distribution of points needs to be sufficient to represent the flow structure of the stream. An insufficient number of verticals and points mean that the velocity distribution is not determined adequately, and the result becomes uncertain [Chauhan et al., 2014].

The trapezoid integration method is used to calculate the flow through each vertical in the stream. The water velocity at the stream bed is assumed to be zero, and the water table velocity is equal to the top measurement. Thereafter, the calculated flows are integrated into the horizontal direction, assuming that the flow is zero at the river banks.

This method is valued because it requires little equipment and is easily repeatable. On the other hand, physically standing in and traversing the stream's width can be time-consuming and invasive to the ecosystem. Furthermore, it is essential to maintain a consistent flow direction, regular velocity distribution across the section, and a perpendicular orientation to the measuring cross-sectional profile while avoiding spots with eddies and counter-currents to reduce uncertainty in the results. Therefore, it is recommended to follow the guidelines provided by [Andersen, 1989] to minimize the environmental impact and obtain accurate results.

Figure 5.2. Measurements being taken for the discharge calculation using propeller method at Binderup Å.

5.2 Acoustic Doppler Current Profiler method

The Acoustic Doppler Current Profiler (ADCP) is a more modern approach to flow measurement, requiring far less time and being far less intrusive on the environment. It involves an acoustic sensor mounted on a small floating boat that is sent back and forth across the width of the stream. For this project, a cableway was used to ensure the same path was followed for each transect, but it can also be remotely controlled or led behind a manned boat. It can, in principle, be carried out by a single operator, although it does require some knowledge and experience with ADCP-specific software. In this case, WinRiver II was used for data acquisition and QRev for quality control, a full explanation for both of which can be found in Appendix B. It also requires a laptop to carry out the measurements, so sufficient battery capacity or power supply for the duration of the measurement period is required. The required set-up is displayed in Figure 5.4. The measurement of water velocity by an ADCP is made by propagating a fixed-frequency sound wave through the water column and computing the change in frequency on echoes from suspended particles and bubbles [Shields and Rigby, 2005]. It is assumed that these particles are moving at the same speed as the water.

The water column under the transducer is divided into bins of equal depths. Water depth, 3-D velocity, temperature, boat displacement, and several other parameters are collected at one-second intervals for each bin [Gordon, 1996].

ADCP offers the advantage of rapid data collection. However, the technology has limitations, which impact its ability to accurately measure water flow in certain conditions. For example, the transducer used in ADCP must be fully submerged, meaning that the top 0.1 meters of the water column cannot be measured. Additionally, reflections from the bottom of the water column can interfere with water echoes in the bottom 6%, resulting in inaccurate measurements. Finally, near-shore areas are also problematic, as the presence of shallow water can prevent accurate measurements [TeledyneMarine, 2022]. Therefore, water flow needs to be estimated in all these four areas, as seen in Figure 5.3.

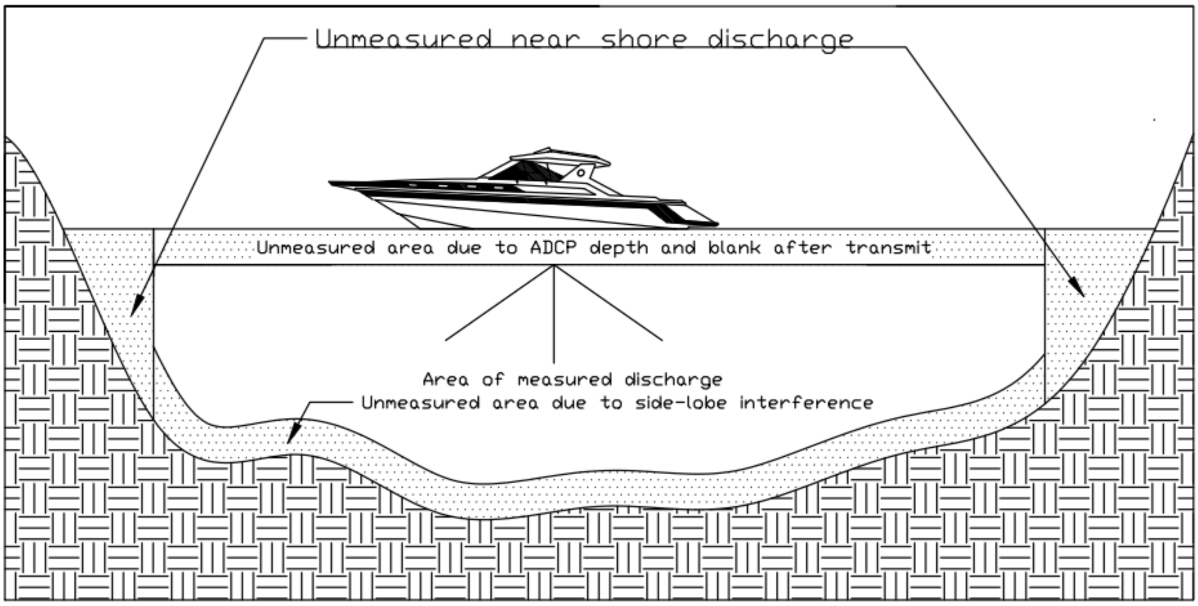

Figure 5.3. Area of measured and unmeasured discharge by ADCP.

The total discharge is calculated as the sum discharge for each ADCP ensemble based on the velocity of the vessel relative to the bottom and depth to the bottom for each beam. A constant or power extrapolation method can be selected based on the flow conditions to estimate the flow at the unmeasured top and bottom parts. Finally, the near-shore discharge is estimated using a ratio-extrapolation method for calculating the velocity in the unmeasured area by using the measured velocity in the adjacent cell. A detailed description of these extrapolation methods with the ones used in this project can be found in Appendix B. At every location, at least four high-quality transects are recommended, with a single dataset calculated as an average of these [TeledyneMarine, 2022].

Chauhan et al. [2014] shown that ADCP results are similar to the current meter with an average difference of 1.68 %. The difference can range from 1.04 % to 9.8 % with two outliers at 24.5% and 25.3 %.

Figure 5.4. Flow measurement being taken by the ADCP method at Binderup Å.

5.3 Water flow comparison

Simultaneous measurements taken with a propeller current meter and ADCP in Binderup Å have allowed comparisons of the discharge measurement by the two methods over 12 cross-sections. The average discharge calculated with the propeller method was 0.68 m^3/sec with a standard deviation of 0.055 m^3/sec. While for the ADCP method, the mean obtained value was 0.74 m^3/sec with a standard deviation of 0.047 m^3/sec, as seen in Figure 5.5. The propeller method showed more variability of results, especially in the meandered area. This deviation may have resulted from measurements taken in an area with high sinuosity where eddies and counter-current flows occur, resulting in irregular velocity profiles that are hard to sample with a propeller, compared with a straight section. On the other hand, ADCP results showed less variability between each other, being less spread around the mean value. In this case, it may be a result of the ADCP's ability to obtain velocity data at a high resolution, capturing the change of velocity in the three directions. Used discharge data can be found in Table D.1, in Appendix D.

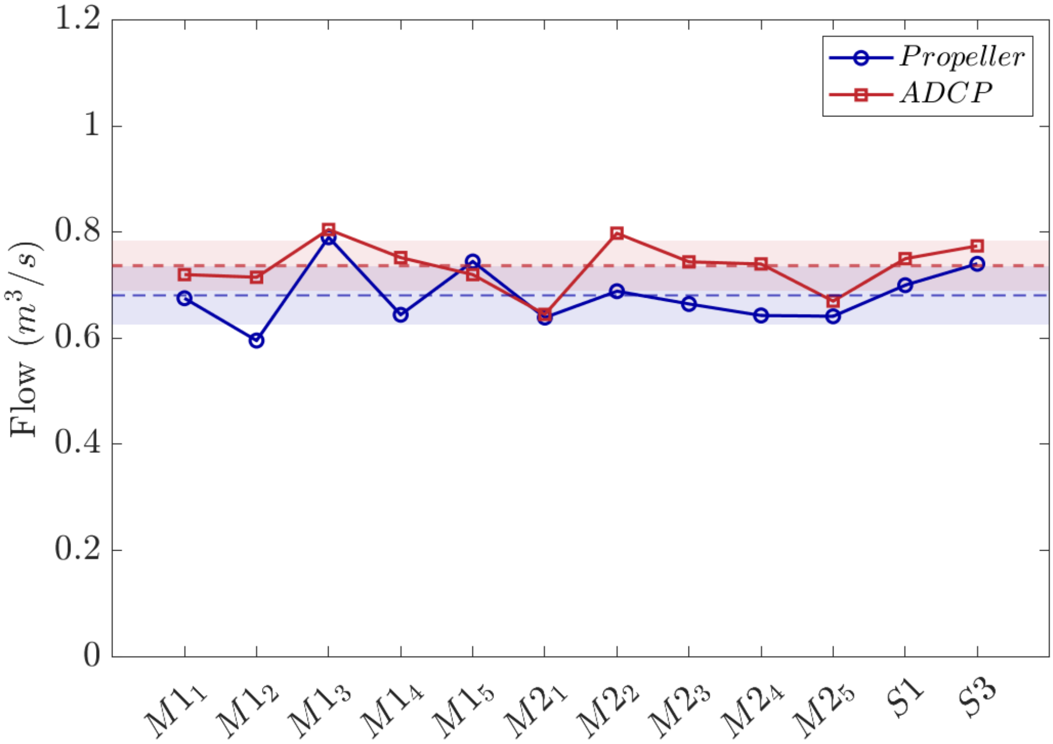

Figure 5.5. Measured water flow at each cross-section with both propeller and ADCP methods. Dashed lines show the mean flow value while the shaded area represents one standard deviation from the mean.

The percentage difference of the propeller results with respect to the ADCP results was calculated for each cross-section as shown in Figure 5.6. The discharge computed by the ADCP was, on average, 7.45% higher than the discharge established by the propeller method. In general, the difference in flow between methods was in the range of 0 - 16%, with the ADCP measurement being higher in all cases except $M1_5$. Here, the flow measured by the propeller current meter was 3.4% higher than the ADCP.

Measurements taken at the start and end of each meander that is adjacent to short straight sections, as well as from the straight reach ($M1_1$, $M1_5$, $M2_1$, $M2_5$, $S1$ and $S3$) displayed lower percentage differences with a mean difference of 4.30%. In the meandering areas, the mean percentage difference is 11.72%.

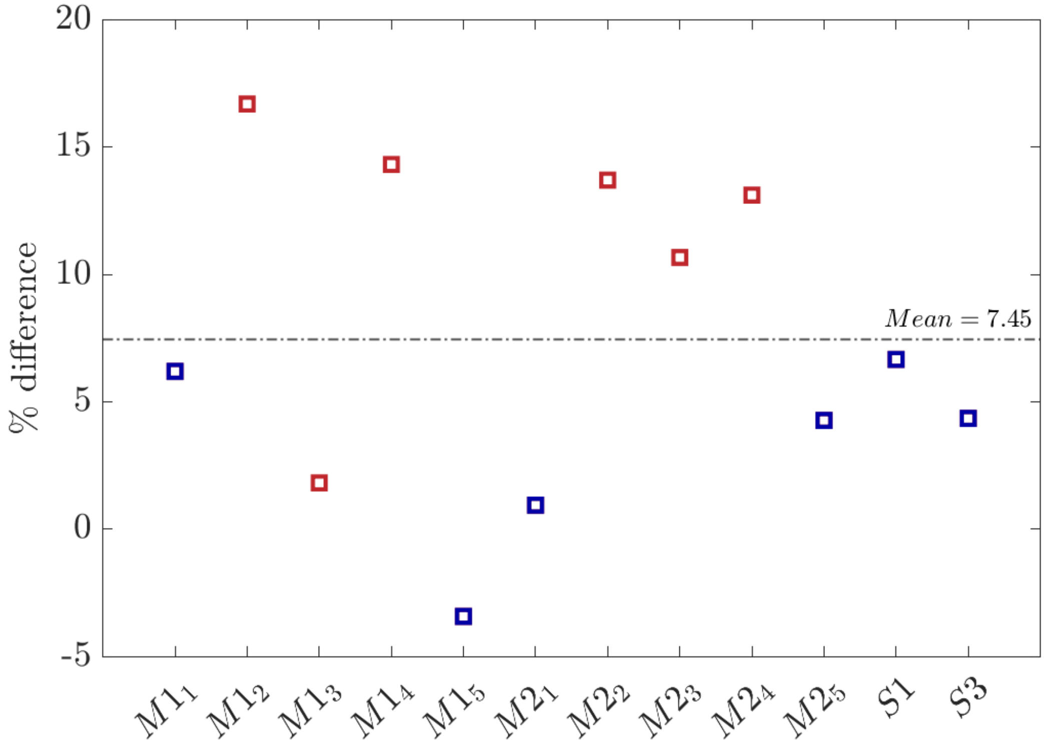

Figure 5.6. Percentage difference from the ADCP measured flow at each cross-section, with planes in or adjacent to straight sections highlighted in blue.

Furthermore, the results from the propeller current meter and the ADCP exhibit a difference in flow measurement visualized in a scatter plot in Figure 5.7. Most of the measurements are displaced upwards of the line of perfect agreement. This suggests that the ADCP measurements tend to be higher than the propeller meter measurements, although there is still a linear correlation between the two methods. Once again, it was highlighted that flows taken in or adjacent to a straight section were, in general, closer to the line of perfect agreement than the ones taken at the meander.

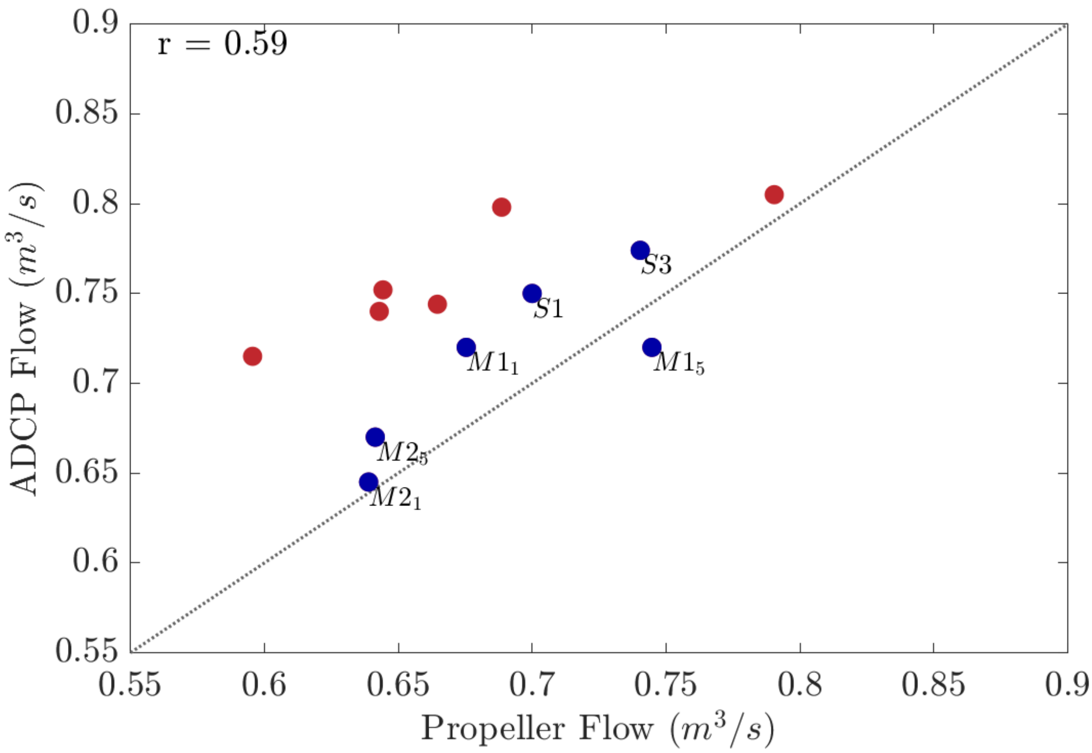

Figure 5.7. Scatter plot of the water flow measured with propeller and ADCP, with the line of perfect agreement. Planes in or adjacent to straight sections are highlighted in blue. The correlation coefficient (r) is also displayed.

5.4 Bathymetry comparison

The bathymetry of the different locations was obtained both manually utilizing a ruled stick as part of the propeller current meter method and with the ADCP referencing each measuring point with the help of a differential GPS attached to the system. The geo-referenced ADCP data was then processed utilizing Velocity Mapping Toolbox (VMT) to obtain the average bathymetry between the transects of each location. VMT is a Matlab-based software developed by the U.S. Geological Survey (USGS) to simplify the processing of the transect data of each cross-section. The method for using VMT to process the data is described in Appendix C.

As a result of differences in width between the two methods, the length where both data sets contain common depth information was used. In Figure 5.8, the obtained bathymetry by both methods is displayed for locations $M1_2$ and $S3$. The collection of all obtained bathymetries, can be found in Appendix C.

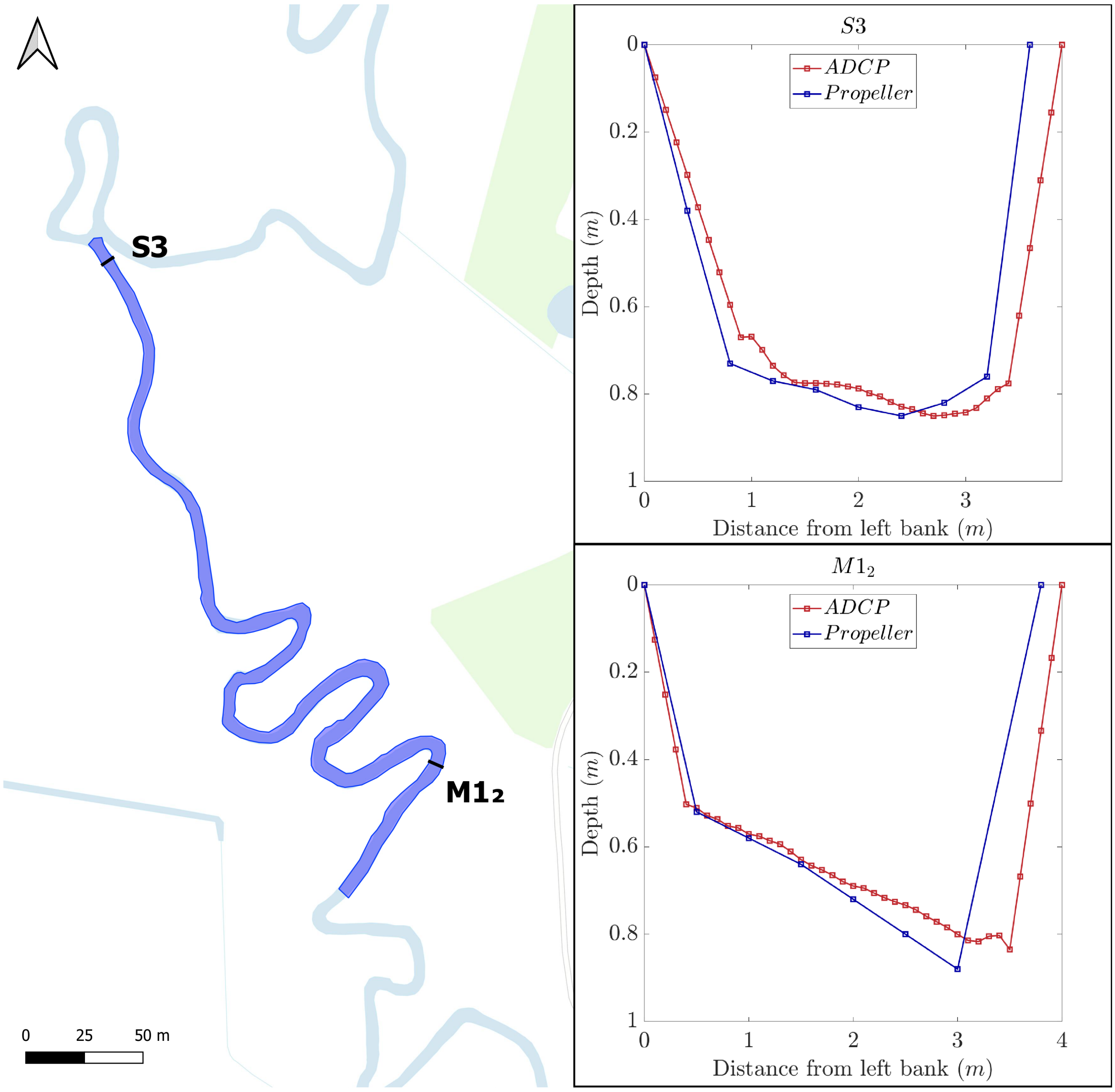

Figure 5.8. Location and comparison of bathymetries measured at $S3$ and $M1_2$.

In general, small differences were observed in the riverbed elevation between methods, Figure 5.9. The obtained median when all locations were considered together was around 5% lower for the ADCP, while half of the data had a difference between -10 and 1% represented by the interquartile range. This means that in general, the depths taken via propeller returned higher depth values. The larger differences observed in some locations like $S1$ may indicate that the ADCP was able to capture a more detailed representation of the terrain or even the presence of some interference overlooked by the less comprehensive propeller method.

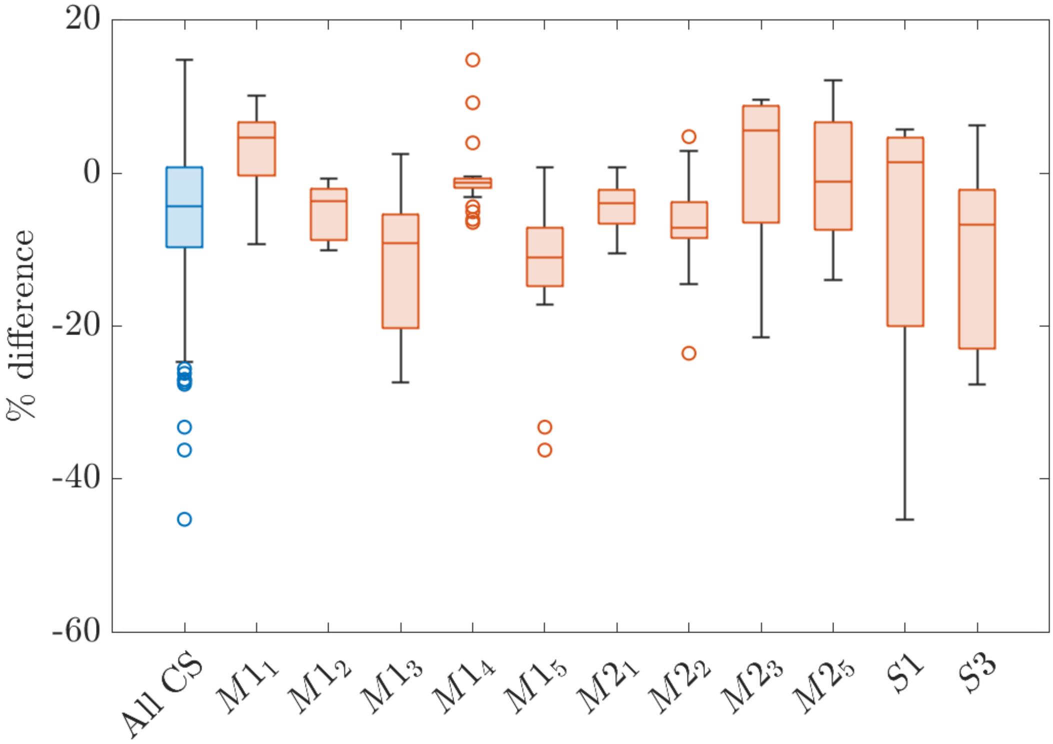

Figure 5.9. Box plot of the percentage difference between measured depths by ADCP and propeller for all locations and grouped by cross-sections. Location $S1$ has 5 outlier points up to -312 % difference that are not shown in the graph. Line inside the box shows the median; box limits display 25 and 75 quartiles, dotes are values outside 1.5 times the range interquartile, and whiskers limits represent maximum and minimum values. CS = Cross-sections.

Furthermore, to overcome the problem of differences in width between cross-sections, the cross-sectional area, wetted perimeter and hydraulic radius for each method were calculated and compared, as seen in Figure 5.10. In general, both methods showed similar results for the analysed parameters. Values of cross-sectional area and wetted perimeter were closer to the line of perfect agreement, as seen in Figures 5.10a and 5.10b. In the case of the area, the propeller method had a moderate tendency to give higher values than the ADCP. On the other hand, for the wetted perimeter, the opposite effect was observed. Moreover, it is observed that those cross-sections close to the apex of the stream ($M1_3$ and $M2_3$) displayed the highest values of the area and wetted perimeter, indicating an increase in these zones of the stream.

When the ratio of flow area and wetted perimeter, called hydraulic radius is considered, as is displayed in Figure 6.7c, the ADCP tends to provide higher results than the propeller method. However, the agreement between methods is also considerably high. In general, cross-sections in meanders had larger values of the three analysed parameters than those at straight sections of the stream. The used values of the parameters used for this comparison are displayed in Table D.2, in Appendix D.

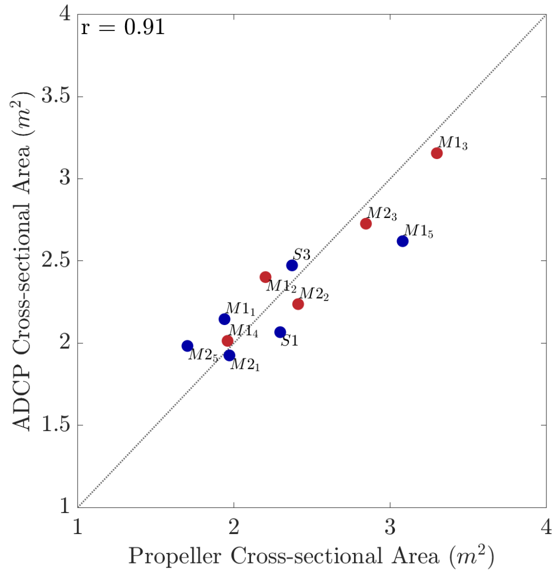

(a) Cross-sectional area

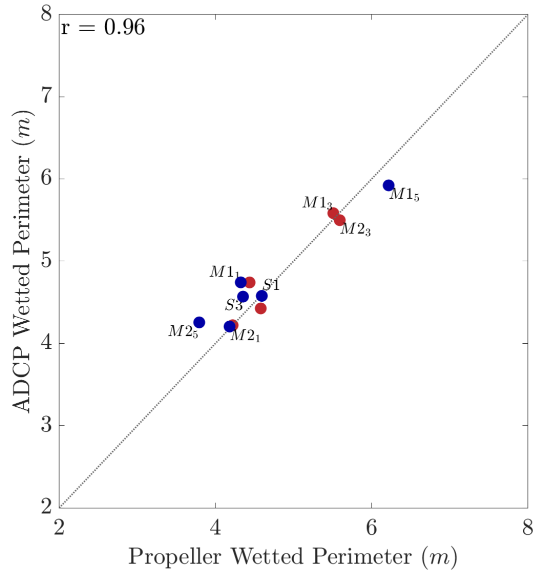

(b) Wetted Perimeter

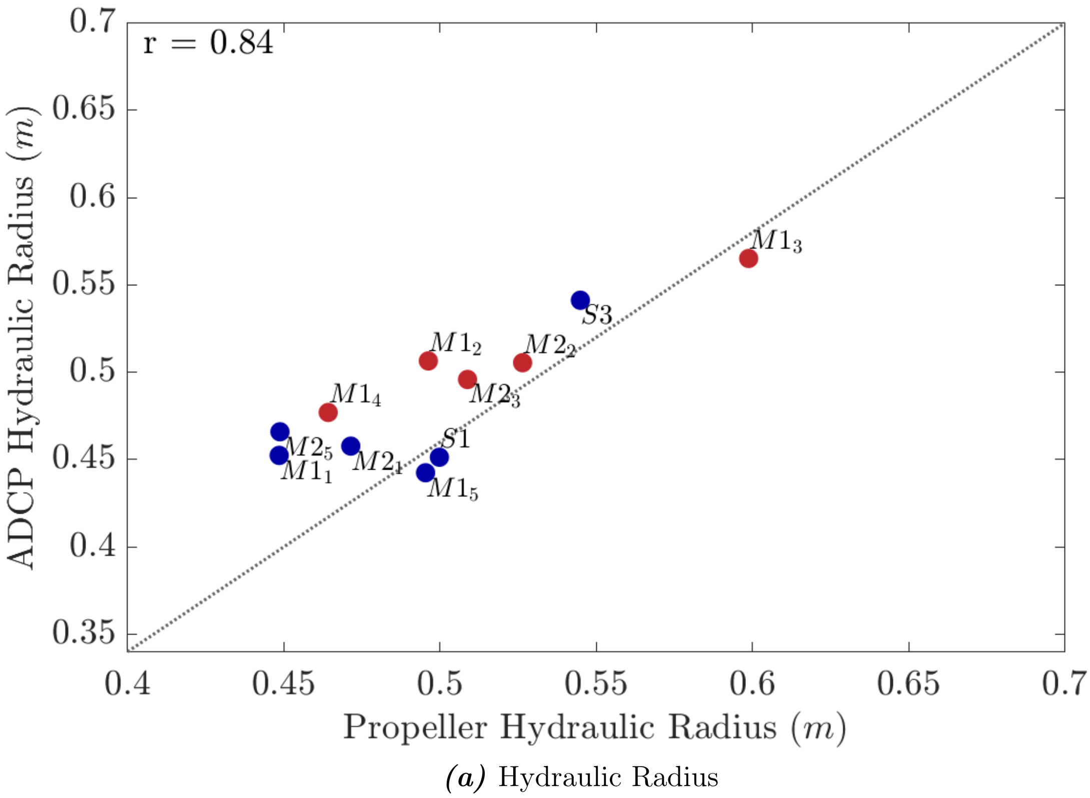

(a) Hydraulic Radius

Figure 5.10. Scatter plot of the (a)cross-sectional area; (b) wetted perimeter; and (c) hydraulic radius, measured with propeller and ADCP, with the line of perfect agreement. Planes in or adjacent to straight sections are highlighted in blue. The correlation coefficient (r) is also displayed.

5.5 Water velocity comparison

Water velocity measurements were obtained using a propeller current meter and ADCP, with subsequent comparison of the two methods. The processed ADCP velocities were derived by processing the transects of each location utilizing a least squares fit of the data cloud to determine the mean cross-section orientation. Data from each transect was then projected onto a new plane using an orthogonal translation and interpolated into a user-defined grid. The arithmetic average of velocities was ultimately computed between all transects. A more detailed description of the velocity data processing with VMT is displayed in Appendix C.

In Figure 5.11a, velocity points measured by the two methods are displayed as a function of distance from the left bank. Both methods had the same velocity profile, with larger velocities at the central part of the stream and lower ones at the edges. As expected, ADCP provided more detailed water velocity measurements, with more data points and variability in velocity readings, especially getting higher velocities in certain areas.

However, the propeller method proved to be able to measure closest to the banks, capturing the characteristics of the velocity profile at the surroundings of these areas with higher friction and tendency of formation of eddies and counter-current circulation. It was also able to capture velocity data closer to the bottom and surface, due to the possibility of setting the desired measuring height with this method. While, as explained in section 5.2, the ADCP has limitations in acquiring values from the top surface, close to the bottom and next to both banks. In these areas, there are neither measurements nor estimations of water velocities by the system.

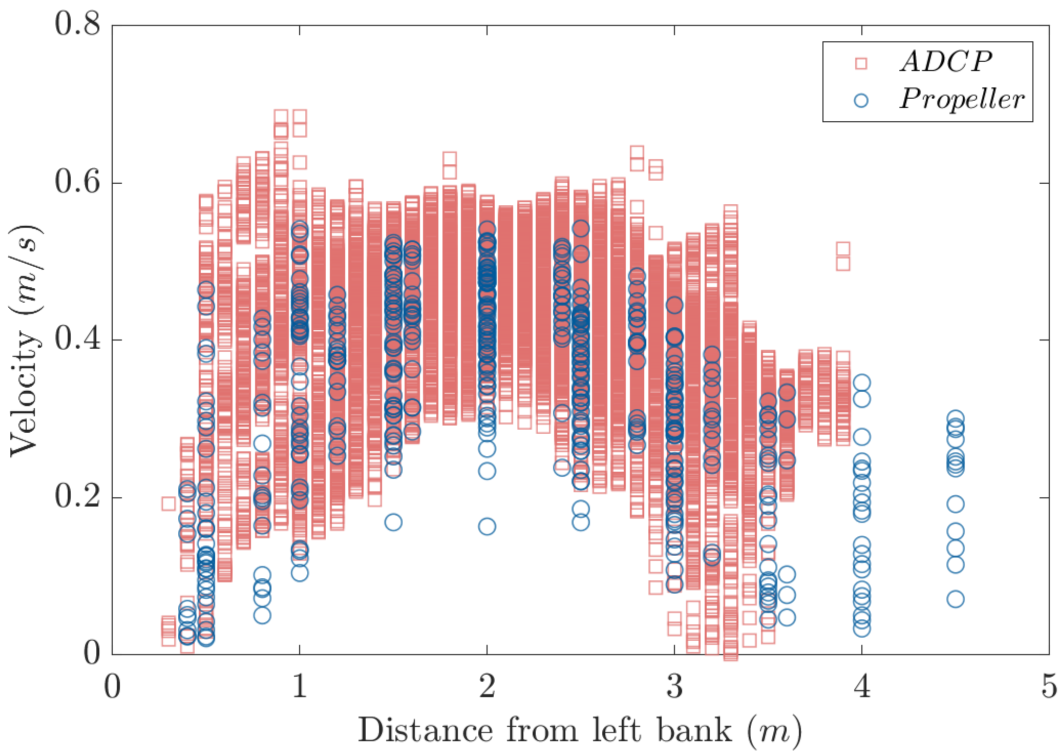

(a) All measured velocity points

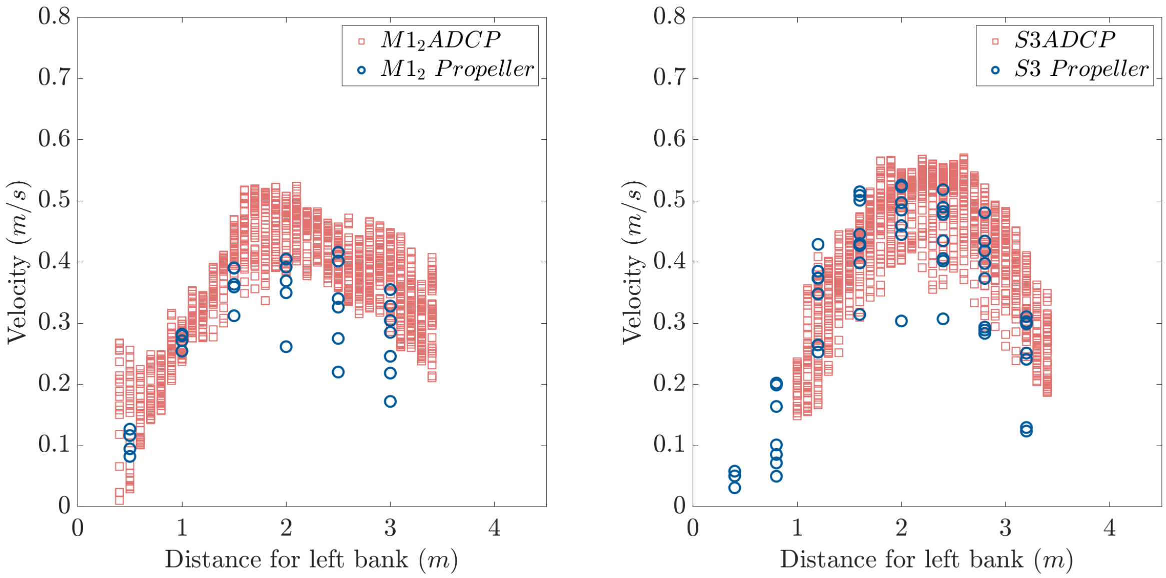

(a) $M1_2$ velocity points ***(b)*** $S3$ velocity points

Figure 5.11. Measured velocity points with ADCP and Propeller respect to the left bank for (a) all the cross-sections; (b) $M1_2$; and (c) $S3$.

When cross-sections of a bend ($M1_2$) and straight ($S3$) areas were analysed separately, as displayed in Figures 5.11a and 5.11b, certain particularities of the velocity profiles were observed. Firstly, for both types of cross-sections, the two methods described the expected general tendency of velocity along the stream. In $M1_2$ lower values were obtained in the inner bank and increased toward the outer one. This describes a typical profile for a meandering section, where the shoaling effects at the inner part direct the flow towards the channel centre [Bisht, 2020]. In $S3$ similar velocity values were obtained at both sides of the stream with the highest values at the centre. Showing that in a straight section, the velocity is uniformly distributed and the friction at both sides was holding back the flow.

However, even though both methods describe the general tendency of the profile, in the meander section the propeller current meter generally measured lower velocities at the same distance from the left bank compared to the ADCP. On the other hand, in the straight cross-section, the same range of velocity magnitude was obtained both with the propeller and ADCP.

Cross-sectional velocity profiles also display interesting insights as shown in Figure 5.12. For both the meander and straight sections, the vertical velocity profiles display lower values at the bottom and higher closest to the surface for the measurements taken at the central part of the stream, representing the higher shear stress at the bottom due to the proximity to the river bed.

However, differences between the two profiles arise when near-bank measurements are considered. In the case of $M1_2$, shown in Figure 5.12a, points close to the right bank displayed the same profile as the central part. On the other hand, data from the left bank showed an inverted velocity profile with a reduction in water speed in depth. These situations are in line with the previous considerations that in the meander sections the lowest velocities were present in the inner bank and increase towards the outer side.

The reversal of the depth profiles near the shore was also observed on the left and right sides of the straight section, shown in Figure 5.12b. Once again, the highest velocities were located in the middle, increasing from the bottom to the surface.

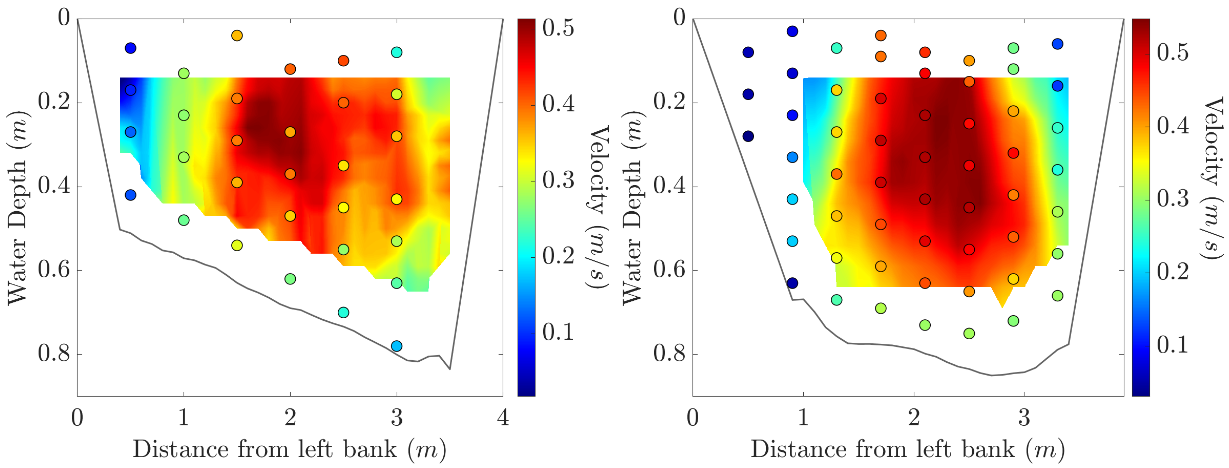

(a) $M1_2$ measured velocity *(b)* $S3$ measured velocity

Figure 5.12. Measured velocity through the water column for cross-sections (a) $M1_2$; and (b) $S3$, the bathymetry of each site is also displayed. ADCP velocity is represented by the interpolated surface, and the propeller velocities by the dots.

Finally, the percentage difference between the ADCP and propeller measurement was calculated for each cross-section, although considering only points from which measurements had been taken using both methods. The points taken with the propeller close to the bottom, surface or edges were excluded due to the lack of ADCP data to be compared against. In total, 92 out of 445 data points were found to share the same location and were used for the comparison.

There was significant variability in the measured velocities with respect to the ADCP data, as shown in Figure 5.13. There was an overall tendency for the ADCP to measure larger values compared to the propeller. When all cross-sections were considered together, the median difference was 9.23% with an interquartile range of 1.44 - 19.08%.

When every cross-section was considered individually, the percentage difference between values ranged from 0 to 48%, and up to 72% when outliers were considered. Moreover, in locations $M2_1$ and $S1$, the median was negative, meaning that for 50% of the measurements, the propeller had larger values than the ADCP data. Besides, the correlation coefficient was calculated as equal to 0.72.

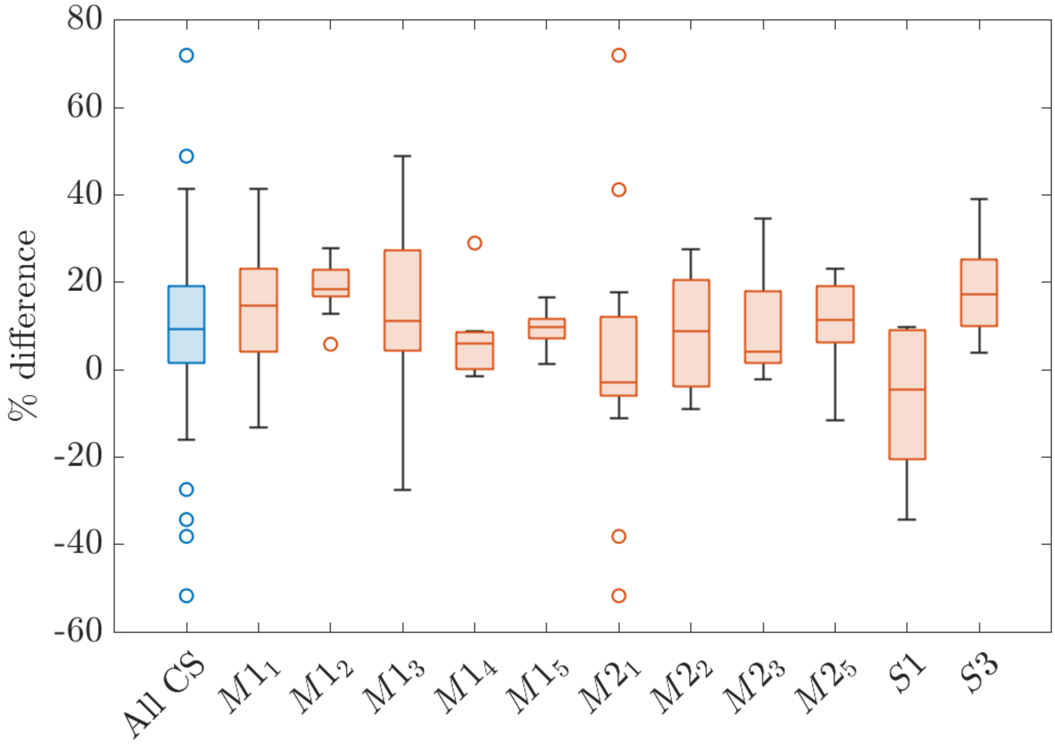

Figure 5.13. Box plot of the percentage difference between measured velocities by ADCP and propeller for data of all cross-sections together and grouped by location. Line inside the box shows the median; box limits display 25 and 75 quartiles, dotes are values outside 1.5 times the range interquartile, and whiskers limits represent maximum and minimum values. CS = Cross-sections.

Moreover, the velocity distribution coefficient (α) was calculated at each cross-section with the propeller and ADCP data. As was mentioned in Chapter 1, the velocity in a given cross-section of a stream tended to vary from point to point due to stream bed roughness, degree of sinuosity, obstructions, and other factors. As a result of this variation, the squared of the mean velocity can be lower than the weighted average of the squares of the point velocities. Therefore, the velocity head calculated with the mean velocity may be lower than the real one. In order to overcome this problem, the velocity distribution coefficient (α) is introduced to compensate for the lower mean velocity value [Hulsing et al., 1966].

According to Brorsen and Larsen [2009], typical values of α are 2.00 in sections with a parabolic velocity profile like laminar flow in a circular pipe, 1.10 in sections with a logarithmic velocity profile like uniform turbulent flows and 1.00 in sections with the same velocity in all points of the sections like contracted cross-sections and turbulent flows. The α coefficient was estimated using Equation 5.1.

$$\alpha = \frac{\int v^3 dA}{V^3 A} \tag{5.1}$$

Where:

v	Point velocity $[m/s]$
dA	Differential element of area $[m^2]$
V	Mean velocity $[m/s]$
A	Total cross-sectional area $[m^2]$

The results of α calculated with the propeller current meter and the ADCP exhibited differences visualized in a scatter plot in Figure 5.14. All the measurements were displaced downwards of the line of perfect agreement. This suggests that the propeller α tended to be higher than the ADCP α, although there was still a linear correlation between the two methods. Regardless of the method, no correlation was observed between the magnitude of α and the position of the cross-section.

Moreover, the range of α obtained with the propeller data was between 1.14 - 1.91, with an average value of 1.44. On the other hand, the α calculated with ADCP data was in the range of 1.02 - 1.43 and an average of 1.19. Meanwhile, the percentage difference between the propeller and ADCP α values ranged from 7 - 33%, with an average of 20%. The values of the calculated α with each method are shown in Table D.3, in Appendix D.

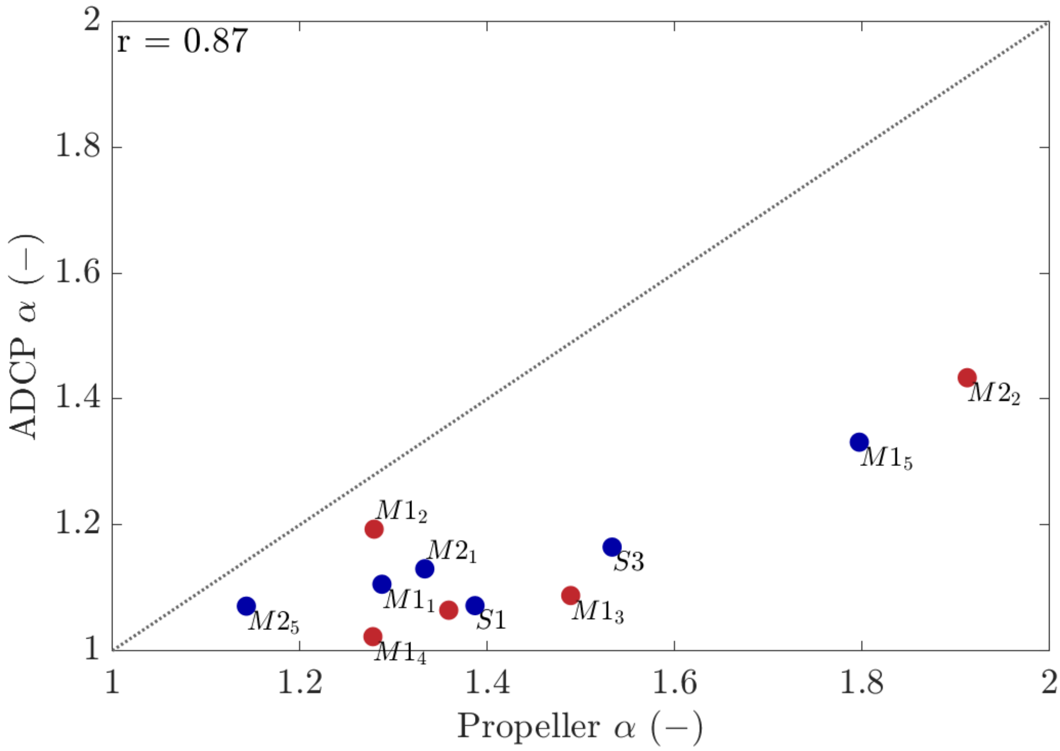

Figure 5.14. Scatter plot of the velocity distribution coefficient (α) calculated with propeller and ADCP data, with the line of perfect agreement. Planes in or adjacent to straight sections are highlighted in blue. The correlation coefficient (r) is also displayed.

5.6 Discussion of methods comparison

The two compared methods used to obtain water flow, velocity and bathymetry have their particular advantages and drawbacks. The propeller current meter method is one of the most broadly used around the world due to its simplicity and low cost. Its accuracy is highly dependent on the ability to measure the particularities of the cross-section by defining an appropriate measurement grid. This can be done by taking velocity data within small intervals both in the horizontal and vertical direction or by refining the grid in those areas where the flow presents sudden changes. However, as the density of sampling increases, the required time rises drastically. Despite making an adequately refined sampling grid, the measured velocities could easily be over or underestimated, especially if the sampling is taking place in a bend. This is due to the complex flow patterns taking place in the meander, the presence of secondary and counter-current flows, and non-uniform velocity patterns, making measuring the stream-wise velocity correctly problematic. For this reason, it is recommended to measure in a straight section of any stream studied.

The ADCP provides a rapid way of sampling. Once the equipment is established in the desired location, it takes approximately 15 minutes to obtain all the desired data. Another advantage is the amount of data that is collected at once. Not only the velocity vectors in three directions were obtained, but also discharge, stream-bed depth, geo-location of measurements, the width of the section, and duration of sampling, among others. The resolution of these data is also higher than what the propeller current meter can provide. This volume of data makes the ADCP highly versatile and able to be applied in different projects with fewer fieldwork efforts. Besides, the ability to measure the velocity vectors both in magnitude and direction allows the use of the ADCP in a wider range of stream conditions, whether it be in straight or meandering sections.

Choosing two consecutive bends for examination would be ideal to ensure a more comprehensive analysis. This approach enables a sequential evaluation, considering the variations in flow dynamics and stream geometries between consecutive bends. However, in this particular study, the selection of meanders was based on their uniform, regular shapes as opposed to the irregularities observed in the intermediate meanders. The presence of these irregularities within the intermediate meanders would introduce complexities and challenges in accurately assessing the performance of the instruments.

In areas where flow measurements are unavailable, careful consideration must be given to selecting constants for estimation. This is particularly important in narrow streams where the near-bank flow contributes significantly to the total flow. The QRev extrapolation process introduces uncertainty due to its reliance on predetermined default criteria. Reviewing and validating the chosen fit is crucial to ensure its suitability for the specific profile under analysis. However, this manual review introduces subjectivity and the possibility of human error, which can affect the accuracy of the extrapolation.

Additionally, combining all transects into a single normalized plot and selecting the best-fit extrapolation relies on a discharge-weighted median. Although this approach considers the relative measured discharge of each ensemble, it assumes that the measured discharge accurately represents the flow dynamics of the entire cross-section. Any errors or inconsistencies in the measured discharge values can impact the weighting and, consequently, the accuracy of the best-fit extrapolation.

In the case of both methods, the flow calculated between edge measurements and the bank itself is decided by linear interpolation. This means that the further the last measurement is taken from the bank, the greater the disparity between the calculated flow and the real-world conditions in this region. This can be particularly problematic in areas with lots of vegetation at the bank, preventing both the propeller and ADCP from being placed directly adjacent to the bank. However, the higher resolution in ADCP data reduces the uncertainty in these areas. Furthermore, the near-bank extrapolation method of the ADCP permits the consideration of an obstruction factor. This factor has to be carefully thought out based on all the flow limiting factors, such as vegetation and shoaling, observed at the banks of the stream.

The data processing with the ADCP could be a more laborious and time-consuming process than the propeller. However, a set of software exists to make this task easier and ensure the quality of the data. Using these made it possible to get the best extrapolation fit for the upper and lower part and provide suggestions on how the constants near the bank should be chosen. Once the quality of the data is ensured, they provide velocity profiles and bathymetry data ready to be used within a few seconds. Therefore, it would depend on the specific objective of the investigation but in general, most of the required data can be extracted and applied relatively fast.

A tendency of higher flow and velocity values recorded by the ADCP compared with the propeller was observed. This may have been due to most sampling being done in curved parts of the stream resulting in an underestimation of the velocities by the propeller and, therefore, the flow, as seen in Sections 5.3 and 5.5. As it was also pointed out, in the two straight sections, the differences in flow and velocity between methods were, in general, lower. This difference in velocities between methods at different locations may be attributed to the fact that in a meandering stream, it can be difficult to determine the exact direction of the stream-wise velocity, hence making it more difficult to obtain accurate results with a propeller compared with a straight section. The ADCP automates this process and provides the velocity regardless of the shape of the stream.

The shape of the horizontal velocity profile, with higher velocities towards the centre of the stream, could be explained by the higher resistance to flow due to friction with the stream bed substrate and the larger presence of vegetation.

Similarly, an inversion of the vertical velocity profile in depth was present near to the shore. This change in depth may be the result of the higher abundance of macrophytes at the banks nearest to the surface.

Higher α values were obtained when the propeller current meter measurements were used for the calculations. This may be the consequence of the lower number of measuring points done by the propeller method, resulting in a larger variability of the velocity from one point to another and a larger area of influence of each point. Using the ADCP method the area of influence of each velocity point was lower due to the higher density of points. This density of points likely generated a better representation of the velocity distribution in the cross-sections. The calculation of the weighted velocity based on the ADCP data could, therefore, also be assumed to be more accurate.

The α values obtained from the ADCP data were closer to what might be expected in an open channel with turbulent flow. This could also be verified by looking at the velocity distribution plots in Appendix C. In those profiles with a uniform distribution of the velocities, the calculated alpha was closer to 1, while those profiles with larger variability of the velocity distribution displayed higher α values.

Unfortunately, there was no volumetric flow data available from the "10.17 Binderup Å, Ns Binderup Mølle" station (see Chapter 4) during the fieldwork period. However, water level data was available and showed that the water level fluctuated from 1.85-1.92 meters at this station. Historically, the flow corresponding to this range of water level was between 0.7-0.8 m^3/s, as seen in Figure 5.15. Results from the ADCP were inside this range. Despite this station being located 2 km upstream from the Cabin St., and the possibility of lateral inflow into Binderup Å, it was assumed that the flow at both locations was approximately the same.

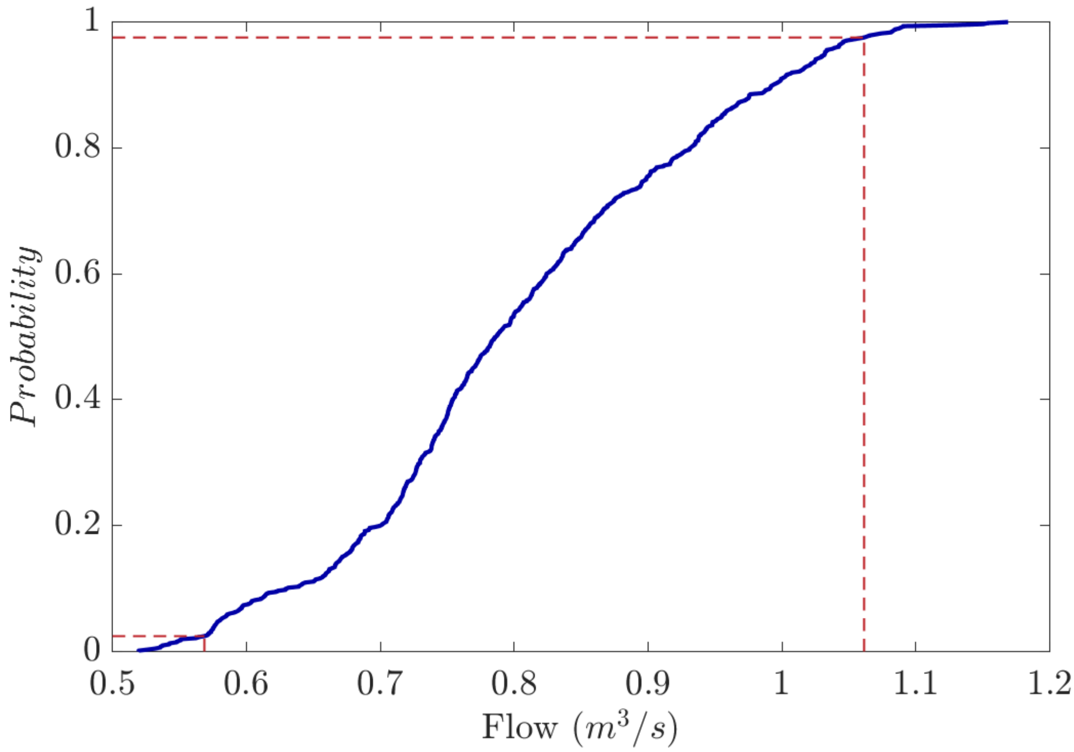

Figure 5.15. Cumulative density function for the water flow at "10.17 Binderup Å, Ns Binderup Mølle" when the water level was between 1.85-1.92 m, between 2012-2021.[WSP and Miljøstyrelsen]. 95 % confidence interval is delimited by red dashed lines.

Regarding bathymetry, both methods showed similar results. The high sampling resolution of the ADCP makes it a better option when a higher resolution description of the streambed is required, with no significant increase in the measuring time. As four different sound beams measure the depth, the error produced by any interference is reduced. Besides, the data provided by the ADCP can be imported into GIS and modelling software for further analysis.

Additionally, its high-resolution depth measurements provide the accurate information needed to calculate area, wetted perimeter and hydraulic radius. Further, the availability of area, wetted perimeter and hydraulic radius data derived from the ADCP measurements allows for a more robust characterization of the stream cross-section, providing valuable inputs for assessing a stream's hydrodynamic processes. In contrast, the propeller current meter method does not directly provide information on area, wetted perimeter and hydraulic radius. Its focus is primarily on obtaining velocity data. Therefore, the ADCP method offers a distinct advantage by providing not only depth measurements but also the ability to calculate key hydraulic parameters. Furthermore, it was possible to observe that the cross-sectional area and wetted perimeter of the stream get increased at the apex position. This may be correlated with the expected sediment dynamics of erosion at the outer bank and sediment at the inner and have their larger influence at this part of the stream.

5.7 Conclusion of methods comparison

Overall, the ADCP was found to be a more versatile and efficient method for measuring flow data in a stream. The bathymetry measured using the ADCP had an average difference of 5% to the ones measured using the propeller. The ADCP measured flow measurements 7.45% higher than the propeller on average. The maximum difference in flow measurements was found in the meandering sections of the stream, indicating a greater disparity between methods in these sections. Due to the nature of the way the ADCP measures flow, it was assumed to be more reliable in bends. The difference in measured median velocities was 10% between the methods, attributed to the limitations of the propeller. Therefore, the data obtained with the ADCP was considered valid and applicable for further analyses of the hydraulic conditions in Binderup Å.

Evaluation of Hydraulic Properties 6

As previously mentioned, determining the roughness in a stream is a difficult task, one which becomes even more challenging in meandering streams due to the particularities of the velocity distribution in these areas.

In order to address this challenge, a 1-D hydrodynamic model constructed in HEC-RAS was developed, using flow, water level, and bathymetry measurements obtained at Binderup Å to compare the hydraulic properties of straight and meandering sections of the stream at various flow conditions. The results obtained from the model were compared with the roughness coefficient at the reaches calculated by the well-known Manning's equation and with the NCALC model developed by the United States Geological Survey (USGS) [Dalrymple and Benson, 1967], which considers the impacts of the changes in the cross-sectional area throughout the reach. The impacts of the variation in roughness coefficient on water depth were assessed using the built HEC-RAS model for both meander and straight sections.

Finally, the impact of the uncertainty in the discharge measurements error by the ADCP on the roughness coefficient was estimated by performing a Monte Carlo simulation, considering the probability distribution of the two flow data sets obtained during the field days.

6.1 HEC-RAS 1-D model presentation

The Hydrologic Engineering Center's River Analysis System (HEC-RAS), developed by the U.S. Army Corps of Engineers, is a software capable of performing a range of one and two-dimensional hydraulic modelling [US Army Corps of Engineers, 2022].

The basic computational procedure is based on solving the one-dimensional energy equation, which evaluates energy losses due to friction and contraction/expansion. In situations where the water surface profile rapidly varies, the momentum equation is also utilized, as described in Appendix E.

For this project, the one-dimensional steady flow analysis was used. This component of the modelling system is intended for calculating water surface profiles for steady gradually varied flow.

6.1.1 Terrain model and model geometry

The model construction process involved several steps in accurately representing the Binderrup Å river's topography. The first step was to combine the bathymetry data collected with the ADCP and a SCALGO elevation model from 2021 [SCALGO] into a single digital elevation model. The ADCP was used to collect bathymetry data along 83 transects, which were then linearly interpolated to generate a bathymetry surface corresponding to the stream bed, with a resolution of 0.1 meters. However, due to insufficient bank elevation data obtained from the ADCP data, the SCALGO terrain elevation model was used as supplemental data. The SCALGO model had a spatial resolution of 0.4 meters, which provided accurate terrain elevation data for the project site. The next step involved merging the two terrain models to create a unique terrain model that incorporated the elevation of both banks and channels, as shown in Figure 6.1.

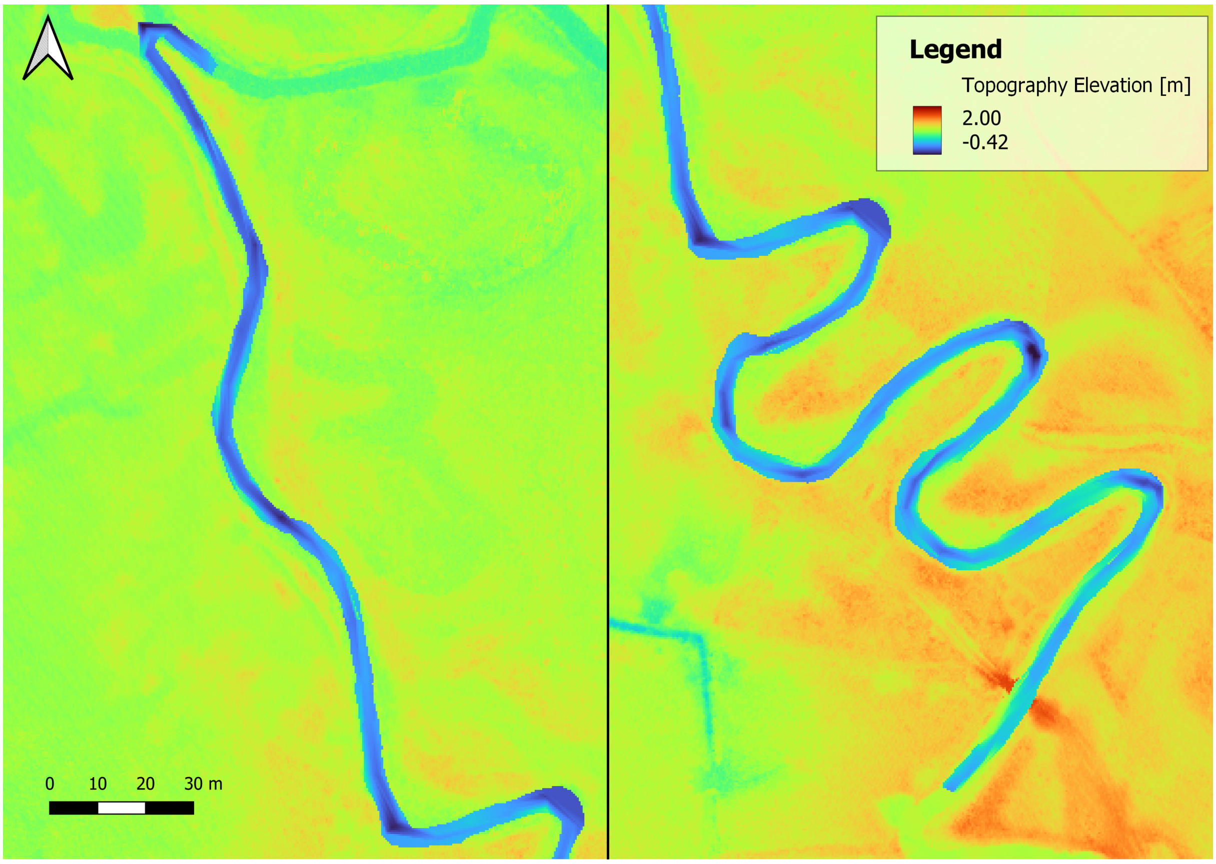

Figure 6.1. Digital Elevation Model of Binderup Å created from ADCP measurements and SCALGO data. Left side of the figure shows the straight portion of the stream, and the right side the meandering.

This terrain model was then used to construct the model geometry using the RASMapper which is a feature within HEC-RAS that facilitates the construction of the model geometry by utilizing the provided terrain data. The geometry included the river schematic and cross-sections. The schematic illustrated the flow path of the river, which was established by drawing the river's central flow line and the bank lines of the stream.

To accurately represent the actual conditions of the river, 74 cross-sections were generated over a total stream distance equating to 509 meters. Each cross-section was located at the same position as the transects taken with the ADCP and had the ground surface profiles of the previously generated terrain model. In this case, it was believed that the number of generated cross-sections provided a good representation of the changes in the cross-sectional area. The meandered reach of the stream was defined as the stretch between cross-section number 509 to 180 and the straight reach from 169 to 1, see Figure 6.2.

Figure 6.2. Geometry of 1-D HEC-RAS model. Meandering area is delimited by cross-sections (CS) 509 to 180; and straight by CS 169 - 1.

6.1.2 Steady flow data

Steady flow data required for the model consisted of flow regime, discharge information (flow data from a specific instance in time), and boundary conditions [US Army Corps of Engineers, 2022].

The sub-critical flow was selected as the flow regime because it is commonly present in natural channels with flat slopes and low velocities along the stream, as described for Binderup Å at Chapter 4.

Next, the discharge information was applied to the most upstream cross-section of the model. The average value of the flows obtained during the field days, found in Tables B.4 and B.5, was selected. For low flow conditions, a discharge of 0.74 m^3/s, while 1.45 m^3/s was used for higher flow conditions.

Finally, the boundary conditions necessary for establishing the water surface at each end of the system were selected. An initial water surface is necessary for the program to begin the calculations. In a sub-critical flow regime, boundary conditions are only necessary at the downstream ends of the river system. There are different possibilities for the selection of the boundary condition, such as Known Water Surface Elevation, Critical Depth, Normal Depth, and Rating Curve. In this model, the Normal Depth condition was selected. For this type of boundary condition, it was required to enter an energy slope to calculate normal depth (using Manning's equation) at the outlet. The energy slope is approximated using the channel's average bathymetric slope or the water surface's average slope near the cross-section. In this case, the bathymetric slope measured in the final stretch of the meandering section, 0.6 ‰, was selected.

6.1.3 Model verification: low-flow conditions

The model was calibrated by adjusting primary model parameters to ensure the results of the model best reflected the observed conditions in low flow conditions, see Figure 4.8.

According to US Army Corps of Engineers [2022], the parameter with the most significant impact on the model's results was Manning's roughness coefficient (n). The value of n can be individually selected for each cross-section, yet for the purpose of this project, a single unique value was selected for each of the meandering (n_M) and straight (n_S) sections. In order to find the best combination of these coefficients, a simple parameter calibration was conducted. A data set of 8,278 equally spaced n_M and n_S values were created. These data sets ranged from 0.01 to 0.1 $s/m^{1/3}$ (M = 100 - 10), each value in the data set spaced from each other by 0.001 $s/m^{1/3}$ (M = 0.0109). Consequently, the model was run iteratively, with roughness values changed one at a time. For each value of n_M, the model was run for each value of n_S, until all combinations had been tested. This process was then repeated for the next n_M value until the whole data set was covered.

For each combination of n_M and n_S values, the observed and modelled water levels were compared using the Nash-Sutcliffe Model Accuracy Metric (NSE). The NSE ranges from $-\infty$ to 1, where a value equal to 1 is a perfect agreement between observations and model results, a value of 0 shows that the model is just as accurate as the mean of the observations, and a negative NSE value means that it is better to use the mean value of the observations as a predictor rather than the model results [Nash and Sutcliffe, 1970].

The calculated NSE for the different roughness coefficient combinations is shown in Figure 6.3. The best-fit combination was obtained with a n_M of 0.051 $s/m^{1/3}$ (M = 19) and a n_S of 0.041 $s/m^{1/3}$ (M = 24). This means a higher resistance was present in the meandering part of the reach compared to the straight section. The models displayed a higher sensitivity towards n_S, with a variation of ± 27% from the best-fit value leading to negative NSE, while in the case of n_M a variation of ± 80% from the best-fit value was necessary to get negative NSE.

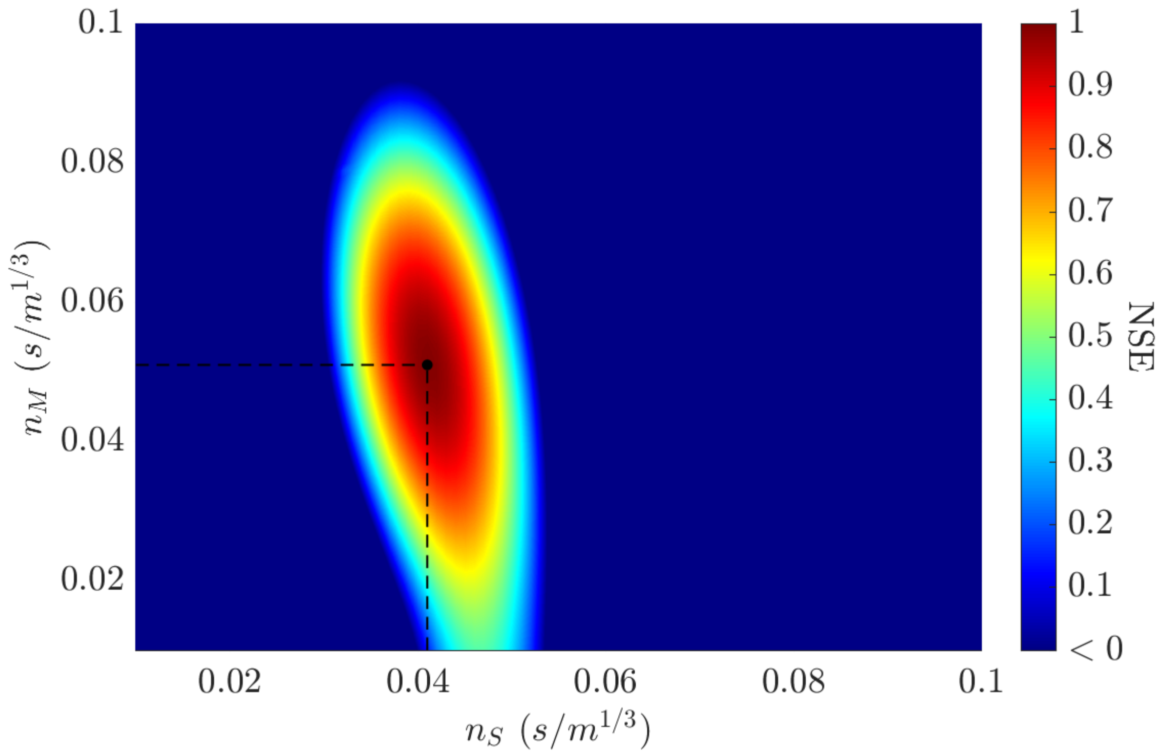

Figure 6.3. NSE heat map of the roughness coefficient calibration, the black dot shows the best combination of n_S and n_M at 0.041 (M = 24) and 0.051 (M = 19) $s/m^{1/3}$, respectively.

Figure 6.4 shows a high correlation between the modelled and observed water surface elevation when using the best-fit combination of roughness coefficients. A mean absolute difference of 0.0044 meters was observed between data sets, with the highest difference of 0.0122 meters.

The model demonstrated a capability to represent the measured water levels at Binderup Å with high accuracy and precision for the low flow conditions. Furthermore, HEC-RAS seemed to be greatly sensitive to roughness coefficient selection, at least for the modelling of simple natural steam, with no junctions or man-made structures.

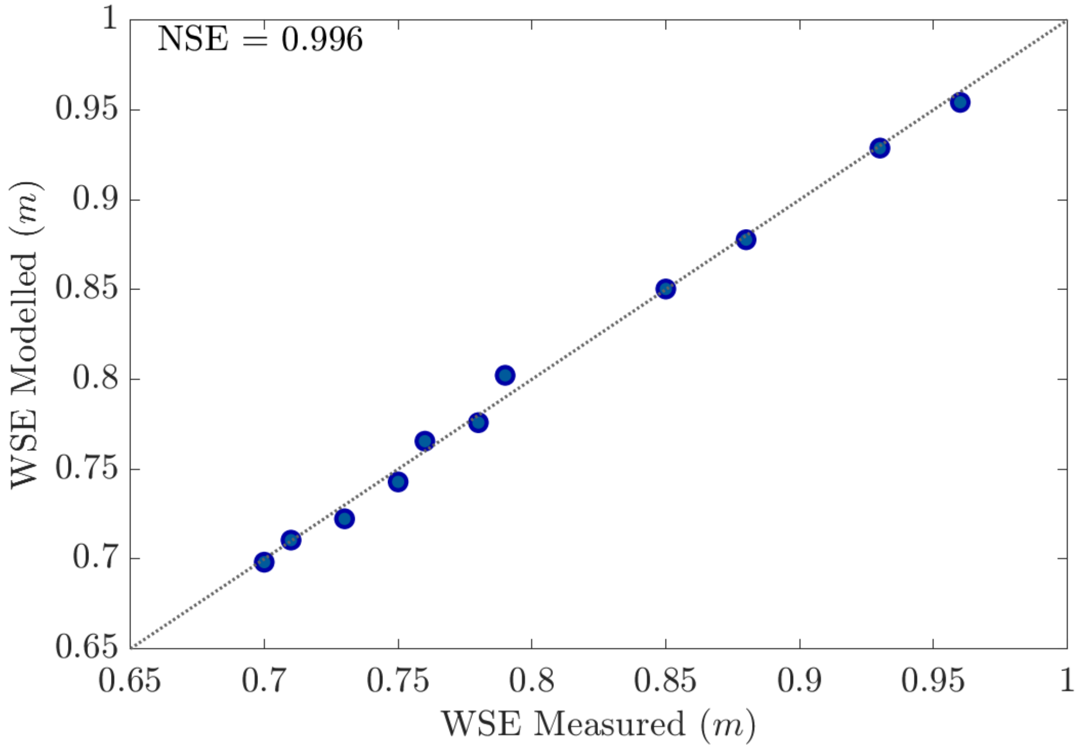

Figure 6.4. Scatter plot of the measured and modelled water surface elevation (WSE) for the best-fit combination of n_S and n_M to the low flow conditions.

6.1.4 Model verification: high-flow conditions

The hydrodynamic model was used to represent the observed water level conditions under high flow. The same procedure as before was followed, and the best combination of n values was obtained. In this case, the model used data from the second field day, in which higher flow conditions (1.45 m^3/s) were observed. Similarly to the low-flow process, the water surface elevation values were compared between the measured and modelled results. NSE values were calculated for each combination of n as illustrated in Figure 6.5.

The best-fit combination was obtained with a n_M of 0.050 $s/m^{1/3}$ (M = 20) and a n_S of 0.039 $s/m^{1/3}$ (M = 25). This means that the same behaviour as in low flow was observed. Higher resistance was present in the meandering part of the reach compared to the straight section. Once again, the models displayed a higher sensitivity towards n_S, with a variation of ± 15% from the best-fit value leading to negative NSE, while in the case of n_M a variation of ± 80% from the best-fit value was necessary to get negative NSE. Under these flow conditions, the model showed a higher sensitivity to the change in n_S than for lower flow.

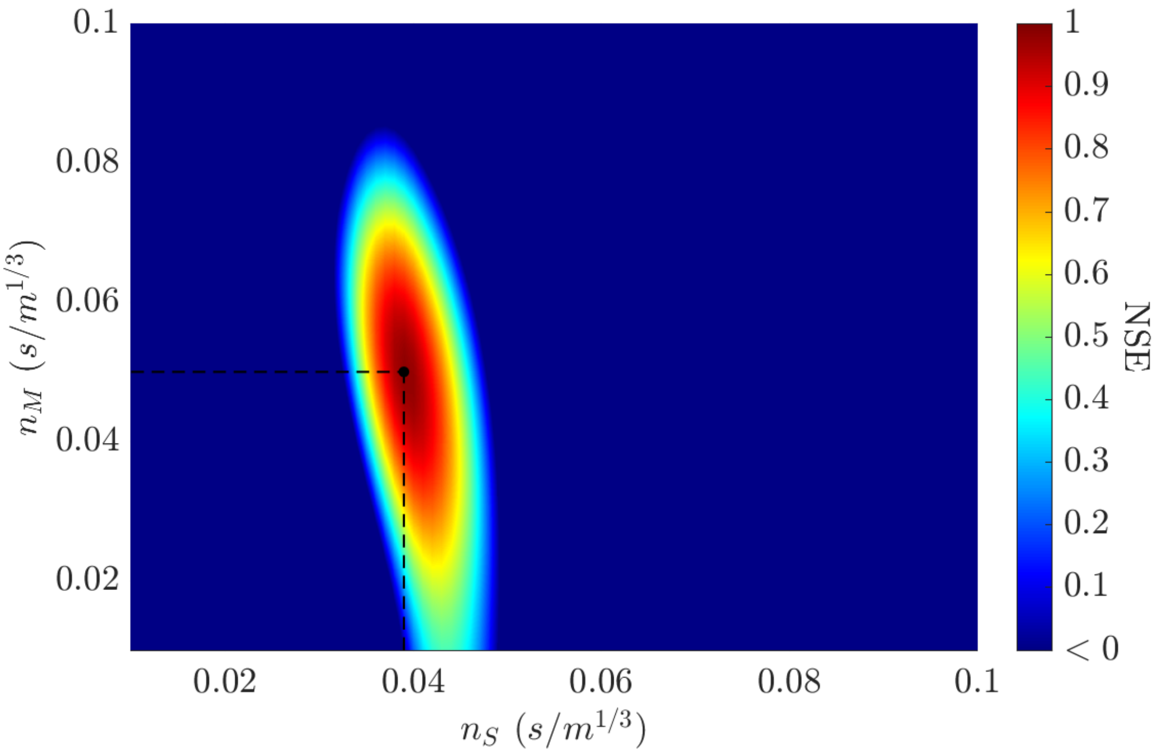

Figure 6.5. NSE heat map of the roughness coefficient calibration, the black dot shows the best combination of n_S and n_M at 0.039 (M = 20) and 0.050 (M = 20) $s/m^{1/3}$, respectively.

The correlation between modelled and observed water levels under high flow conditions when using the best-fit combination of roughness coefficients is illustrated in Figure 6.6. A mean absolute difference of 0.0086 meters was observed between data sets, with the highest difference of 0.0219 meters.

The model showed a slight tendency to underestimate the water level along the stream for the high-flow conditions, as illustrated in Figure 6.6. However, the NSE indicates a significant level of agreement between observation and model results. The model exhibited more substantial differences in proximity to its upper boundary and within the meander section of the stream, despite its ability to accurately represent water level fluctuations in the straight section with a higher degree of precision.

The model demonstrated a high level of accuracy in representing observed water surface levels during both low and high-flow conditions. As such, the model is capable of accurately representing the observed conditions. However, the accuracy of prediction was slightly lower than for the low-flow conditions.

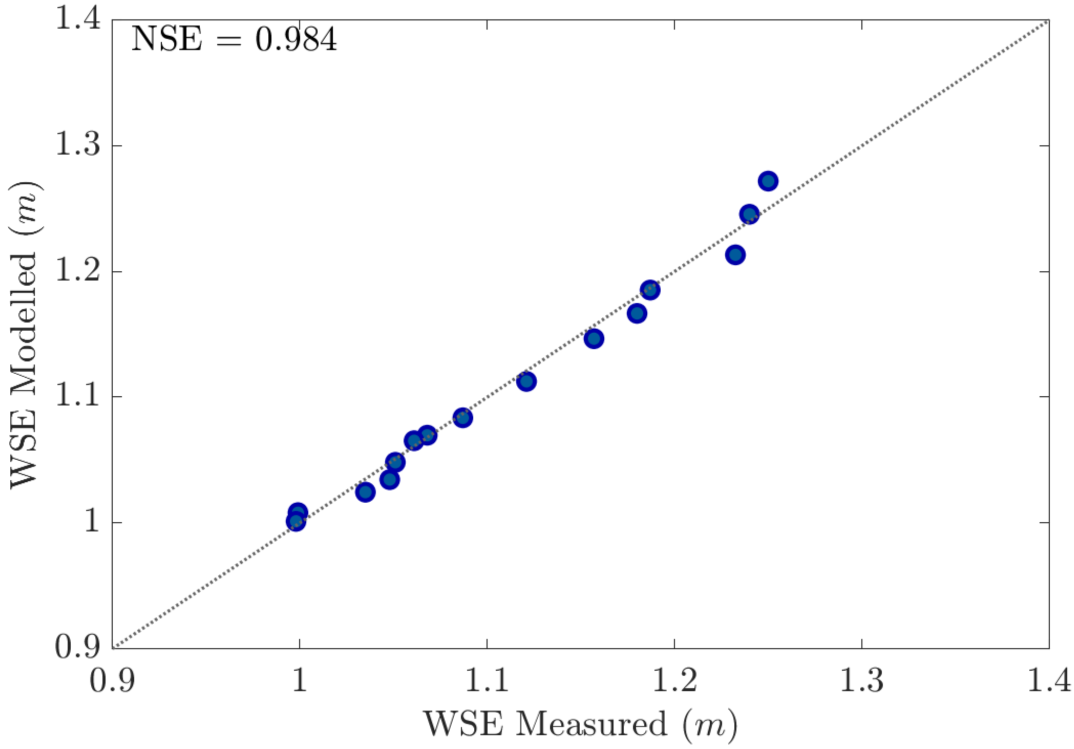

Figure 6.6. Scatter plot of the measured and modelled water surface elevation (WSE) of the model at higher flow conditions.

6.2 Hydrodynamic variables analysis

The model was used to analyze the hydraulic characteristics of the stream between discharge rates of 0.74 to 1.45 m^3/s. The model was executed using ten flows evenly distributed across the aforementioned range, and hydraulic properties were evaluated by comparing the averaged wetted perimeter, cross-sectional area, hydraulic radius, and velocity within meandering and straight sections of the stream. For the comparison, the average value of each property of all cross-sections within the meandering and straight sections was used. Regarding the roughness coefficient, a linear interpolation between the previously obtained for low and high flow was done, and a new pair of n_S and n_M was obtained for each flow condition.

Figure 6.7 illustrates the variability of hydraulic characteristics. In terms of geometric variables, the cross-sectional area demonstrated a linear increase proportional to flow in both meandering and straight sections, with the meandering section consistently exhibiting higher area values across all flows as shown in Figure 6.7a. Moreover, as flow rates increased, the disparity in the area between meandering and straight sections also increased.

The wetted perimeter demonstrated a linear increase in both sections up to a flow rate of 1.21 m^3/s, with the meandering section displaying higher values. After this point, the increase became exponential, with a steeper slope for the straight section, as displayed in Figure 6.7b. As a result, for the final modelled point, the wetted perimeter of the straight section was almost the same as that of the meandering section. This increase in slope coincided with the point when the water level reached the banks, resulting in a greater volume of water distributed over a larger surface area and hence a larger wetted perimeter.

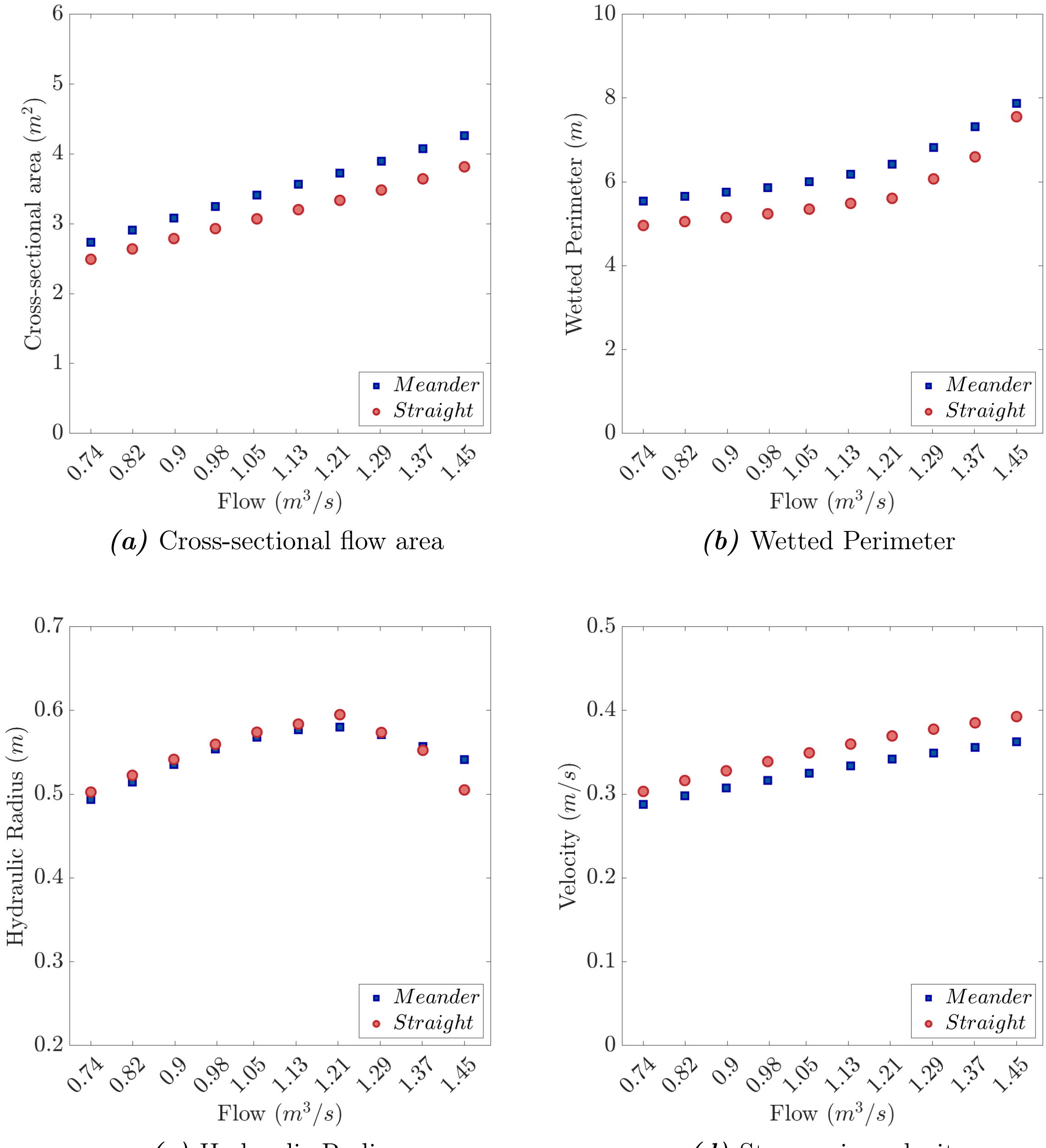

(a) Cross-sectional flow area ***(b)*** Wetted Perimeter

(c) Hydraulic Radius ***(d)*** Streamwise velocity

Figure 6.7. Modeled hydraulic properties for both meandering and straight portions of the stream with different flow conditions.

In the range from low flow to a flow of 1.21 m^3/s, the hydraulic radius increased with higher flow rates because the increment in the cross-sectional area was more significant than the rise in the wetted perimeter at each step. This behaviour was comparable for both meandering and straight sections, as demonstrated in Figure 6.7c. However, after this point, due to the exponential surge in wetted perimeter exceeding 1.21 m^3/s, the hydraulic radius rapidly decreased for both sections, though at a greater rate in the straight section.

Furthermore, for each flow condition the streamwise velocity in the straight section consistently exceeded that in the meandering section, as illustrated in Figure 6.7d. As the velocities in both sections increased with rising flow rates, so did the difference in velocity between sections.

6.3 Comparison of roughness coefficient

Manning's equation and the NCALC method were employed to estimate Manning's roughness coefficient for both meandered and straight reaches of Binderup Å. These approaches were chosen because they allow for the direct calculation of the coefficient n from the measured water level, discharge data, and geometric parameters of the cross-sections. Furthermore, these selected methods are independent of subjective estimations such as look-up table methods and are not influenced by the grain size distribution.

Assuming uniform steady-state flow, where water-surface slope, friction slope and energy gradient are parallel to the stream bed and the area, hydraulic radius, and depth remain relatively constant throughout the stream reach, discharge can be computed with Manning's formula (Equation 6.1) [Jarrett and Petsch Jr., 1985].

$$Q = \frac{1}{n} \cdot A \cdot R^{2/3} \cdot I^{1/2} \tag{6.1}$$

Q	Discharge $[m^3/s]$
n	Roughness coefficient $[s^3/m^{1/3}]$
A	Cross-sectional area $[m^2]$
R	Hydraulic Radius $[m]$
I	Energy gradient or friction slope $[m/m]$

In the absence of a more appropriate method, it is commonly presumed that the equation remains applicable to nonuniform reaches, which are frequently present in natural channels when the energy gradient is adjusted to consider the losses resulting from boundary friction (h_f) [Barnes, 1967]. In such cases, the friction slope must be determined by employing Equation 6.3, based on the Energy Equation 6.2. A sketch of the energy change between two cross-sections is displayed in Figure 6.8.

$$h_1 + h_{v1} = h_2 + h_{v2} + h_f + k(\Delta h_v) \tag{6.2}$$

Where:

h	Surface elevation above common datum at the respective section $[m]$
h_v	Velocity head at the respective section $= \alpha v^2/2g$ $[m]$
α	Velocity distribution coefficient [-]
v	Average cross-section velocity $[m/s]$
g	Gravitational acceleration $[m/s^2]$
h_f	Energy loss due to boundary friction in the reach $[m]$
$k(\Delta h_v)$	Energy loss due to acceleration of velocity in a contracting reach, or deceleration of velocity in an expanding reach $[m]$
k	Coefficient generally assumed to be equal to 0 for contracting reaches, and equal to 0.5 for expanding reaches [Barnes, 1967].

Therefore, the friction slope is defined as:

$$I = \frac{h_f}{L} = \frac{\Delta h + \Delta h_v - k(\Delta h_v)}{L} \tag{6.3}$$

Where:

Δh	Difference in water-surface elevation at the two sections $[m]$
Δh_v	Upstream-velocity head minus downstream-velocity head $[m]$
$k(\Delta h_v)$	Energy loss due to acceleration of velocity in a contracting reach, or deceleration of velocity in an expanding reach $[m]$
L	Length of the reach $[m]$

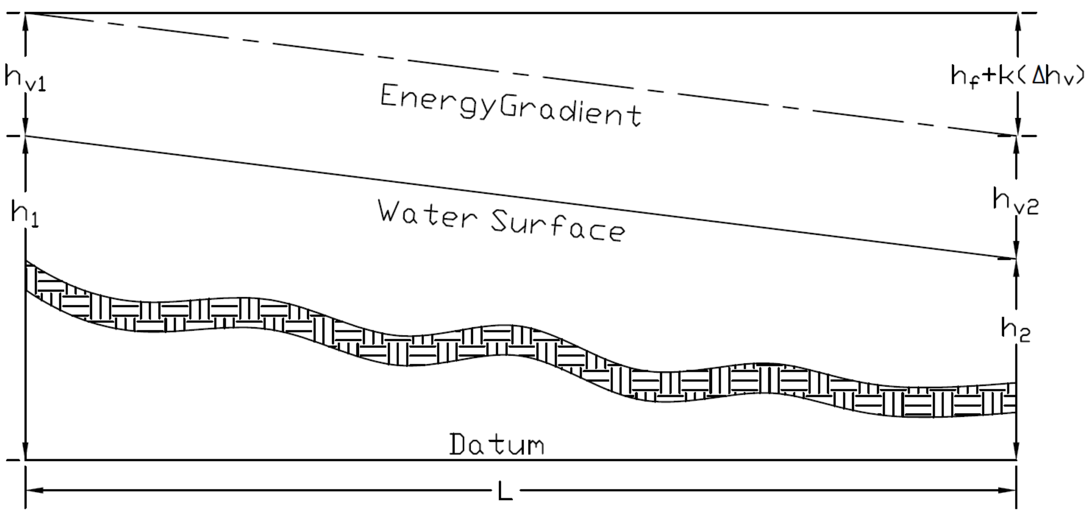

Figure 6.8. Sketch of energy change between two cross-sections.

Alternatively, the NCALC method [Jarrett and Petsch Jr., 1985], developed by the United States Geological Survey (USGS), is applicable when multiple cross-sections along the stream are accessible, enabling the consideration of changes in cross-sectional parameters such as area and hydraulic radius, as is seen in Figure 6.9. In this regard, Equation 6.4 was utilized to estimate the roughness coefficient using the NCALC method.

$$n = \frac{1}{Q}\sqrt{\frac{(h_1 + h_{v1}) - (h_M + h_{vM}) - \sum_{i=2}^{M}(k_{i-1,i}\Delta h_{v_{i-1,i}})}{\sum_{i=2}^{M}\frac{L_{i-1,i}}{Z_{i-1}Z_i}}} \tag{6.4}$$

M	Number of cross-sections [-]
Q	Discharge $[m^3/s]$
$h_{1,M}$	Water-surface elevation at the first and last cross-sections, respectively $[m]$
$h_{v1,vM}$	Velocity head at the first and last cross-sections, respectively $[m]$
$k(\Delta h_v)$	Energy loss due to acceleration of velocity in a contracting reach, or deceleration of velocity in an expanding reach, between consecutive cross-sections $[m]$
L	Length between consecutive cross-sections $[m]$
Z	Equals to $AR^{2/3}$
A	Cross-sectional flow area $[m^2]$
R	Hydraulic radius of the cross-section $[m]$

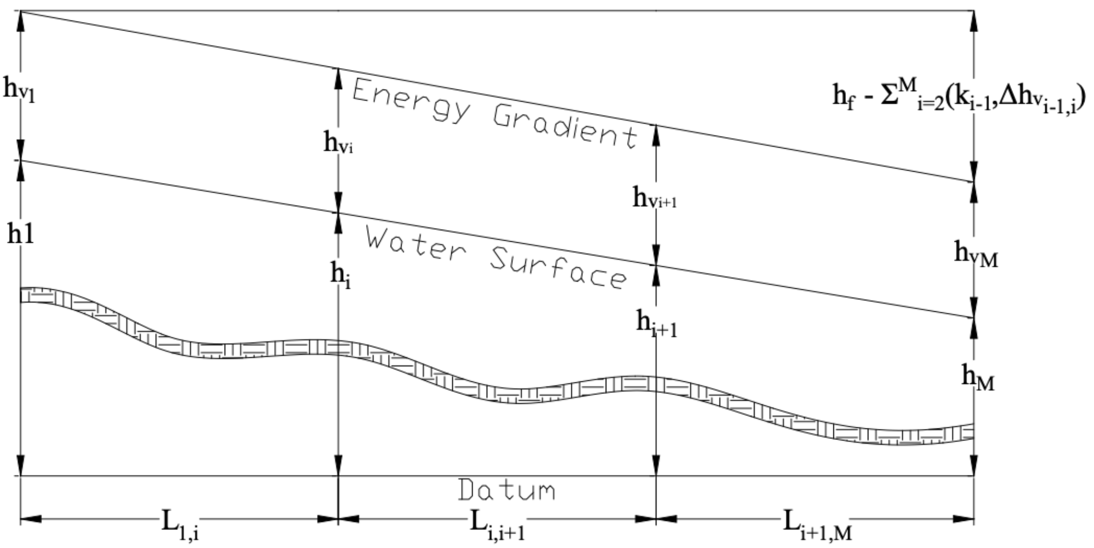

Figure 6.9. Schematic representation of the NCALC method for estimating roughness coefficients in stream flow analysis.

The ADCP data collected during the field days was used to perform the n calculations with the two selected methods. The water surface elevation at each cross-section was known, and the previously defined discharges of 0.74 and 1.45 m^3/sec were used.

For Manning's method, an average value of flow area and hydraulic radius was calculated with the area and radius of all the cross-sections belonging to the reach. However, for the calculation of the energy gradient, the change in energy between the first and last cross-section of each reach was considered.

For the NCALC method, the measured area and hydraulic radius at each cross-section was considered. Aside from the change in water surface elevation and velocity head between the first and last cross-sections, the energy change due to acceleration or deceleration of velocity between every transect belonging to the reach was included in the calculations.

In both methods, for the velocity-head estimation, the average velocity used was calculated by the division of the measured flow by the flow area in the transect, as the

ADCP data contains several portions where the velocity was unmeasured. The velocity distribution coefficients (α) were calculated for each cross-section, as shown in Chapter 5.5, and applied in the calculation of the velocity head of each of them.

6.3.1 Roughness Coefficient Results

The findings obtained during the field days were used to determine the value of n in the stream across the two flow conditions with Manning's and NCALC methods. Used cross-sections for the calculations at each condition are displayed in Figures 6.12 and 6.13. The results of n were subsequently compared with those obtained with the HEC-RAS model. As shown in Figure 6.10, the results indicate a decrease in n with increased flow for both meandering and straight sections, regardless of the estimation method.

Under low flow conditions in the meandering section, n was estimated to be 0.051 $s/m^{1/3}$ (M = 19.6) via both HEC-RAS and Manning's equation, and 0.048 $s/m^{1/3}$ (M = 20.8) using NCALC. Under high flow conditions, these values were 0.050, 0.047 and 0.044 $s/m^{1/3}$ (M = 20, 21.3 and 22.7), respectively. This equates to a reduction of 2%, 8.2%, and 8.9% in the meandering stretch, as per HEC-RAS, Manning's and NCALC methods, respectively.

In the straight sections, n was estimated to be 0.041 $s/m^{1/3}$ (M = 21.4) via HEC-RAS and 0.040 $s/m^{1/3}$ (M = 25) utilising both the Manning's and NCALC methods under low flow conditions. These same methods returned values 0.039, 0.034 and 0.035 $s/m^{1/3}$ (M = 25.6, 29.4 and 28.6) under high flow conditions, equating to a decrease of 4.9%, 15.8%, and 13.4%, respectively.

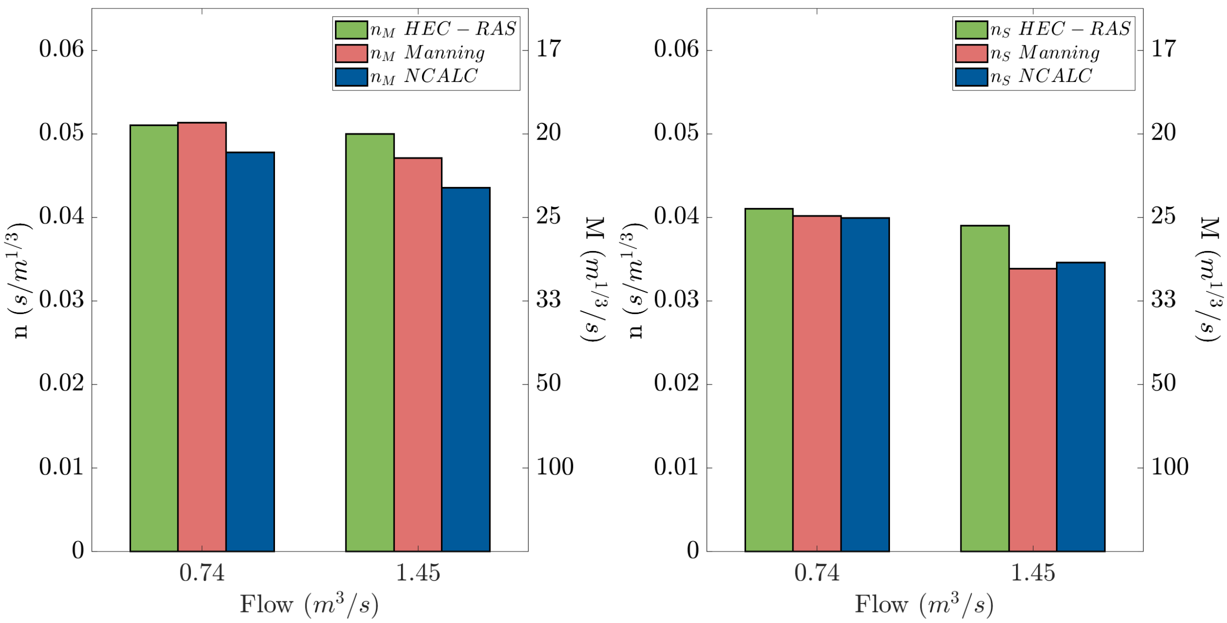

(a) Meandering Reach ***(b)*** Straight Reach

Figure 6.10. Variation of roughness coefficient with discharge estimated with HEC-RAS, Manning's equation, and NCALC method at the (a) meandering reach and (b) straight reach of Binderup Å.

The calculated percentage difference between straight and meandering sections with HEC-RAS was 25% and 28%, with low and high flow, respectively. Using Manning's method, a maximum difference of 28% was obtained for low flow and 39% for high flow conditions. The NCALC method displayed the lowest difference, with 20% and 26% under low and high flow conditions respectively. Additionally, the difference in n between meandering and straight sections rises from low to high discharge conditions, as displayed in Figure 6.11a.

This difference was translated to the conveyance, K, of the stream according to Equation 6.5. Considering an increase of between 20 - 39% of n in the straight section, the K of this section would be 17 - 28% lower.

$$K = \frac{1}{n} * A * R^{2/3} \tag{6.5}$$

Comparable roughness coefficients were computed for the three methods in the straight section for low flow conditions. However, during high flow conditions, slightly more significant roughness coefficients were obtained by HEC-RAS. In contrast, more noticeable differences between methods were observed at the meandering reach. As seen in Figure 6.11b, the NCALC method showed the lowest values of n between methods for both conditions, with a variance of 7% compared to the other two methods for low flow. At high flow conditions, the difference between NCALC and HEC-RAS was the highest, while smaller differences between Manning's and HEC-RAS were observed.

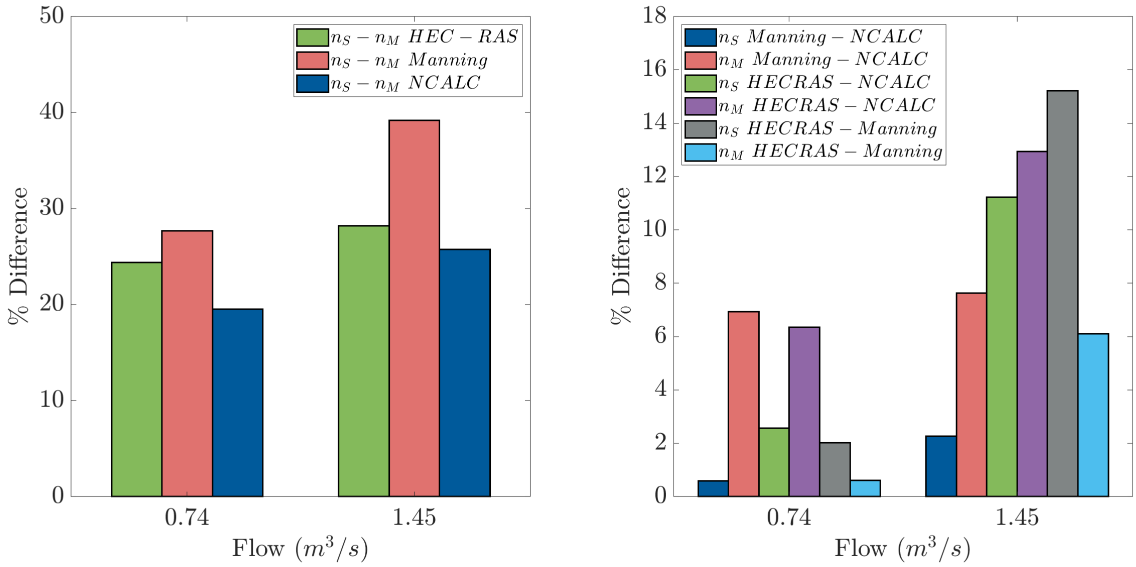

(a) Difference between straight and meander ***(b)*** Difference between methods

Figure 6.11. Percentage difference of n for (a) the two sections with different methods; and (b) at the same section with the different method.

As described in Section 6.3, several cross-sections can be considered in calculating the roughness coefficient in either method, although to varying degrees. To assess the impact of including more cross-sections in each method, the value of n was calculated with a progressively larger inclusion of the cross-sections shown in Figures 6.12 and 6.13.

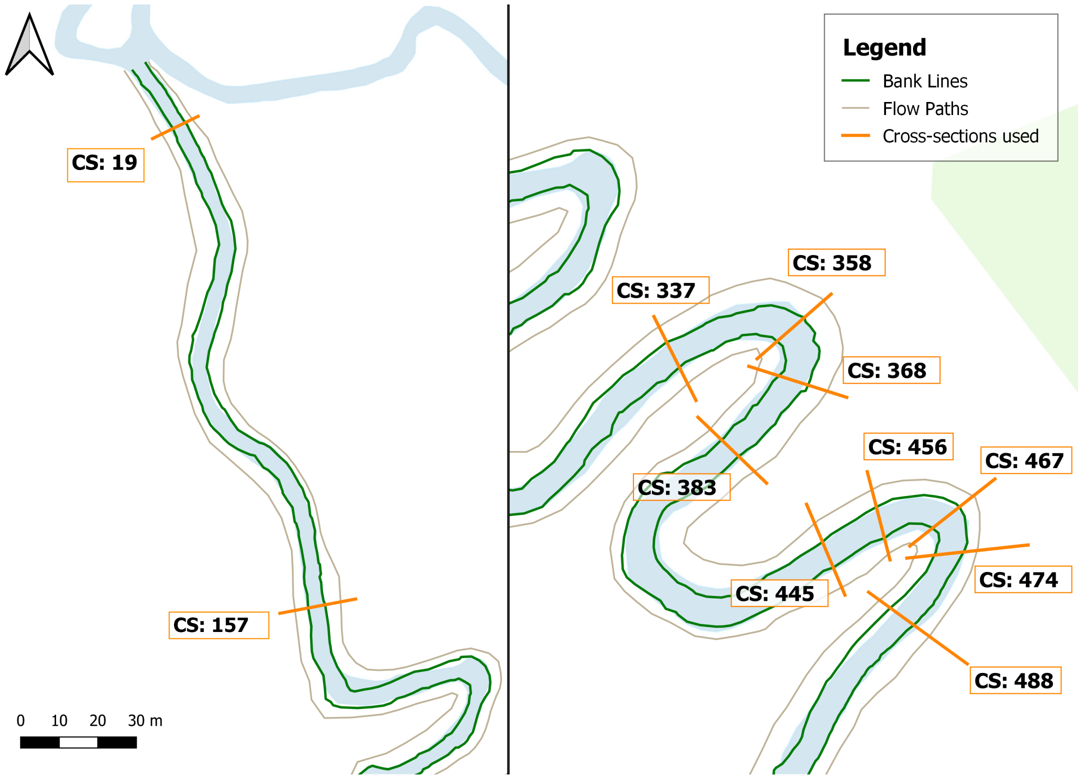

Figure 6.12. Cross-sections included in Manning's and NCALC calculations under low flow.

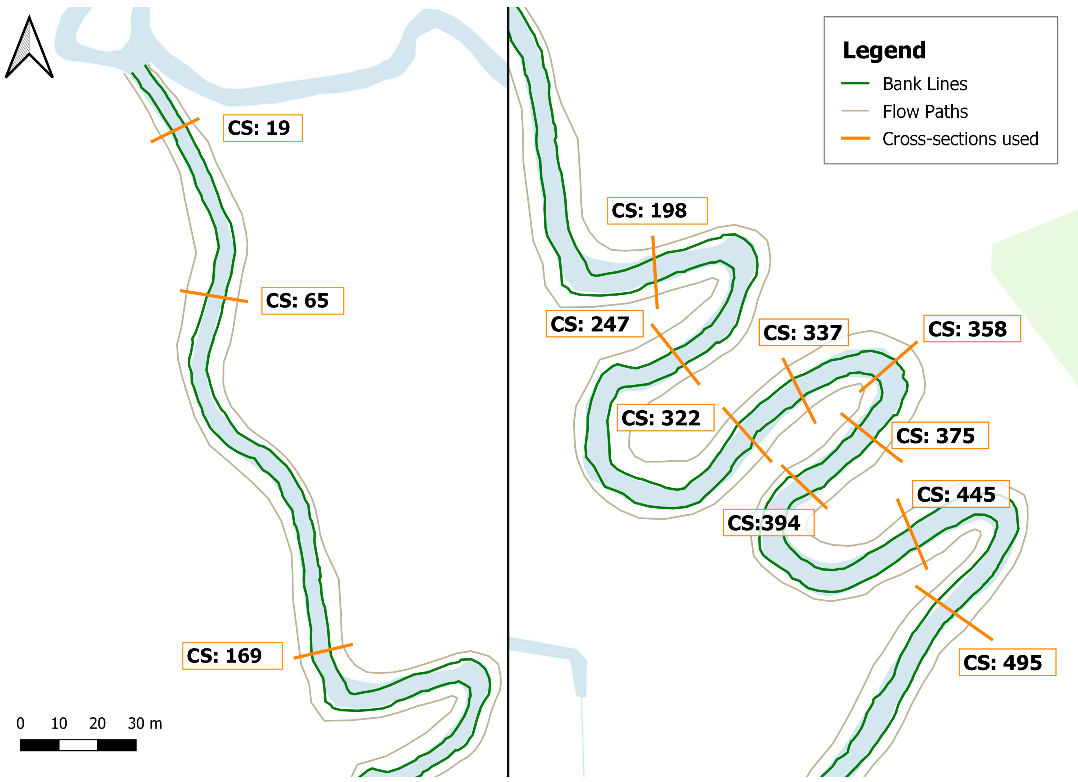

Figure 6.13. Cross-sections included in Manning's and NCALC calculations under high flow.

The analysis was focused primarily on the meander area because more cross-sectional data was available for this part. For Manning's equation, an average value of flow, area and hydraulic radius from all the cross-sections included in the estimation were used, while for the NCALC method, the cross-sections were included as described in Equation 6.4.

Regardless of flow condition, similar behaviour was observed in the meander area. As illustrated in Figure 6.14, larger variability in n was observed with a lower number of cross-sections. As the number of cross-sections included in the calculations increased, the n value tended to approach a constant value, both for Manning's and NCALC methods.

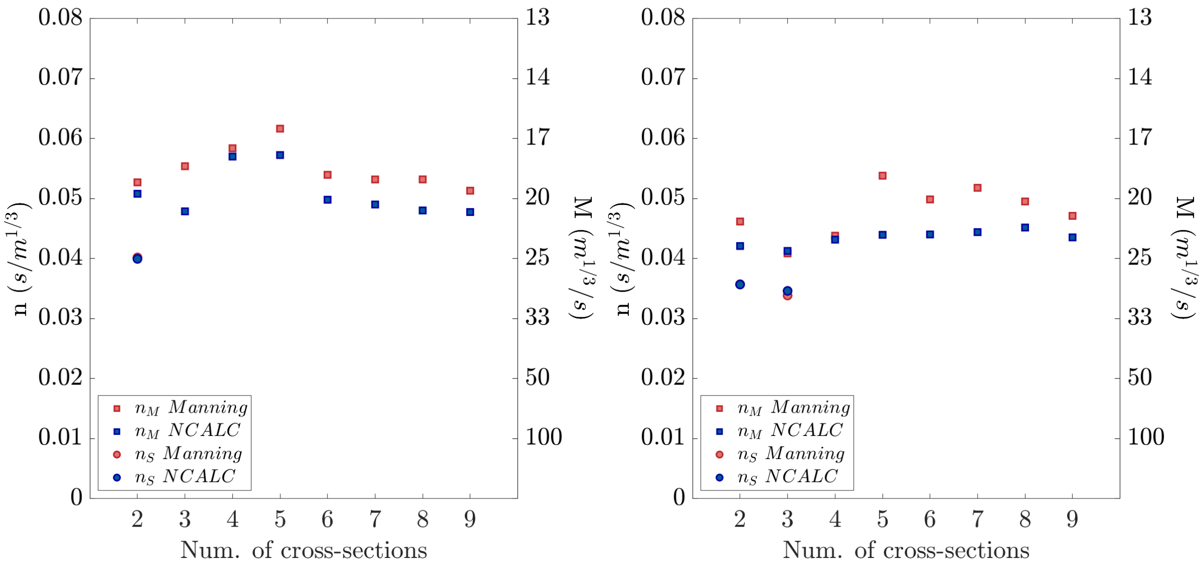

(a) Low Flow

(b) High flow

Figure 6.14. Variation of roughness coefficient values (n) with the change in the number of cross-sections used for the calculations for (a) low flow; and (b) high flow conditions.

The difference in estimated roughness coefficients between the utilised methods can lead to significant over or underestimation of the water level in small-size streams such as Binderup Å [Kim et al., 2010], which is problematic when dealing with flood risk assessment.

The average difference in the roughness coefficient calculated by the three different methods was approximately 10%. Therefore, the effect of a 10% increase in the n on calculated water depth at both meander and straight sections of Binderup Å was analyzed using HEC-RAS, for the two different discharge conditions.

The maximum and mean difference, along with the percentage change from the original conditions, are shown in Figure 6.15. A 10% increase in roughness coefficient led to an average of 4% and 5% rise in water depth for meandering and straight sections, respectively. At certain cross-sections, however, increases of 5% to 6% were observed. The difference between the average value of the entire area and the maximum value is larger for the meandering.

Even though the percentage changes in water level were almost the same for the two flows, the absolute difference in water level tended to diminish with decreasing discharge. The maximum observed increase was around 0.05 m. Besides this, the disparity between the average difference and maximum difference was lower in the straight section than in the meandering.

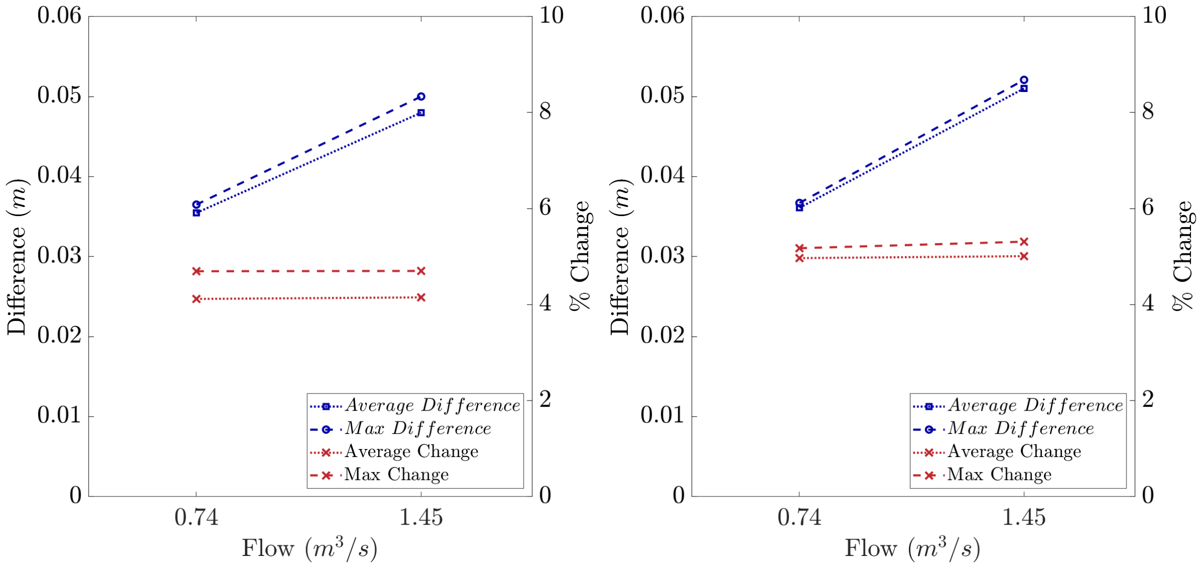

(a) Meandering Reach *(b)* Straight Reach

Figure 6.15. Change in water surface elevation for low and high discharges at the (a) meandering; and (b) straight reaches of Binderup Å when the roughness coefficient in the HEC-RAS is increased by 10%.

6.4 Uncertainty of flow measurements on roughness coefficient estimation

The estimation of the n based on measured flow data included the uncertainty originating from the flow measurements. Therefore, it was necessary to find a way to estimate how the error in ADCP measurements may affect the roughness coefficient calculations.

In order to assess any propagation of the error stemming from the ADCP measurements, a Monte Carlo Simulation was performed considering the uncertainty range of the measured discharges of 0.74 and 1.45 m^3/s. Firstly, the normal probability distribution of the discharge measurements was proven by a Lilliefors test. Following this, one data set of 100,000 values for each flow condition was generated, assuming a normal distribution. Then, for each of the generated flow values, the roughness coefficient using the NCALC method and Manning's equation were calculated. In these calculations, the previously estimated values were used to get the remaining terms of the methods.

6.4.1 Probability distribution of ADCP discharge measurements

The frequency distribution of the studied variable needed to be known before carrying out the Monte Carlo simulations. In this case, the Lilliefors test was used to evaluate whether a dataset is normally distributed. The Lilliefors test evaluates the absolute value of the maximum vertical deviation between the normal distribution and the empirical distribution of the data set. This value is compared with a threshold value that depends on the number of observations and selected significance level. If the calculated value is smaller than the threshold the data can be normally distributed for the selected significance level [Poulsen, 2005].

In this case, the flow measurements taken at each transect were the studied variable, including 80 measurements under low-flow conditions, and 36 under high-flow conditions. The empirical and normal cumulative distribution function for both data sets is displayed in Figure 6.16. Visual inspection of the graphs suggested that the data may be normally distributed.

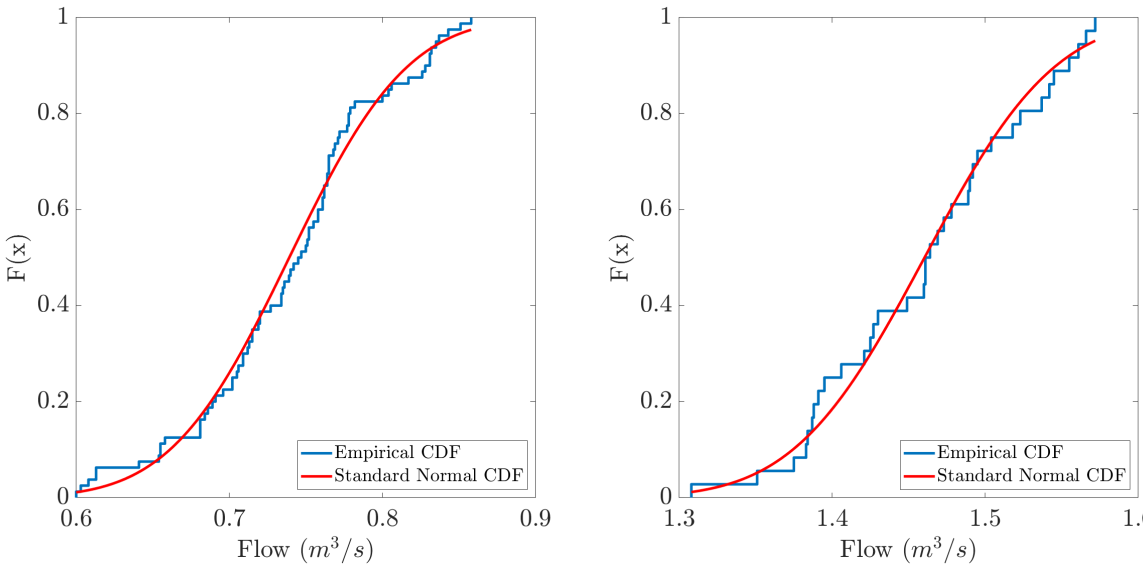

(a) Low Flow Conditions

(b) High Flow Conditions

Figure 6.16. Empirical and Normal Cumulative Distribution Function of (a) low flow; and (b) high flow conditions, made from the measurements taken at Binderup Å.

The results of the Lilliefors test confirm the normal distribution of the data. In both low and high discharge cases, the Lilliefors threshold value for the data set was observed to be greater than the maximum absolute difference between the empirical and normal cumulative distribution function (Max $T_{(i)}$), as presented in Table 6.1.

Table 6.1. Lilliefors test results for the two used data sets. Max $T_{(i)}$ represents the maximum absolute difference between the empirical and normal distribution. σ is standard deviation.

Mean Discharge $[m^3/s]$	**Min. Disch.** $[m^3/s]$	**Max. Disch.** $[m^3/s]$	σ $[m^3/s]$	**Max T$_{(i)}$**	**Lilliefors Threshold**
0.74	0.6	0.86	0.04	0.069	0.100
1.45	1.31	1.57	0.07	0.085	0.149

6.4.2 Monte Carlo Simulation of roughness coefficient

As the two data sets were proven to be normally distributed, 100,000 random flow values could be generated for each discharge condition based on their distribution function.

Following this, for each of the generated flows two roughness coefficient values were calculated for the meandering and the straight portions, one based on the NCACL method and the other on Manning's equation.

The generated roughness coefficients by the Monte Carlo Simulation were normally distributed, based on their frequency distribution plots as shown in Figure 6.17. For both flow conditions, the values estimated with Manning's equation were consistently higher than the NCALC, and the difference between straight and meandering was also more significant.

In general, roughness obtained with the NCALC method displayed a lower standard deviation than the one from Manning's equation for the same flow conditions, as seen in Table 6.2. Moreover, the standard deviation was decreased when the flow conditions increased.

Table 6.2. Mean (μ) and standard deviation (σ) of the roughness coefficient calculated by Monte Carlo Simulation, for the different flow (Q) and roughness methods. Values in brackets correspond to M.

Q	**n Method**	$\boldsymbol{\mu_{n_S}}$	$\boldsymbol{\sigma_{n_S}}$	$\boldsymbol{\mu_{n_M}}$	$\boldsymbol{\sigma_{n_M}}$
Low	NCALC	0.040 (25)	0.0034	0.048 (21)	0.0040
Low	Manning	0.041 (24)	0.0034	0.052 (19)	0.0043
High	NCALC	0.034 (29)	0.0016	0.043 (23)	0.0020
High	Manning	0.034 (29)	0.0016	0.047 (21)	0.0022

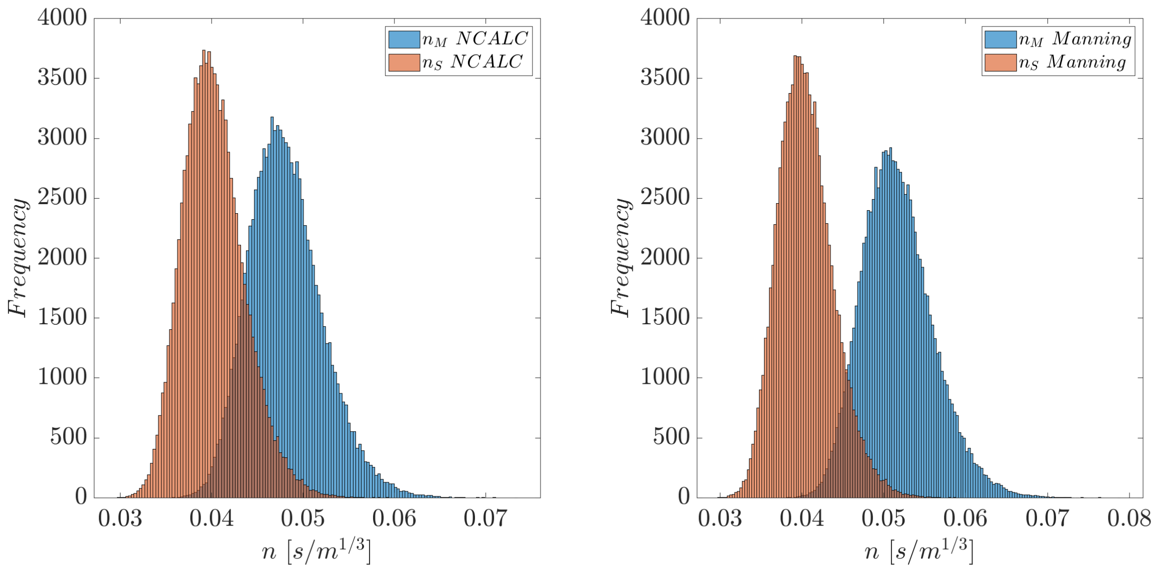

(a) Low-flow and NCALC method ***(b)*** Low-flow and Manning's eq.

Figure 6.17. Estimated roughness coefficient n via Monte Carlo Simulation for different conditions and methods. (a) Low-flow conditions and NCALC method; (b) Low-flow conditions and Manning's equation; (c) High-flow conditions and NCALC method; (d) High-flow conditions and Manning's equation.

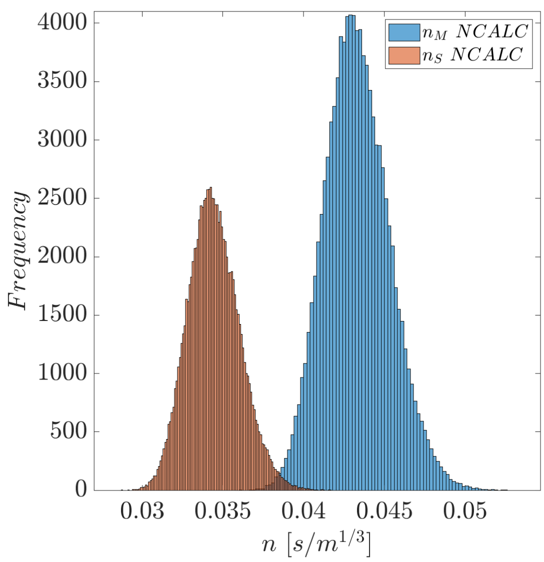

(c) High-flow and NCALC method

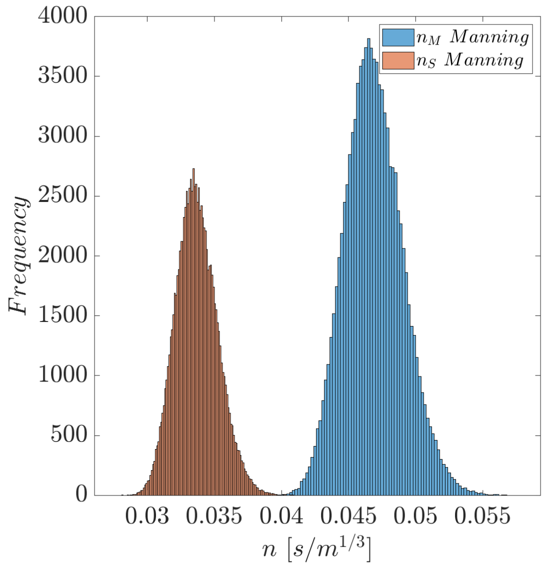

(d) High-flow and Manning's eq.

Figure 6.17. ***(cont.)*** Estimated roughness coefficient n via Monte Carlo Simulation for different conditions and methods. (a) Low-flow conditions and NCALC method; (b) Low-flow conditions and Manning's equation; (c) High-flow conditions and NCALC method; (d) High-flow conditions and Manning's equation.

When comparing the original n values with those obtained at two tails 95% confidence interval from the Monte Carlo Simulation, larger uncertainty was observed under low flow conditions despite the used method and section of the stream. Meanwhile, the uncertainty due to error in ADCP flow measurements was reduced as flow increased, as seen in Table 6.3.

Table 6.3. Uncertainties associated with the values of the Manning coefficient due to errors of ADCP flow measurements. Values in brackets correspond to M.

Q	**n Method**	$\mathbf{n_{S(orig.)}}$ $[s/m^{1/3}]$	$\mathbf{n_{M(orig.)}}$ $[s/m^{1/3}]$	**Uncertainties of $\mathbf{n_S}$ [%]**			**Uncertainties of $\mathbf{n_M}$ [%]**		
				$\mu-2\sigma$	μ	$\mu+2\sigma$	$\mu-2\sigma$	μ	$\mu+2\sigma$
Low	NCALC	0.040 (25)	0.048 (21)	16.2	0.78	17.5	16.2	0.81	17.39
Low	Manning	0.040 (25)	0.051 (20)	16.2	0.78	17.5	16.2	0.78	17.39
High	NCALC	0.035 (29)	0.044 (23)	9.73	0.50	8.73	9.73	0.50	8.73
High	Manning	0.034 (29)	0.047 (21)	9.73	0.50	8.73	9.73	0.50	8.73

6.5 Discussion of hydraulic properties

The 1-D model generated in HEC-RAS proved to be an accurate yet simple and fast tool for replicating the water levels observed in Binderup Å. The inbuilt functions of the program allow the generation of the geometry of the studied system in different ways, depending on the available data. In this project, the process of merging the ADCP bathymetry with the topographical map directly in HEC-RAS had the advantage of generating a unique terrain that contained both bathymetry and terrain data, while being possible to generate the model geometry directly from this. In case of needing additional cross-sections to describe certain areas of the stream, they could be easily added as elevation data was available for the whole study area.

The model accuracy was based on the roughness coefficient of the meandering (n_M) and straight (n_S) areas. In sub-critical flow, the wave celerity is higher than the stream velocity, meaning that backwater effects are observed [Brorsen and Larsen, 2009]. This suggests that if a manual procedure of calibration is used, then n values should be modified from the down- to upstream direction.

The model also showed an acceptable representation of the water level under both low and high flow conditions. However, as it was proven, the roughness coefficient is dependent on the flow conditions, being inversely correlated for the case of Binderup Å. A better representation of the real-world conditions might be obtained with the implementation of a variable roughness coefficient. This might be more important in the case of unsteady simulation to correctly predict the water level of an event.

As for the hydraulic properties, the meandering part of the stream generally showed a larger cross-sectional area and wetted perimeter. This may be explained by the particular velocity distribution in the meandering area that generates sediment transport with erosion and deposition processes. Resistance in this area was also higher for all flow conditions.

The bank geometry in straight cross-sections typically followed a more vertical path than meanders until reaching terrain, which occurred at 1.21 m^3/s. At this point, the horizontal terrain caused the wetted perimeter to increase at a high rate. The banks around meanders, on the other hand, were typically higher than in the straights, particularly on the inner bank, meaning the slope continued at a more gradual gradient for longer in meanders, resulting in a more gradual increase in wetted perimeter than in the straight sections,

Meanders could contribute to an increase in n of up to 39% or a minimum of 20% according to the Manning and NCALC methods respectively, across both flow conditions. The HEC-RAS method returned values within the range of these two methods. This equates to a reduction of conveyance of up to 28 m^3/sec, which indicates that if straight sections were to be altered to meanders of the same curvature as studied in this project, the risk of flooding could be significantly increased.

The difference between the two sections was larger under high-flow conditions, which might be due to the rapid decrease in hydraulic radius at the straight portion and the larger difference in cross-sectional area. This means that even though the resistance was reduced with higher flow, the observed reduction was smaller than in the straight section.

In the straight portion, Manning's and NCALC methods used to estimate n showed similar results. This could be the result of the almost constant cross-sectional geometry throughout the straight section. In this scenario, the averaged cross-sectional area and hydraulic radius used in Manning's equation were almost the same as one of the individual cross-sections. Therefore, expansion and contraction effects become largely insignificant. Conversely, the opposite effect occurred in the meandering channel. Significant changes in cross-sectional geometry took place in the different bends, which cannot be incorporated in Manning's equation as averaged values for the whole reach were used. The NCALC method on the other hand does incorporate the effects of contraction or expansion between each cross-section throughout the reach. Values of n obtained with HEC-RAS were similar to those calculated with the other methods for low flow conditions and were higher than those obtained with other methods for high flow.

When a higher number of cross-sections were included in the n estimation with Manning's and NCALC methods, a lower variability in results were obtained. This may be a result of considering a larger length where a more general representation of the resistance in the reach is possible to be obtained.

The uncertainty in flow measurements had a considerable impact on roughness estimation. Even though the ADCP proved to be a reliable method to measure discharge, see Chapter 5, the error of the method influences the estimation of n values. At low flow conditions, the error in flow measurements resulted in larger uncertainties.

In general, an increase of 10% in n values led to an increase of around 5% in water level in both the meandering and straight sections. Under low flow conditions, the increase in n due to uncertainty in flow measurements was almost double that seen at high flow. This means that at high-flow conditions, a 5% difference in water level could be expected, or even higher at low-flow conditions. This implies that the estimated roughness coefficient for low flow was more affected than that for high flow by the same degree of uncertainty in flow measurement. Depending on the application, it might be necessary to analyze whether the estimated uncertainty is acceptable for different flow conditions or if efforts need to be made to increase the quality of the discharge measurements.

In addition, the uncertainty in the water level measurements taken using the differential GPS, which has a vertical uncertainty of between 2-3 cm, could prove to have some impact on these results. However, they have not been accounted for in this study. On top of that, the method of inserting a stake into the stream bed, placing the GPS on top of this stake, and subsequently subtracting the height of the stake above the water surface from the GPS-measured elevation could introduce some added level of uncertainty. Moreover, to reduce the uncertainty in the calculations, equally spaced and larger number of water level measurements should be taken. This would provide a better representation of how the water surface slope changes along the stream. In addition, to ensure a better comparison between low and high flow conditions, both water level and cross-sectional data could be taken exactly at the same position for the different conditions.

It is important to note that as Manning's equation is based on empirical data of straight, uniform channels at steady state, every variation away from these conditions makes this equation less reliable for estimating n. NCALC addresses the expansion and contraction factors along the reach, but there is still a multitude of factors that remain unaccounted for. Therefore, some deviation from the true value of n should be expected, regardless of the method.

The largest differences between methods were typically seen under high flow conditions.

This could be attributed to the less uniform flow conditions when these data were obtained, which could lie outside the recommended scope of the selected methods.

6.6 Conclusion of hydraulic properties

From the analysis made through this Chapter on 1-D modelling and roughness coefficient, it could be possible to conclude that:

- The applicability and accuracy of the 1-D model generated in HEC-RAS for replicating water levels in Binderup Å under different flow conditions have been demonstrated. The merging of ADCP bathymetry with topographical data in HEC-RAS was found to be advantageous as it generated a unique terrain that contained both bathymetry and terrain data. The model's accuracy was based on the roughness coefficient of the meandering and straight areas, which was inversely correlated with flow conditions. The model was more sensitive to downstream n values, as expected for sub-critical flow conditions.
- Differences in the roughness coefficient calculated with the different methods were larger in the meandering section due to the variations in cross-sectional geometry. Conversely, the three methods returned similar roughness values in the straight section. The findings in this chapter demonstrate that up to 39% of the resistance to flow could be attributed to the meanders in Binderup Å. However, the uncertainty in flow measurements had a significant impact on n estimation, particularly under low-flow conditions.
- Overall, the study suggests the need for a dynamic roughness coefficient that better reflects real-world circumstances in terms of spatial distribution and flow conditions. Efforts must be made to increase the quality of discharge measurements and analyze if the estimated uncertainty is acceptable for different flow conditions, depending on the application. Additionally, the method selection for calculating n should be considered, as each is more appropriate for certain stream conditions than the other. Specifically, the NCALC is more appropriate for more complexly shaped streams, while the regular Manning's equation requires more assumptions to be made, but saves time as a result.
- Conclusions on the accuracy of the n calculations cannot be made. Therefore, uncertainty has to be expected in the n value and be considered during the application instead of relying on a single value.

Evaluation of Hydraulic Properties in 3-D Model 7

The computational fluid dynamics (CFD) software STAR-CCM+ was used to model the hydrodynamic conditions in a series of simple open channels with varying degrees of curvature. The aim of this was to isolate the effect of the bend itself on n, and remove the effects of irregularities in channel shape and roughness. The following chapter will describe the methods used to set up the model, validate it, and finally extract a result that can be related to the theory.

7.1 3-D hydrodynamic model presentation

Three models were constructed to assess the effect of curvature on n, with curvatures of C=0, corresponding to the straight section of Binderup Å, C=0.63, corresponding to the second meander at Binderup Å, and C=0.31, serving as an intermediate, as illustrated in Figure 7.1. The geometric design of the models was modified to adopt a simplified rectangular channel with a uniform flat bottom. Consequently, a specific segment of the channel measuring 3.90 meters in length and 1 meter in width was selected for the analysis, maintaining a total height of 0.55 meters. Data acquisition was performed at nine equally spaced planes within this segment, identified as P1-9 and visually represented in Figure 7.1.

A straight 2.5-meter extension was added at the outlet of the models to eliminate any backwater influence the boundary condition may have on the planes used for data extraction. Similarly, a 5-meter extension was added to the inlet sections to ensure uniform conditions preceding the area of analysis.

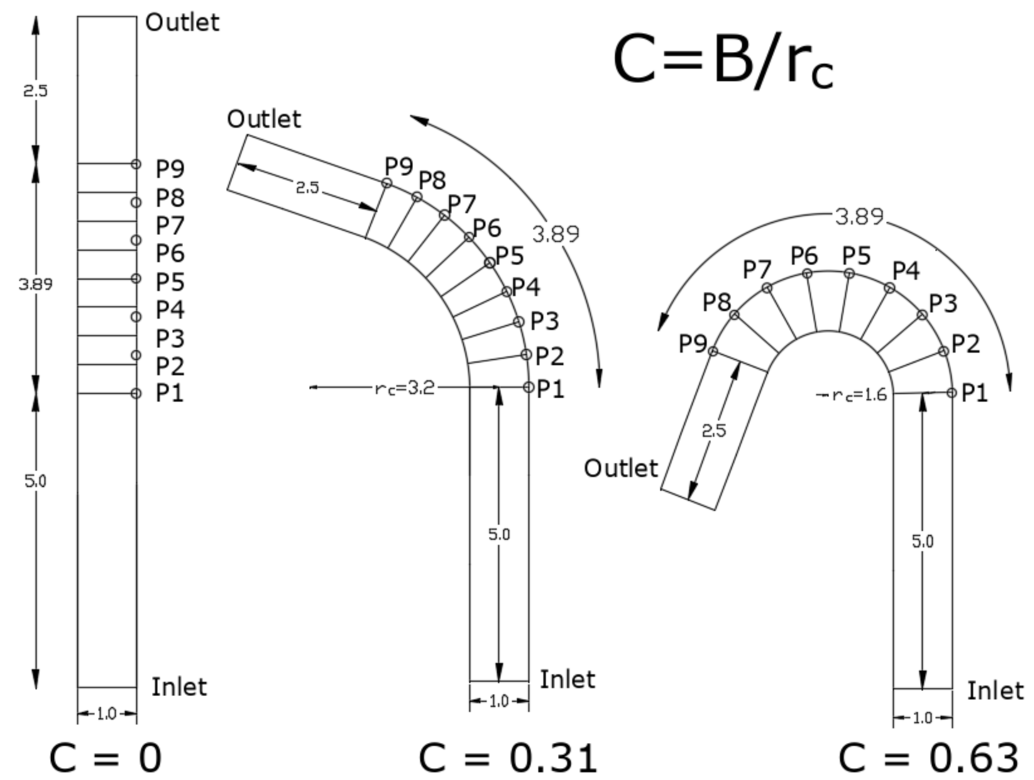

Figure 7.1. Geometries used in Star CCM+ with curvatures of C=0(On the left), C=0.31, and C=0.63. C is the curvature of the channel, B is the width and r_c is the radius of curvature.

7.1.1 Physics selection

The selected physics models define the components of the model, interactions between elements of the model, and the type of flow. The selection, therefore, needs to be carefully tailored to suit the input and desired outcome of the model.

In this case, the flow was expected to be turbulent, with pressure losses and variation in water elevation being essential outcomes of the model. The Reynolds-Averaged Navier Stokes (RANS) model was selected as the overarching turbulence model as it provides a balance between accuracy and computational efficiency by averaging the Navier-Stokes equations over time. The specific RANS model selected was the Realizable K-Epsilon Two-Layer model, which enforces the standard K-Epsilon model in the turbulence-dominated region far from the wall, where the equations for kinetic energy transport and dissipation are described. In the boundary layer, however, the model employs an 'all y+ wall' treatment, which combines two methods to address varying y+ values in the model. The first is the high y+ wall treatment; employed in areas where the near-wall mesh resolution is relatively low, it assumes the impact of the viscous layer is negligible and applies the logarithmic 'law of the wall' to estimate the velocity profile. The second method is the low y+ wall treatment, where the mesh is of a resolution sufficient to resolve the viscous sublayer via a set of closure equations specifically designed for the near-wall flows.

Additionally, the two-phase multiphase model and the Volume Of Fluid (VOF) Waves model were included to account for the effects of a varying transverse water level. The two-phase multiphase model is used to simulate the interaction between two fluids, in this case, air and water, by tracking the volume fractions of each fluid and solving the conservation equations for each phase separately. The VOF Waves model is another multiphase model used to track the interface between the air and water phases, particularly to simulate the waves on the water's surface. The VOF-generated waves allow the effects of waves and ripples to be included in the simulation, moving the model closer to real-world conditions. Finally, the Implicit Unsteady solver was selected, as it is useful for solving unsteady flow equations where the properties change with time. The remaining models used in this study can be found in Appendix F.

7.1.2 Mesh discretization

The discretization of the computational domain into a grid of elements is commonly known as meshing. The size of the mesh elements determines the resolution of the numerical solution. A finer mesh with smaller elements leads to a more accurate solution approximation. However, a finer mesh also requires more computational time and may lead to numerical instabilities if the time step is not appropriately selected.

In this study, the model domain was specifically designed with a height of 0.55 meters and a width of 1 meter, as depicted in Figure 7.2. The base mesh resolution was set to 0.05 meters, with a flexible range of +/-20% around this value.

In order to enhance the accuracy of capturing boundary layers and the physics of near-wall flow, a 5-centimetre prism layer was introduced in the vicinity of the walls. This prism layer was implemented to effectively represent the flow characteristics in close proximity to both the stream bed and the banks. The distance from the wall to the nearest cell was 1.28 millimetres, ensuring a refined resolution in the near-wall regions.

The Flat Wave model utilized in this study allowed for specifying the initial Point On Water Level, in this case set to the arbitrary value of 0.4 meters. As illustrated in Figure 7.2, a region of high mesh-resolution extending between the minimum and maximum water surface elevation in the area of analysis was implemented to more accurately measure the conditions around the interface.

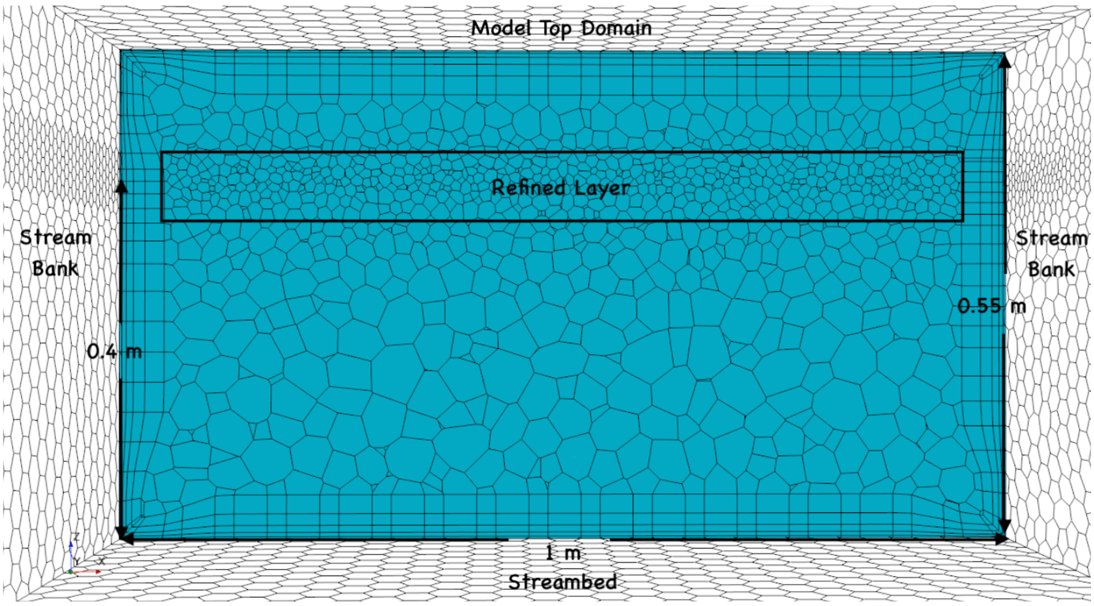

Figure 7.2. Mesh structure of the vertical plane.

The wall y+ value is a parameter used to describe near-wall mesh resolution and the ratio of viscous to turbulent forces. It is given by Equation 7.1, where u_f is the friction velocity, y is the absolute distance of the cell centroid from the wall, and ν is the kinematic viscosity.

$$y+ = \frac{y * u_f}{\nu} \tag{7.1}$$

The Realizable K-Epsilon Two Layer turbulence model has an optimal y+ range, with the high y+ method optimised for y+ values larger than 30 and the low y+ method optimised for y+ below 5. This means that the optimal y+ range is y+ $<$ 5 and 30 $<$ y+ $<$ 60 [Salim and Cheah, 2009].

7.1.3 Boundary selection

To replicate turbulence levels measured in Biderup Å in the 3-D model, the average velocity at the inlet boundary had to be scaled. This involved utilizing the Reynolds Number (Equation 7.2) which quantifies the ratio between inertial forces and viscous forces within the fluid flow, thereby characterizing the level of turbulence. The average wetted perimeter, cross-sectional area, and velocity were extracted from ADCP measurements. Subsequently, the hydraulic radius R was computed using Equation 7.3.

$$Re = \frac{\rho * v * R}{\mu} \tag{7.2}$$

$$R = \frac{A}{P} \tag{7.3}$$

ρ	Fluid density $[kg/m^3]$
v	Velocity magnitude $[m/s]$
R	Characteristic linear dimension (Hydraulic Radius) $[m]$
μ	Dynamic viscosity of the fluid $[Pa \cdot s]$
A	Area
P	Wetted Perimeter

To find the velocity required in the down-scaled model, Equation 7.3 was first used to find the R of the down scaled geometry. This R was then substituted into Equation 7.2, along with the previously found Re. Finally, the scaled velocity was estimated and the results of R and v can be found in Table 7.1 along with the Reynolds number calculated by using the ADCP measurements.

Table 7.1. Reynolds number scaling results and comparison with ADCP measurements

Meas. Vel. [m/s]	**Meas. R [m]**	**Scaled R [m]**	**Re [-]**	**Scaled Vel. [m/s]**
0.3141	0.48	0.22	171139.85	0.6804

The downstream boundary was set to a pressure outlet utilizing the hydrostatic field function. Specifically, the Hydrostatic Pressure of Heavy Fluid of Flat VOF Wave, which is a VOF Waves model built-in field function suitable for the outlet pressure boundary [Siemens, 2022]. This function calculates the hydrostatic pressure in the heavy fluid based on the distance from the Point On Water Level.

The models 'Top' boundary illustrated in Figure 7.2 was characterized as a slip boundary, which allows free movement across the domain. The streambed and banks were defined as no-slip boundaries, enforcing a zero velocity gradient at the interface between the surface and fluid phases. Shear stress specifications were applied to these boundaries to simulate the frictional resistance experienced by the fluid as it interacts with these surfaces. In addition, the rough method was chosen for wall surface specifications, which allows for the specification of a sand-grain roughness height parameter. Due to the y+ wall limitation discussed in Section 7.1.2, as well as to further simplify the model, this roughness value was set to 0.

7.1.4 Assessment of steady-state conditions and examination of upper and lower boundary effects

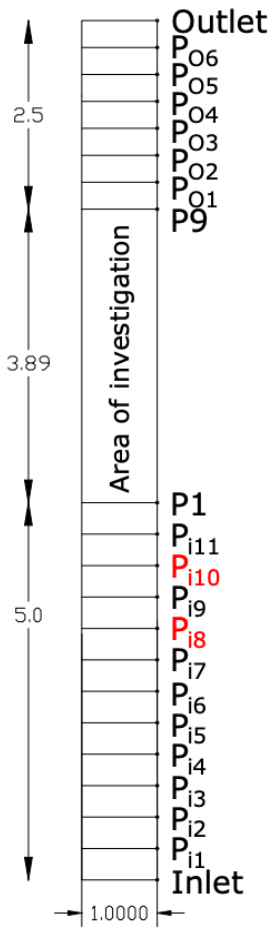

Figure 7.3. Location of planes used for checking steady state condition in in- and outlet channels

To assess whether the conditions between the boundaries and the area of analysis reached a steady state and were free of influence from the boundaries, the changes in velocity and surface elevation between the inlet and P1 as well as between P9 and the outlet, were analysed.

In each model, a series of 11 equally spaced planes were placed between the inlet and P1, with 6 equally spaced planes placed between P9 and the outlet plane, as illustrated in Figure 7.3. While this illustration represents model C=0 specifically, it also represents the location of these planes in models C=0.31 and C=0.63 sans the bent area of analysis.

Velocity data from these were assessed to determine whether the velocity profiles were fully developed between the inlet and P1, while surface elevation data was used to determine whether the fixed water elevation at the outlet had an impact on the conditions at P9.

Figures 7.4a and 7.4b show the velocity profiles in planes P_{i8} and P_{i10} in the C=0.63 models. These profiles are visually similar, indicating similar flow conditions, with a developed velocity profile along the stream bed and banks.

The full collection of profiles for each model can be found in Appendix F, where the profiles between P_{i1} and P_{i7} can be seen developing along the walls. In models C = 0.31 and C = 0.63, the development of the higher velocity region towards the inner bank can also be seen developing from P_{i9} to P_{i11}.

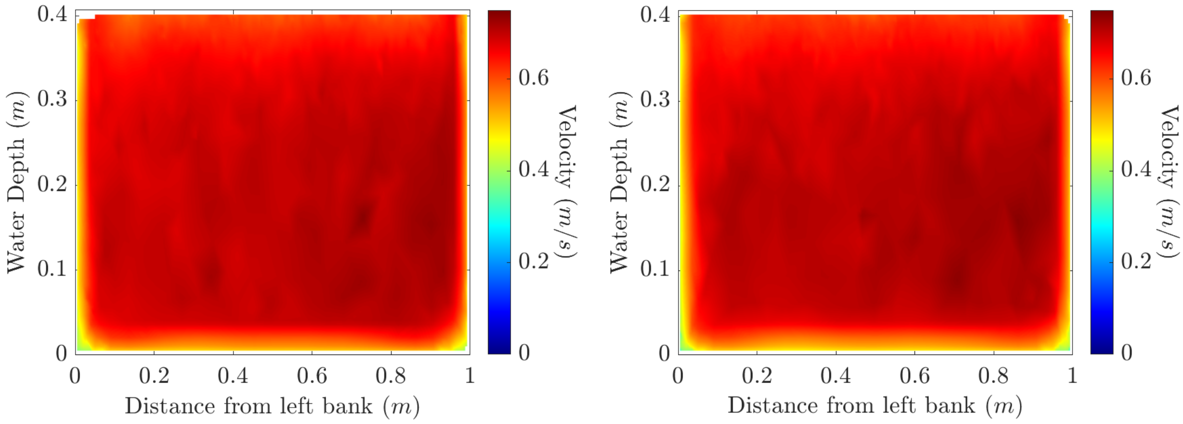

(a) Velocity Profile, P_i8, C=0.63. *(b)* Velocity Profile, P_{i10}, C=0.63.

Figure 7.4. Velocity profiles in P_i8 and P_i10 in the C=0.63 model.

The Mean Square Error (MSE) of streamwise velocity between adjacent planes was found, representing the overall change in velocities between planes. The MSE between planes in the inlet channel followed the same trend in all three models, with the MSE remaining below 1.9x10^{-4} between the first three planes, before increasing sharply to between 2.6x10^{-3} and 3.1x10^{-3} between planes P_{i3} and P_{i4}, as shown in Figure 7.5. Following this, the MSE in all three models dropped to approximately 8.5x10^{-5} by P_{i10}.

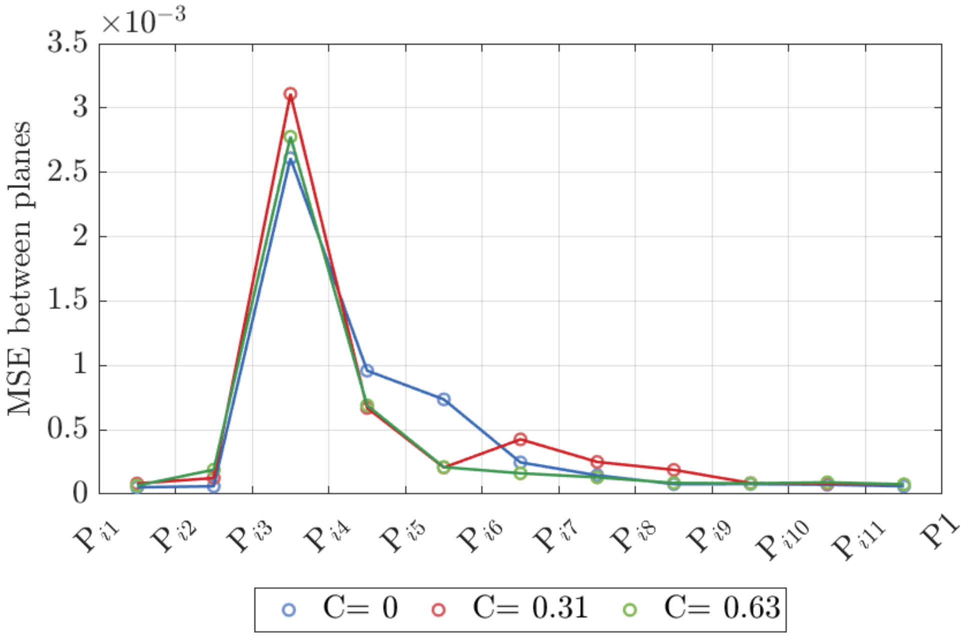

Figure 7.5. MSE between adjacent planes in the inlet channel in all three models.

In the outlet channel, the MSE tended to start relatively high in models C=0.63 and C=0.31 between planes P9 and P_{O1}, at 2.8x10^{-3} and 8.2x10^{-4} respectively. Towards the outlet, this value dropped towards the MSE in the C=0 model, at approximately 5.3x10^{-5}.

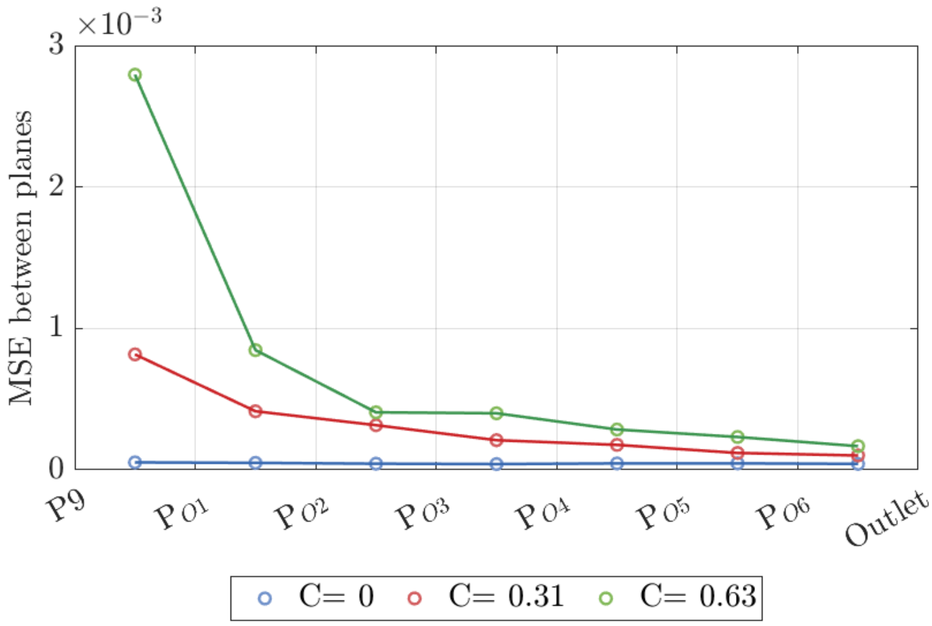

Figure 7.6. MSE between adjacent planes in the outlet channel in all three models.

Additionally, the slope of the water surface elevation was analysed along the centerline of the inlet, where it was found that the surface fluctuated greatly in the first 1 to 2 meters in each of the models, before reaching a state of relative steadiness towards P1. An example of this can be seen in Figure 7.7, showing the water elevation between the inlet and P1 in model C=0, with all three slopes shown in Appendix F.

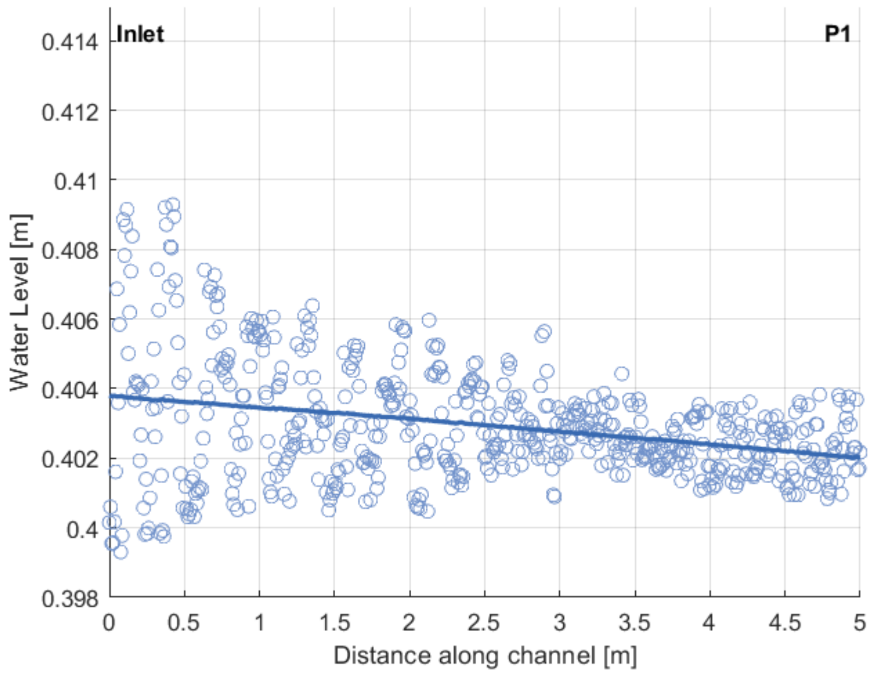

Figure 7.7. Water surface elevation along the center line of inlet channel in model C=0.

Finally, the transverse slope of the water surface at each plane was compared along the outlet channel to identify whether the lower boundaries fixed elevation had an impact on the analysis area. Figure 7.8 shows that the slope in models C=0.63 and C=0.31 had a relatively high transverse slope at P9, with 0.017 m/m and 0.008 m/m, respectively, before dropping to below 6.45x10^{-4} m/m by P_{O4}. Model C=0 maintained a relatively low slope throughout.

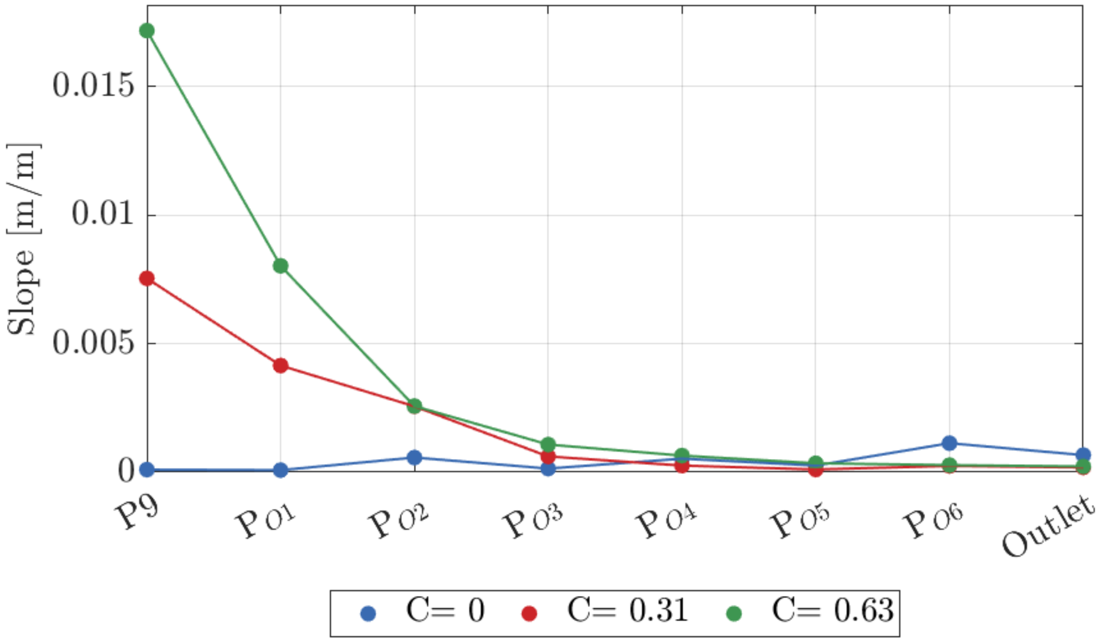

Figure 7.8. Transverse slope of water surface along outlet channel.

7.1.5 Sensitivity analysis

The sensitivity of the C=0 model to certain design parameters was analysed, specifically to changes in Time Step (TS) and Mesh Base Size (MBS). The analysis was partitioned into two segments. The first focused on variations in the MBS by evaluating values of 0.045, 0.050, and 0.055 meters while maintaining a constant TS of 0.1 seconds. The second segment of the analysis examined variations in the TS with values of 0.005, 0.01, 0,02, 0.05 and 0.1 seconds while keeping the MBS fixed at 0.05 meters. Subsequently, the resulting output of n from these modified simulations was compared to the corresponding median of the Courant number, as illustrated in Table 7.2.

Table 7.2. Used scenarios for sensitivity analysis with median, quartiles 25 and 75 of the Courant Number.

Time Step [s]	**Mesh Base Size** [m]	**Median Courant Number**	**Interquartile Courant Num.**
0.005	0.05	0.18	0.10 - 0.32
0.01	0.05	0.37	0.20 - 0.65
0.02	0.05	0.79	0.41 - 1.31
0.05	0.05	2.26	1.21 - 3.63
0.1	0.05	4.2	2.76 - 5.64
0.1	0.055	3.71	2.45 - 5.18
0.1	0.045	4.47	2.95 - 6.26

The model that would be used for the final results was decided on by taking the model with the lowest computational time while still returning results similar to that of the TS 0.005 seconds model, which had the lowest median Courant number and was therefore assumed to have the most accurate result.

Figure 7.9 shows the n values calculated in each model, with models TS of 0.02 seconds, 0.01 seconds as well as the MBS of 0.045 meters performing similarly to the TS of 0.005 seconds, all returning n values of approximately 0.01 $s/m^{1/3}$ (M = 100).

The simulation with a TS of 0.05 seconds reveals that despite the median Courant number being more than twice the recommended value, the resulting n value of approximately 0.011 $s/m^{1/3}$ (M = 91) was approximately 10% higher than in the TS 0.005 seconds model. The simulation with the lowest n value observed was the TS of 0.1 seconds, where the median Courant number was 4.2 and n was 0.005 $s/m^{1/3}$ (M = 200).

The highest n value was recorded in the simulation with an adjusted MBS of 0.055m. This 10% increase of MBS lead to an almost twofold increase in n while maintaining a Courant number of 3.71.

This influence was observed as the larger cell sizes led to overestimating water surface elevation, whereas smaller mesh sizes yielded similar outcomes to simulations conducted with TS of 0.02, 0.01, and 0.005 seconds with designated MBS of 0.05 meters. Therefore, the emphasis was placed on selecting the most appropriate TS for subsequent analysis while maintaining the MBS at 0.05 meters.

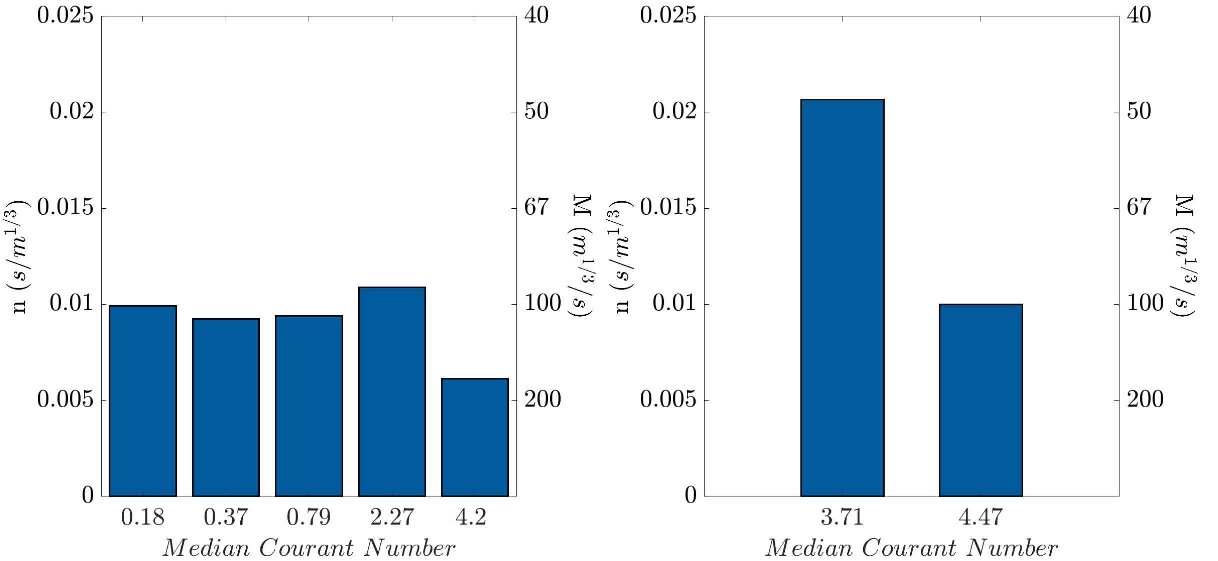

(a) Variation in Time Step ***(b)*** Variation in Mesh Base Size

Figure 7.9. Comparison of calculated n between different models with changed (a) Time Step, and (b) Mesh Base Size.

Furthermore, a thorough analysis was conducted to evaluate the sensitivity of various parameters used to estimate the n value. These parameters include the cross-sectional area (A), hydraulic radius (R), water surface elevation at the centre line, and velocity head (h_v) between planes P1 and P9, as shown in Figure 7.10.

The assessment of the results revealed that most of the TS's performed similarly, with the exception of TS of 0.1 seconds, which led to an overestimation of the values of A, R, and h compared to other TS scenarios. Notably, the h_v parameter demonstrated slightly higher values at Plane 9 in all simulations, except for the simulation with a TS 0.1 seconds. In this particular case, the h_v values at P1 and P9 were equal.

Based on these findings, it was evident that simulations with TS of 0.02, 0.01, and 0.005 seconds performed similarly. Therefore, a decision was made to select the time step configuration that yields the best performance while also minimizing computational resource requirements. Consequently, the chosen combination for further analysis was a time step of 0.02 seconds and a Manning's roughness coefficient MBS of 0.05 meters.

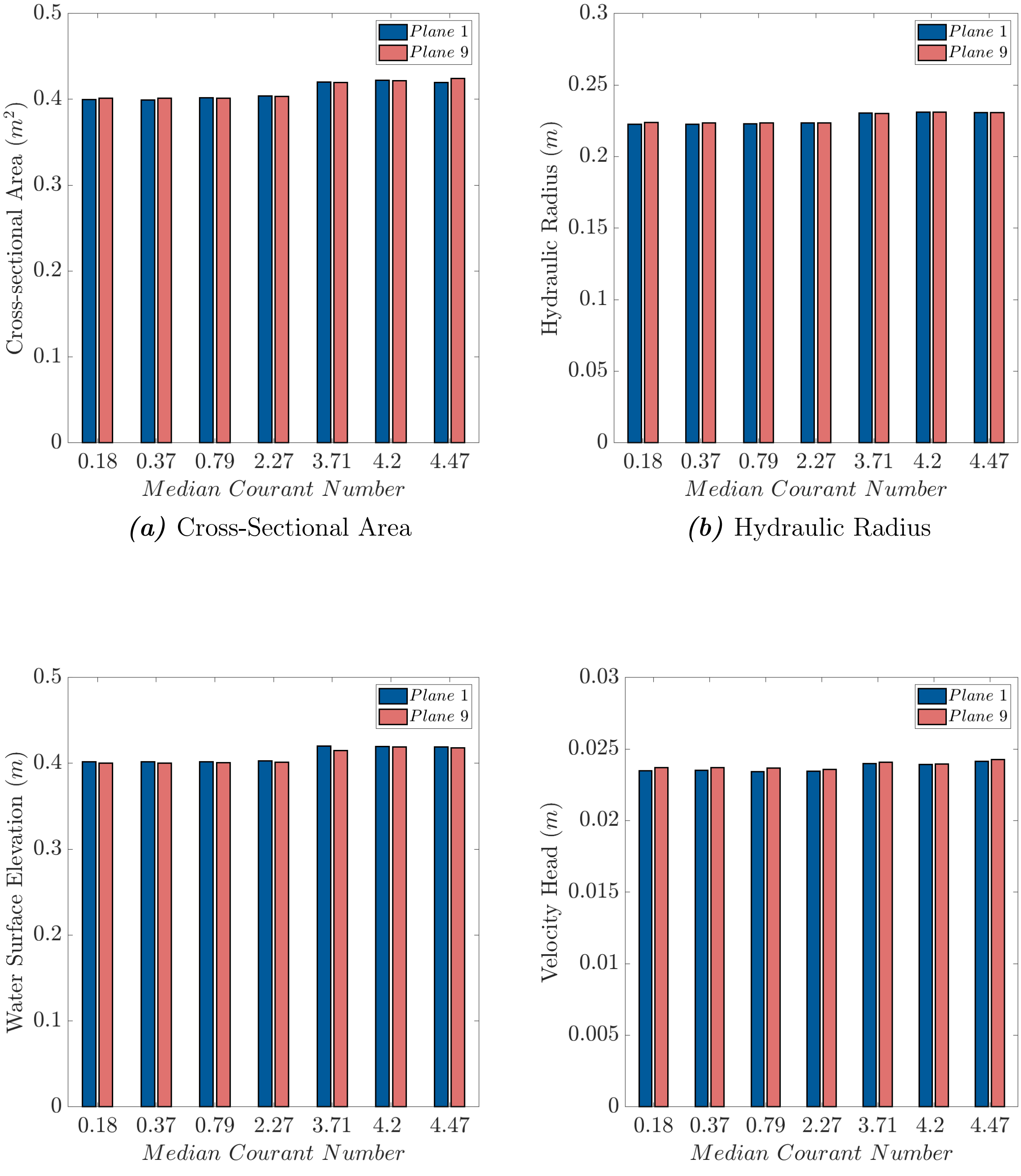

(a) Cross-Sectional Area

(b) Hydraulic Radius

(a) Water Surface Elevation

(b) Velocity Head

Figure 7.10. Evaluation of Sensitivity to Changes in Manning's Equation Variables.

7.2 Results of the 3-D models

7.2.1 Water surface elevation

The investigation into the influence of meanders on water surface elevation during the modelled conditions allowed for assessing how meandering affects the displacement of the water level. Figure 7.11 provides a visual representation of the distribution of water surface elevation along a straight channel, which serves as a baseline for understanding the impact of meanders. As expected, minimal variability was observed along the channel's centerline, where the water surface elevation exhibited a relatively consistent decrease between planes P1, P5, and P9. Over a distance of 3.89 meters, the water surface elevation decreased by 0.002 meters from P1 to P9.

However, the condition changed further away from the centerline and closer to the channel banks. Examining the role of channel walls in shaping water surface elevation revealed a concentration of data points near the banks, indicating substantial fluctuations in water levels.

Contrary to expectations, the best-fit lines were not parallel to each other. Instead, they exhibit an inclination towards the inner bank.

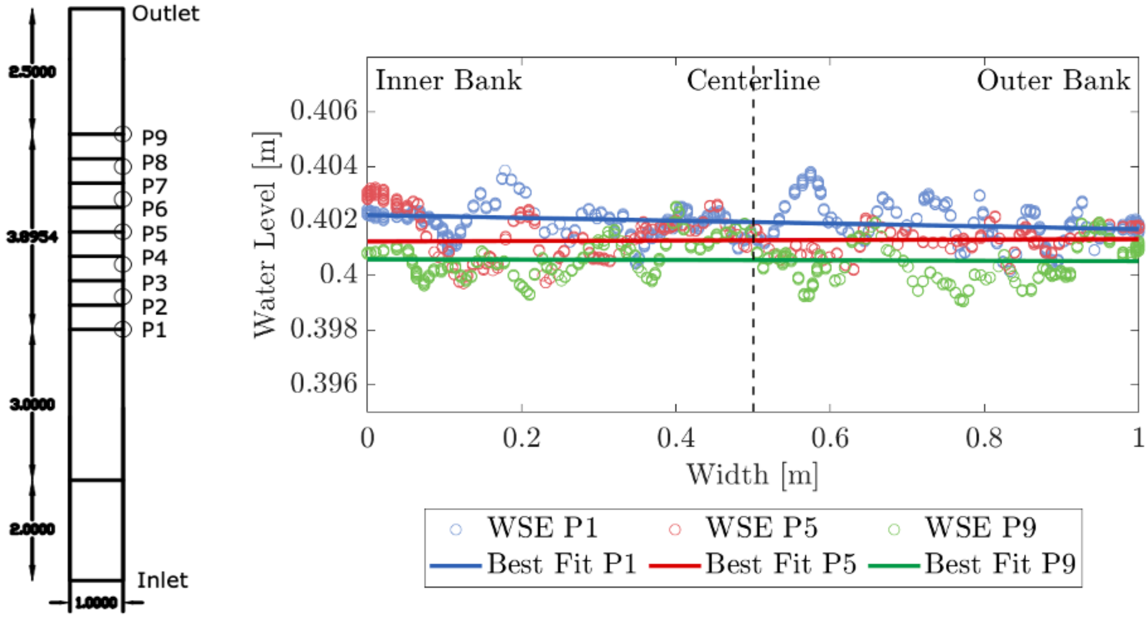

Figure 7.11. Water surface elevation distribution at planes P1, P5 and P9 for the model C=0.

Figure 7.12 provides a visual representation of the water surface elevation profile of model C = 0.31, which incorporates a meander. The figure confirms the hypothesis that meandering influences the displacement of water levels between the inner and outer banks of the stream. The discrepancy in water elevation was more pronounced than in the C = 0, as indicated by the difference between the inner and outer banks at different points along the stream.

The observed water surface elevation variation between the inner and outer banks at position P5 was 0.0153 meters. However, considerable disparities become apparent when comparing these measurements to planes P1 and P9, where the differences represent approximately where the observed variations were 0.0079 and 0.0077 metres for P1 and P9, respectively.

It is interesting to note that the inner bank, particularly at P5, exhibits the lowest water surface elevation, with an elevation of 0.395 meters, 0.004 meters lower than that observed at P1.

Notably, the variations in water surface elevation were not limited to the banks alone but extended to the channel's central region. The section along the meander centerline demonstrates that water progression at P5 is restricted, leading to nearly identical water surface elevation values observed at P1, followed by a steep decrease at P9.

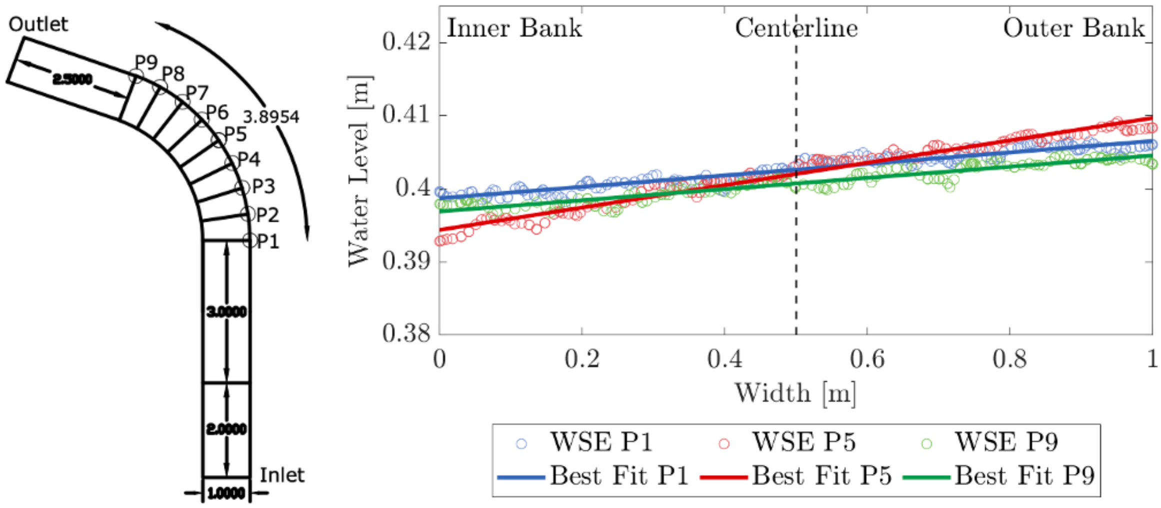

Figure 7.12. Water Surface Elevation distribution at planes P1, P5 and P9 for the model C=0.31.

Figure 7.13 depicts the water surface elevation profile under the influence of a curvature value of C=0.63, where the effects of centrifugal forces become significant. The surface elevation attains a height of approximately 0.42 meters at the outer bank, which is 0.01 meters higher than the surface elevation observed at a curvature of C=0.31.

The increased curvature at C=0.63 leads to a more influential impact of centrifugal forces on the displacement of the water level. This indicates that the water is more strongly affected by the outward-directed forces due to the curvature, resulting in an elevated surface elevation compared to C=0.31 values. The slope observed along the centerline, specifically between planes P1, P5, and P9, closely resemble the slopes observed in the C=0 model in terms of the elevation at the centerline at each plane. In contrast, when considering the C=0.31 model, the water surface elevation between these points along the centerline was more compressed, indicating smaller differences in elevation. This suggests that at C=0.63 there are larger differences in the water surface elevation compared to the curvature of C=0.31. Furthermore, the slope between the inner and outer planes of the water surface exhibits a notably steeper profile at C=0.63 compared to C=0.31. This implies that the transition of the surface elevation from the inner to outer bank occurs at a steeper angle, indicating a more pronounced change along the curved channel.

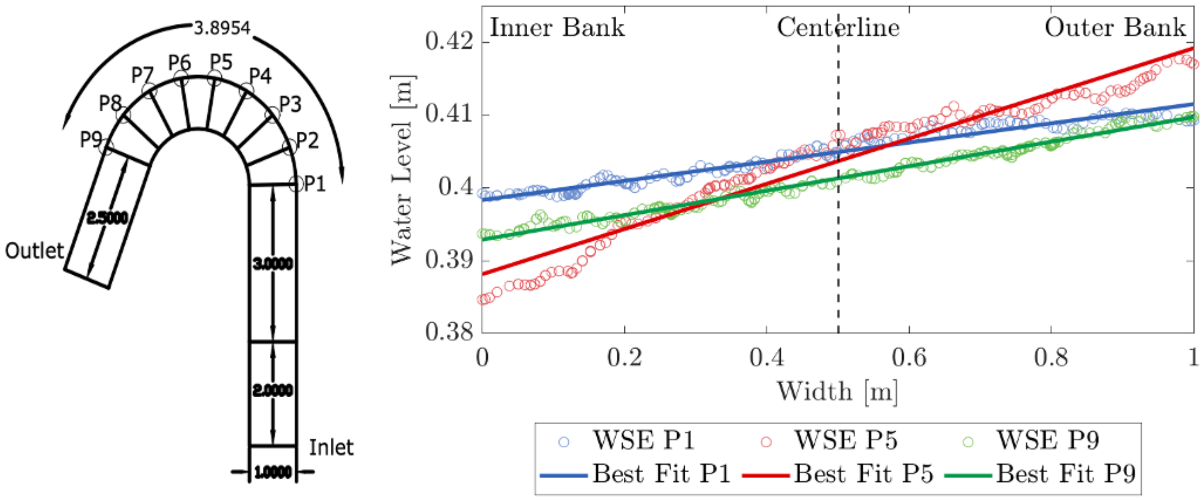

Figure 7.13. Water surface elevation distribution at planes P1, P5 and P9 for the model C=0.63.

7.2.2 Comparison of the stream-wise velocity and secondary circulation patterns

The velocity distributions, quantified as stream-wise velocity and secondary circulation, had spatially varying sensitivity to curvature, as displayed in Figures 7.13, 7.14, and 7.15. In the C=0 model, the velocity distribution remained relatively constant along the channel. In all three planes, the lowest velocities were observed near the walls, both at the bottom and along the banks. The highest velocities were present in the central part of the channel, although slightly decreasing towards the air-water interface. Secondary flows were not observed in these planes, and some small turbulence in the vertical direction was present throughout the water column.

When the curvature was increased in C=0.31, clear patterns of the velocity being displaced towards the inner bank were observed, as seen in Figure 7.14. At P1, the stream-wise velocity was decreased from the inner bank towards the outer bank, and the velocity seemed uniformly vertically distributed. Secondary circulation could not be observed in this plane. However, the vectors indicate that the flow shifted towards the inner bank due to the curvature of the section. Maximum velocities were observed at the inner bank of P5, Figure 7.14b. Besides this, a clear reduction of the stream-wise velocity in the outer-bank direction was present. At this point, secondary circulation patterns started appearing. Two clearly defined cells were observed, one in the top outer zone in the counterclockwise direction and the other at the bottom inner part with a circulation in the opposite direction. These secondary circulation phenomenons were enhanced when reaching the outside of P9, as illustrated in Figure 7.14c. However, the stream-wise distribution patterns were quite different; the largest velocities were displaced towards the centre of the channel, while a zone of relatively low velocities were generated at the upper part of the inner bank, corresponding to a zone of low-pressure typically generated after the apex of the bend.

The behaviours observed in the C=0.31 model were enhanced when the curvature was increased at C=0.63, as displayed in Figure 7.15. At P5 the water was pushed towards the outer bank. Therefore, the velocity was increased in the inner bank. When the water starts to leave the bend at P9, the water followed a straight movement, resulting in higher velocities at the centre of the channel. Once again, an area of lower velocity was observed at the top part of the inner bank, which was larger compared with C=0.31. However, recirculation was not observed in this area despite the degree of curvature. Regarding secondary circulation, in both P5 and P9, the centre of rotation of the uppermost cell was displaced to the central part of the transverse sections. In this order, these secondary cells became more noticeable in the planes.

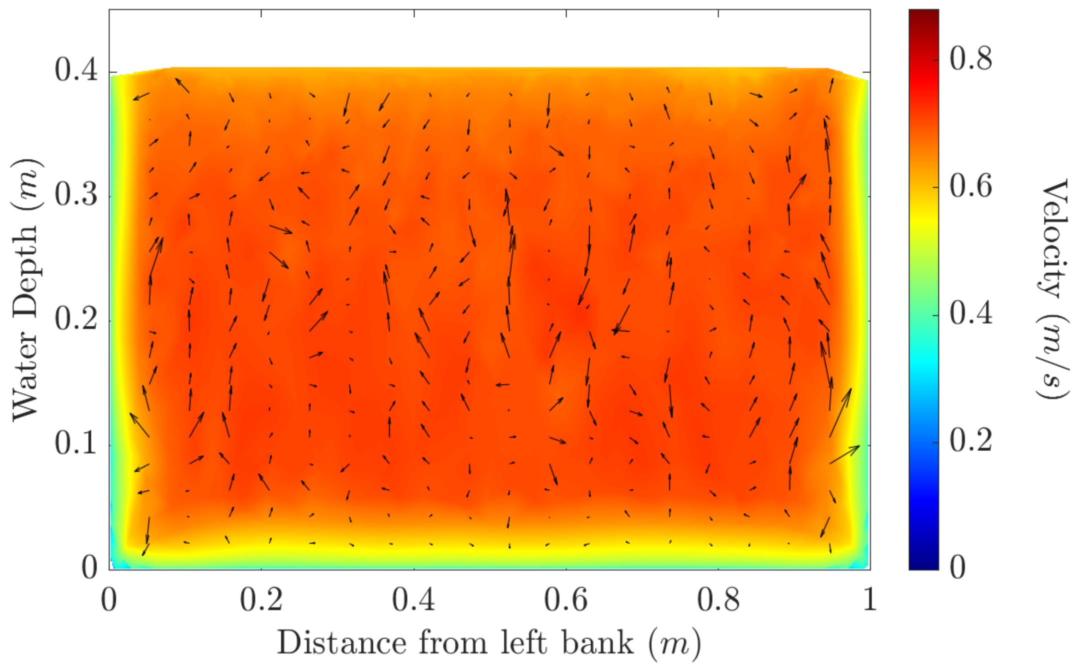

(a) P1 - C=0

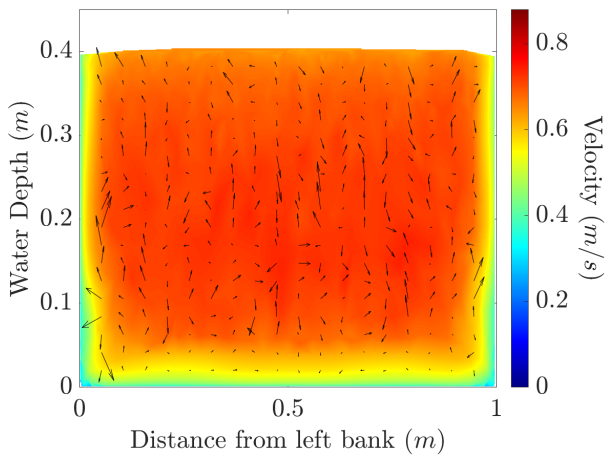

(b) P5 - C=0

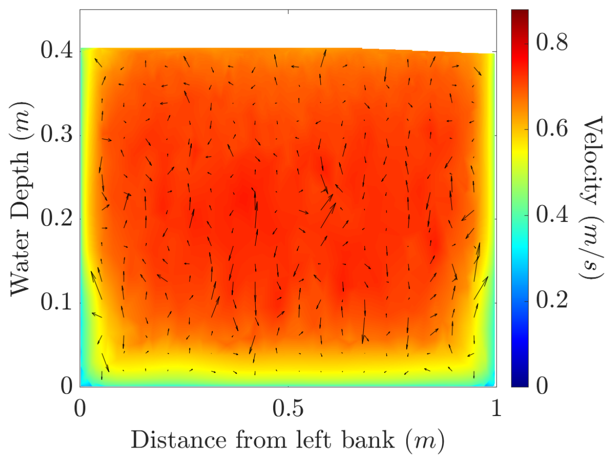

(c) P9 - C=0

Figure 7.13. Stream-wise velocity distribution with secondary circulation flow at planes (a) P1, (b) P5, and (c) P9, for model C=0.

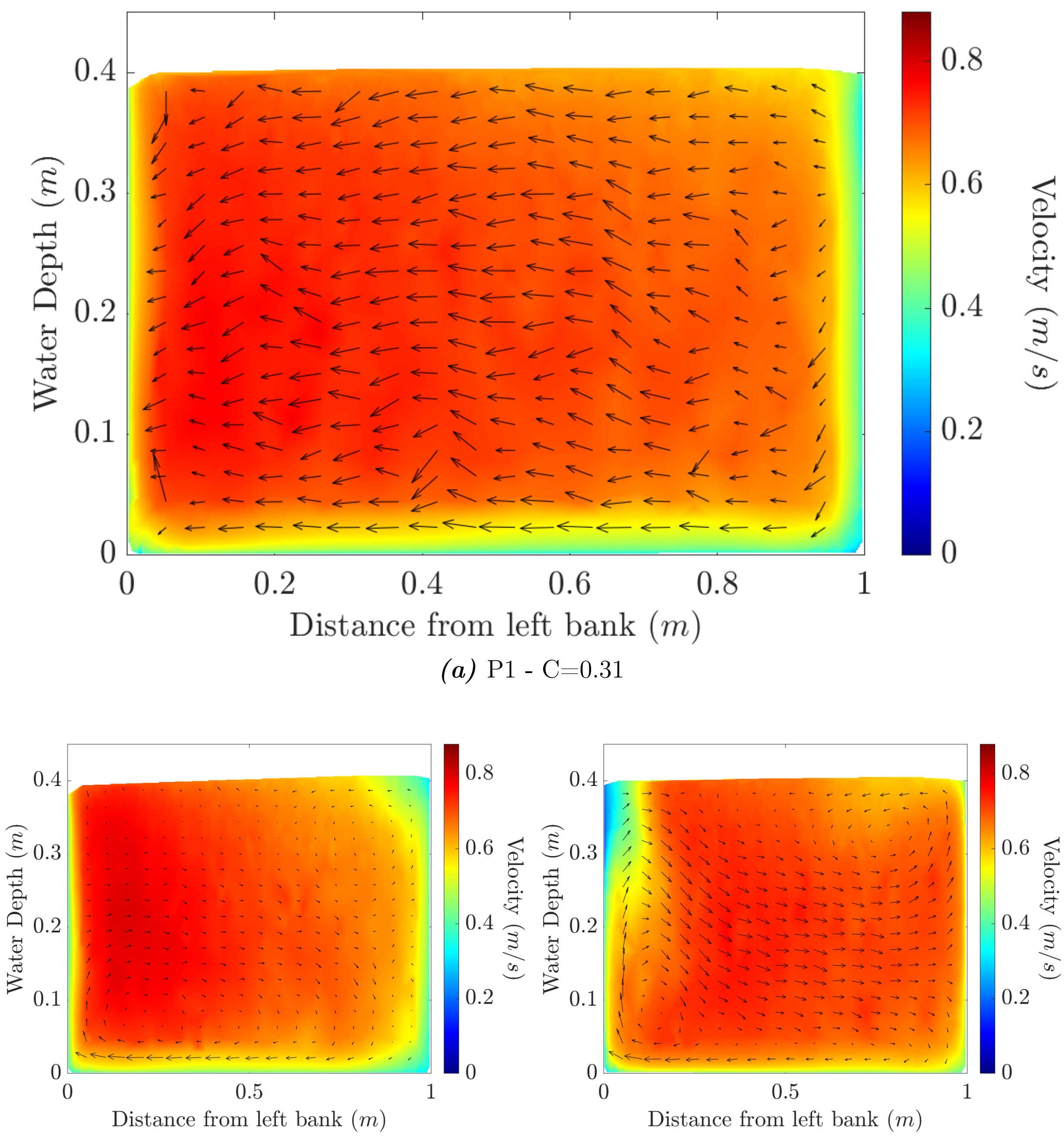

(a) P1 - C=0.31

(b) P5 - C=0.31

(c) P9 - C=0.31

Figure 7.14. Stream-wise velocity distribution with secondary circulation flow at planes (a) P1, (b) P5, and (c) P9, for model C=0.31.

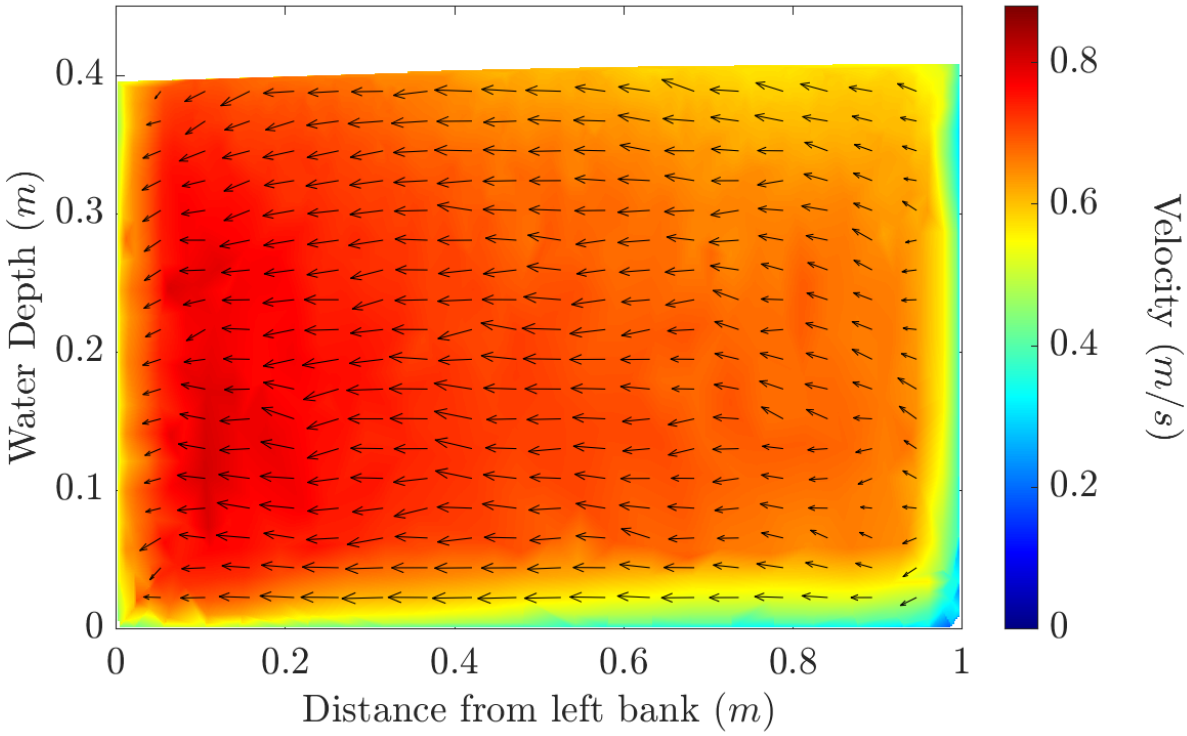

(a) P1 - C=0.63

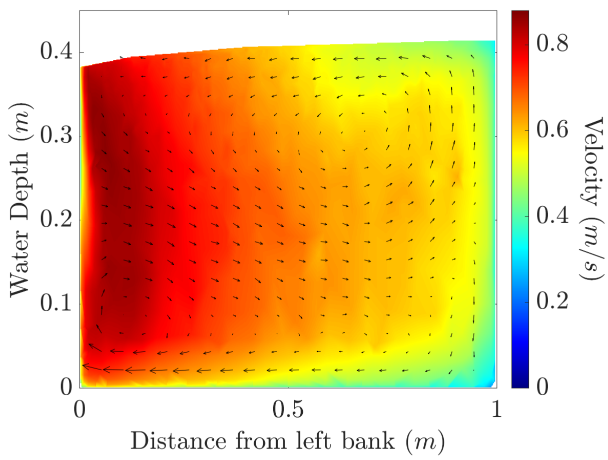

(b) P5 - C=0.63

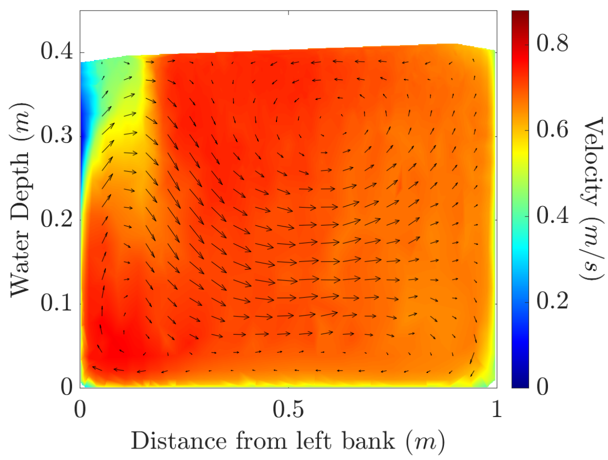

(c) P9 - C=0.63

Figure 7.15. Stream-wise velocity distribution with secondary circulation flow at planes (a) P1, (b) P5, and (c) P9, for model C=0.63.

7.2.3 Manning's n as a result of 3-D modelling

The roughness coefficient between planes P1 and P9 was estimated for each curvature with the data extracted from the CFD model by applying the basic form of Mannig's equation, Equation 6.1.

The energy gradient between planes was calculated using Equation 6.2. The water surface elevation value, h, corresponded to the water level at the centre-line of the geometry at each plane. Furthermore, the velocity head at each plane was calculated using the average stream-wise velocity. The velocity distribution coefficient (α) at each plane was estimated with Equation 5.1. Finally, the cross-sectional flow area and the hydraulic radius were extracted from Star CCM+. The values used for each described parameter can be found in Table 7.3.

Table 7.3. Parameters used for the calculation of Manning's roughness coefficient between Plane 1 and Plane 9 for the different modelled curvatures. Values in brackets correspond to M.

Model	**Plane 1**			**Plane 9**			**A**	**R**	**I**	**n**
	$\boldsymbol{\alpha}$	**h** $[m]$	$\mathbf{h_v}$ $[m]$	$\boldsymbol{\alpha}$	**h** $[m]$	$\mathbf{h_v}$ $[m]$	$[m^2]$	$[m]$	[‰]	$[s/m^{1/3}]$
C=0	1.03	0.40	0.023	1.04	0.40	0.024	0.40	0.22	0.29	0.0094 (106)
C=0.31	1.04	0.40	0.024	1.04	0.40	0.024	0.40	0.22	0.52	0.0124 (80)
C=0.63	1.04	0.41	0.024	1.031	0.401	0.024	0.40	0.22	0.94	0.0168 (59)

Under the modelled flow conditions, an increase of n was observed corresponding to the degree of curvature, as displayed in Figure 7.16. An increase of 32% and 79% was observed from the C = 0 model to the C = 0.31 and C = 0.63, respectively. Moreover, due to the short distance between planes, the differences in water surface elevation and velocity head were imperceptible. However, those small differences reflect significant differences between the energy gradients in the different models.

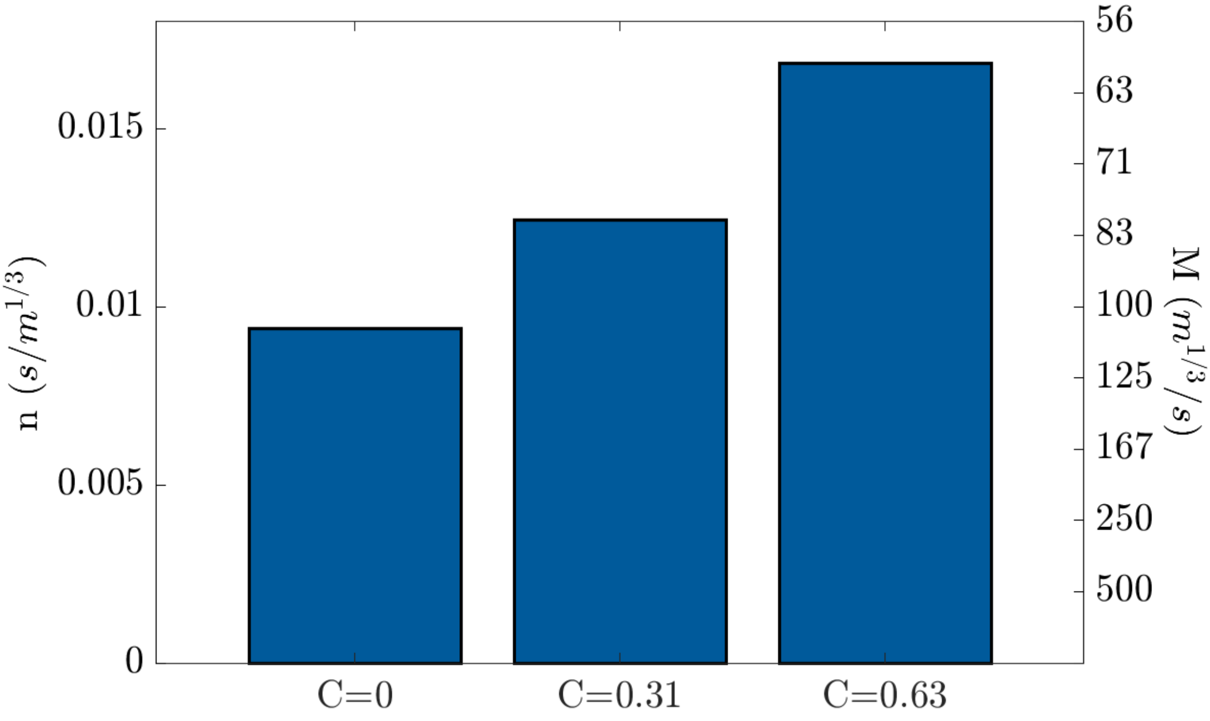

Figure 7.16. Manning's roughness coefficients for the three models with different curvature.

7.3 Discussion of 3-D modelling

7.3.1 Construction of model

To improve the hydraulic similarities between the 3D model and Binderup Å, changes to the dimensioning of the geometry could be made. Specifically, aiming to increase the hydraulic radius of the 3D model to match that of the stream would be appropriate, as this would mean a better replication of the friction forces being imparted on the fluid. Additionally, the selection of a more appropriate wall roughness would be an important step in replicating the conditions found in a natural stream.

To isolate the impact of the degree of curvature on n, the bed of the stream was kept flat, keeping the degree of curvature as the only independent variable. However, it is important to note that this approach results in a velocity profile that is opposite to that of a natural stream. Consequently, conducting further analysis on the degree of transverse bed slope on n would be an appropriate follow-up investigation.

This study was limited to three geometries, two of which were curved, limiting the ability to define a precise relationship between curvature and n. Including a wider variety of curvatures would provide a more substantial data set to possibly propose a more definite relationship between C and n.

7.3.2 Model selection

It was assumed that accurate simulation of the near-wall forces and particularly generation of turbulence would be important factors in accurately replicating the effects of curvature on n, as this turbulence is a significant contributor to energy loss in stream systems.

The Realizable K-epsilon two-layer model was chosen as it provides a balance between accuracy and computational time. It does, however, have some limitations in accurately resolving near-wall turbulence. Alternative turbulence models that could more accurately resolve the turbulence in these regions, such as the K-omega model, could have been utilized, but at the scale modelled in this study, the additional accuracy was assumed to not be significant enough to outweigh the additional computational time. Conversely, a larger near-wall mesh resolution could have been applied, taking advantage of the All Wall y+ Treatment's ability to handle larger y+ vales. However, high y+ wall treatment does not fully resolve turbulence calculations, but rather uses a logarithmic law to approximate the velocity profile in the cells it is applied. This could mean that any influence that turbulence in adjacent cells may have on a given cell governed by the high y+ treatment is not fully accounted for.

The VOF wave model was chosen to include the impact of the air-water interface as it interacts with the stream banks. The limitations of this model were that the irregularities on the water surface may have caused some warping of the results, for example the slight deviation in the transverse surface slope from the anticipated path in C=0. Additionally, the fluctuations caused increased computational time and extended periods before reaching equilibrium as opposed to a single-phase or simple two-phase model.

7.3.3 Velocity scaling

The velocity of the model was scaled up to match the Reynolds number with that found in the stream. This had the consequence of scaling the Froude number in the opposite direction, meaning the conditions on the surface, such as the transverse slope, would not be directly relatable to the measurements taken in the stream. The Froude number of the models was calculated to be 0.34, approximately twice that measured in the streams. Nevertheless, as the model was aimed at isolating the effect of curvature and not necessarily replicating the conditions in the stream, the results can still be considered valid when considering a channel of this geometry under these hydraulic conditions.

The velocity might not have needed to be scaled up quite as high as it was, as the Reynolds number was above 100,000, meaning that the velocity could have been reduced while maintaining turbulent conditions. In that way, a similar Froude number to the one observed in Binderup Å could have been used, and the turbulent conditions maintained. Then, the modelled transverse slopes would have been similar to the present in the natural stream.

In general, the transverse slopes in natural bends are almost imperceptible. Therefore, if the computational time needs to be reduced, a good option may be building a closed-lid model instead of a VOF model.

In a single-phase model, the general velocity distribution of the bend should also be observed but the transverse slope would not be present. However, as the transverse slope in natural streams is smaller than the one observed in the presented models, the resulting calculations of n could be closer to reality.

7.3.4 Wall y+ values and Courant Number

The distribution of wall y+ values for each of the three models typically lay within the optimal range of < 5 and $30 <$ y+ < 60, as can be seen in Figure 7.17, although it was not possible to keep 100% of the cells within this range. As y+ is a function of wall shear stress, and in turn velocity, this could be attributed to the distribution of velocities along the stream banks and bed.

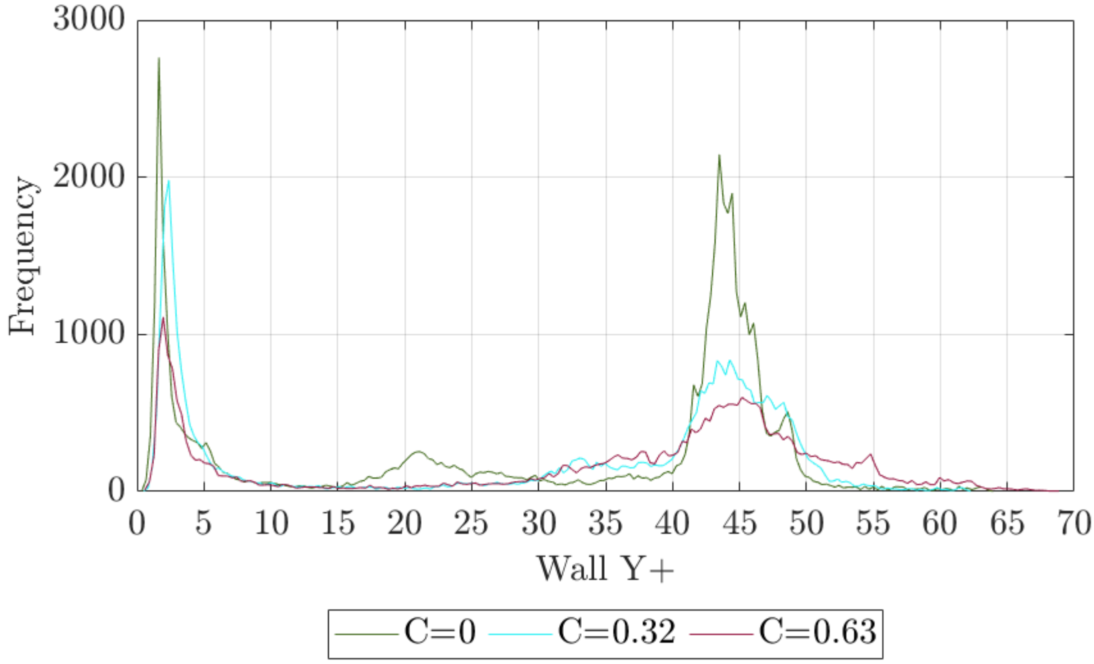

Figure 7.17. Distribution of wall y+ values between C=0, C=0.32, and C=0.63.

In the sensitivity analysis, the Courant number used to identify each model /quantify each models performance was the median value. This ignores the fact that the range of the Courant number in some models exceeded the recommended value of 1. For example, the upper quartile of the TS = 0.02 model sat at 1.31. This was not considered problematic owing to the model replicating results produced in the TS = 0.01 and 0.005 second models, in which the upper quartile lay 0.65 and 0.32 respectively. It should be kept in consideration that instabilities could occur in cells with a Courant number higher than one, resulting in invalid results in certain regions.

7.3.5 Validation of initial conditions

It was assumed that the constant elevation at the lower boundary would create an anchor point for the slope of the water to reach, while the constant velocity at the inlet would create a pressure gradient which would produce an elevation of the water level near the inlet via backwater effects, with any transitional phase between the lower boundary and the section at steady state expected to be negligible.

The results of the steady state assessment in the in- and outlet channels indicate that while not perfectly at steady state, the conditions were nearing steady state, with minimal changes in velocity between planes in the inlet channel, and minimal changes to the transverse slope in the outlet channel.

The impact of any unsteadiness moving into P9 was difficult to assess, and when considering the fact that natural streams will rarely, if ever, demonstrate a uniform steady state, the small variance observed between for example P_{i11} and P1 could be considered negligible. However, as the purpose of the 3D modelling was to isolate the effect of the bend to the greatest extent possible, this should still be considered an area of potential improvement.

7.3.6 Sensitivity Analysis

The TS of 0.1 was chosen to carry out the mesh size sensitivity due to time constraint. It would be ideal to have chosen a time step with a lower Courant number, as the minimum 25th percentile of the Courant number of any of the mesh analysis models was 2.45.

It is probable that the monitors used in the simulations to measure the water surface elevation between Planes 1 and 9, which were used to calculate the energy gradient, were affected by the change in cell size.

The sensitivity analysis was carried out only on C=0, as it was assumed that the change in TS and MBS would have a similar impact on the remaining geometries C = 0.31 and C = 0.63. The number of cells listed in Table F.1 illustrates that the volumetric discretization of the three domains differs. Therefore, the assumption that the changes in TS or MBS would have a similar impact on C=0.31 and C=0.63 as they had on C=0 was inaccurate. However, this aspect was disregarded in favour of time management and the belief that the resulting changes in n would be negligible.

7.3.7 Modelled hydraulic conditions in the 3-D channels

The findings of the 3D modelling shed light on the influential role of centrifugal forces within meanders. As water traverses the bend, the outward-directed centrifugal forces displace the water toward the outer bank, resulting in a higher water level. Consequently, the inner bank experiences a relatively lower water level.

The change in water level throughout the bend seemed to be directly correlated with the grade of curvature. Moreover, the centrifugal forces have their maximum effect around P5, with maximum values at the outside of the apex and minimum elevation along the inner bank of the apex. This corresponds to what is expected to be found in natural channels, with high-pressure zones on the outside of the bend and lower pressure on the inner. As a consequence, the water is pushed down along the outer bank.

As the Froude number was not considered for the scaling process, the obtained transversal slopes may differ from those observed in a natural channel with similar geometry.

The velocity profile of water running through a uniform, flat-bottomed channel in the 3D models showed that the velocity gradient increased towards the inner bank of the bend. This contradicted what was measured in the stream but may be explained by the geometry of the modelled channel; being a flat bedded channel, the pressure gradient is dictated by the elevated water surface on the outer bank, owing to centrifugal forces. In a natural stream, however, the velocity distribution is also influenced by the topographic steering caused by the elevated bathymetry at the point bar, producing convective accelerations that increase the pressure in this area and a reduction in the pool. Moreover, in this new scenario, the transverse centrifugal force becomes larger than the opposite pressure gradient force. Therefore, in the outwards direction, an increase in flow is produced, and due to mass conservation, the velocity needs to be increased [Dietrich and Smith, 1983; Camporeale et al., 2007; Blanckaert, 2010].

On the other hand, a region of lower velocity was observed at the inner bank past the apex of the bend, which was enhanced with the degree of curvature. Even though a re-circulation was not present in the models, as might be expected in a natural bend, the reasons behind the deceleration are the same. The reduction of the water level at the inner side of the apex generates a positive pressure gradient in the flow direction around this area. Additionally, as the bend ceases, the region of high velocity shifts back across to the outer bank as the pressure gradient due to centrifugal forces diminishes. These two factors result in the stream-wise velocity being reduced, and in some extreme cases, counter-flow can be observed.

The observed secondary circulation described patterns that may be found in natural streams. The pressure gradient generated from the super-elevation at the outer bank produced the movement of the near-bed water towards the inner bank. The effect was predominant at the position of P9 where the larger transversal water surface slope is present. Moreover, the topmost cell observed in the models was larger than expected for natural streams.

Another significant difference between the modelled velocity profile and the one that would be expected in a typical natural stream was the two secondary circulation zones seen in Figures 7.15b and 7.15c. Here, the central region of flow in P5 maintained an outwards direction while along the air-water interface and the stream bed, the flow moved towards the inner bank. Further through the bend, at P9, this relationship had flipped, with the central region moving inwards and the upper and lower regions of flow moving towards the outer bank. One possible explanation for this is the ratio between the depth and width of the channel, causing the recirculation zones to split. In a natural stream, a smaller depth compared with the width would be expected, with the secondary cell moving from the outer towards the inner bank would be predominant in the profile.

Manning's roughness coefficients for the model were calculated using the same procedure as done for the real-world measurements. The roughness coefficient increased with the increase in curvature. However, as the largest velocities were obtained in the inner bank, the majority of the energy loss is expected to take place in this area as a result of larger turbulence, shear stress.

As this velocity profile does not match the typical profile of a natural stream, the losses may be disproportionate to those seen in a natural stream. This suggests an investigation of how this shift in region of high velocity affects n could be a valuable follow-up investigation.

7.3.8 Relating results of 3D modelling with analytical and 1D modelling

While the results of the 3D modelling are not directly relatable with the results of the analytical and 1D modelling approaches, the conclusions that can be drawn from each are similar.

The results of the analytical approach under low-flow conditions showed the value of n was 28% higher in the meandering than in the straight section using the standard Manning's equation and 20% higher using the NCALC method. The difference between these values resulting from the 1D modelling approach returned a difference of 25%. The results of the 3D modelling meanwhile showed that the n of the bend with a curvature of C=0.63 was

79% higher than the straight C=0 model. This difference was significantly higher, which could be explained by a variety of the factors discussed above. Notably, the difference in bed geometry and the hydraulic radius could be important factors in replicating the same hydraulic conditions and thereby more comparable results. The value of n in the intermediate bend, C=0.31, was 32% higher than in the straight model, slightly less than half that of the C=0.63 model. This could indicate a near-linear correlation between curvature and contribution to n, although more comprehensive investigations would be required to confirm this.

7.4 Conclusion of 3-D modelling

- It was proven that 3-D hydrodynamic models are powerful tools to assess the velocity distribution structures that are taking place in a bend.

- The modelling process and the obtained results have highlighted the necessity to include natural stream bathymetry in the study of natural bends if real-world flow patterns are to be accurately described. Consequently, further research is required to better understand and model these aspects accurately.

- The study utilizing CFD modelling has provided valuable insights into the complex hydrodynamics of meandering channels. The research findings contribute to our understanding of the intricate interplay between centrifugal forces, channel curvature, water depth, velocity, and secondary circulation. Further investigations and refinements are necessary to better capture the nuanced characteristics observed in natural streams and enhance the accuracy of CFD modelling in replicating real-world scenarios.
- The results of the 3D modelling show that increasing curvature correlates with increasing values of n. The precise relationship between the two has not been defined, but further investigations into a more comprehensive span of curvatures would help in defining this. Additionally, investigation into the relationship between stream bed geometry and velocity distribution, and in turn n, would be valuable additions to this study.

Summary of Findings 8

The ADCP demonstrated similar results to the propeller current meter while also providing a more comprehensive dataset. Despite requiring additional training and equipment, it offers greater time efficiency compared to the propeller current meter. Therefore, it was concluded to be a reliable, accurate and efficient method for collecting flow data in meandering stream sections.

Manning's equation has limitations when applied to meandering streams due to the presence of variable conditions. The equation assumes a single average area and may not fully capture the complexity of meandering streams. The NCALC method provides a more comprehensive analytical approach by accounting for the varying geometrical conditions throughout the stream. The increase in n between straight and meandering sections was estimated to be between 18% and 28% under low flow conditions and between 25% and 39% under high flow conditions.

The findings of this study demonstrate that under low flow conditions, the outcomes obtained using the 1D modelling approach exhibit minimal divergence when compared to the results derived from the NCALC or Manning's methods, despite incorporating detailed bathymetry and ADCP measurements. This approach enables straightforward verification of the n across diverse flow conditions, not only in the steady-state but also in unsteady flows that are particularly relevant in open channels. The estimated n values obtained through all three approaches return similar values of approximately 0.04 $s/m^{1/3}$ (M=25) for the straight section of the stream. There was a greater disparity between values calculated in the meandering section, where both Manning's equation and HEC-RAS yielded a value of 0.051 (M=19.6) $s/m^{1/3}$, whereas the NCALC method yielded a value of 0.048 (M=20.8).

For any real-world application where the hydraulic conditions of a stream need to be studied, the uncertainty of n needs to be considered.

In this study, no significant advantage to utilising the more time-consuming methods (NCALC and HEC-RAS) was found over using the standard Manning's Equation. Nevertheless, the conditions of the stream should still be considered when choosing the appropriate method.

The curvature of meandering streams had a direct influence on n value. All three methods (analytical, numerical, and CFD) employed in the study demonstrate that meanders increase the value of n. 3-D modelling revealed a correlation between increased degrees of curvature and higher values of n, which increased by 32% and 79% from the C = 0 model to the C = 0.31 and C = 0.63, respectively. However, this assessment was conducted on only two variations of curvature with a different hydraulic radius and minimal surface roughness. Further investigation is required to assess specific cases and obtain more conclusive results.

9 Perspectives for Future Research

Based on the findings, challenges, and analysis conducted during the course of this project, several avenues for future investigation are proposed.

The velocity distribution profile influences the distribution of energy losses along the stream. Therefore, it could be expected to observe different energy gradients in situations where a bed is preceded by a long straight channel compared to those by a bend. In the former, the flow is expected to reach the bend with a typical profile of larger velocities in the centre and lower close to the banks. While for the latter, it would be expected to see this distribution shifted towards one side entering the bend. These particularities in the velocities distribution could be studied with field ADCP velocity measurements, if the proper site is found, or by CFD modelling of the desired conditions.

As was pointed out in this report, topographic steering has a large role in the velocity distribution both in the longitudinal and transversal direction of the stream. Therefore, based on CFD modelling, a study could be carried out where a series of bends are modelled. These bends must share the same curvature, but the transversal slope has to be gradually increased. In this way, it would be possible to estimate the effects of the bathymetry on the velocity distribution and determine the point where the inner-bank circulation is shifted towards the outer bank.

Regarding the ADCP measuring process, further studies can be done on the method's reliability. One interesting approach could be to evaluate how the flow measurement results vary with the increased quantity of transects taken at one location. Moreover, the required total measuring time could also be evaluated. Therefore, suggestions about the recommended number of transects and total measuring time at each cross-section could be made. Besides this, a recommendation for the extrapolation method utilised in the unmeasured regions based on certain environmental conditions could be investigated. These environmental conditions could include stream-bed substrate, near bank shape and wind velocity, direction and magnitude. The findings may result in recommendations for the best-fitting method to be used as a function of the stream condition.

Several methods for quantifying the preferred hydraulic conditions for the development of biodiversity have been proposed. Some of them are based on the estimation of velocity distribution gradients. Differences in velocities along the stream generate heterogeneous physical conditions that enhance the conditions needed for different organisms to thrive. The ADCP could be used to measure the velocity profiles throughout a stream reach and assess certain biodiversity metrics. As proposed by Crowder and Diplas [2000], these spatial velocity gradients can be used to correlate the degree of curvature with biodiversity growth. Moreover, the relationship between biodiversity and flow could be evaluated between straight and meandering streams. The aim could be to get recommendations for the minimum flow needed for biodiversity to develop depending on the degree of meandering.

With increased meandering, the flow capacity of a stream will reduce as resistance increases. The consequence of this is a higher water level and increased risk of flooding upstream of the site, while promoting biodiversity with increased habitat area for benthic life. An investigation could therefore be carried out on what the optimal degree of curvature would be needed to optimise the balance between improved ecological status with acceptable flood risk in a given stream.

Moreover, several investigations have shown that it is possible to estimate the concentration of solids suspended in the water column by using the back-scatter energy measured by the ADCP [Dwinovantyo et al., 2017; Baranya and Józsa, 2013]. In principle, two main investigation lines arise from this possibility. On the one hand, finding a correlation between the back-scatter data and the concentration of sediments in each ensemble. In order to do this, water samples at different depths must be taken at the same time and location where the ADCP measurement is taking place. Moreover, a correlation between back-scatter data and suspended solids could be found and applied in different scenarios. Thereafter, the new insights into solid concentrations could be used to gain more knowledge of the distribution of particles in a bend and a better understanding of the sedimentation and erosion processes that are taking place in the area.

Bibliography

Andersen, A. (1989). Profilopmålingens betydning for vandspejlsberegninger med den hydrauliske vandløbsmodel VASP. Technical report, Hedeselskabet, Forskningsvirksomhed, Beretning nr. 40.

Baattrup-Pedersen, A. and Riis, T. (1999). Macrophyte diversity and composition in relation to substratum characteristics in regulated and unregulated danish streams. *Freshwater Biology*, 42:375–385.

Baranya, S. and Józsa, J. (2013). Estimation of suspended sediment concentrations with ADCP in Danube River. *Hydrol. Hydromech*, 61(3):232–240.

Barnes, H. (1967). Roughness characteristics of natural channels. *U.S. Geological Survey Water-Supply Paper*, 1849:213.

Bilgil, A. and Altun, H. (2008). Investigation of flow resistance in smooth open channels using artificial neural networks. *Elsevier, Science Direct*, 19:404–408.

Bisht, T. (2020). The form, flow and dynamic character of meanders in a lowland river. *ProQuest*, 28120186.

Blanckaert, K. (2010). Topographic steering, flow recirculation, velocity redistribution, and bed topography in sharp meander bends. *Water Resources Research*, 46(9).

Bray, D. (1979). Estimating average velocity in gravel-bed rivers: American Society of Civil Engineers. *Journal of the Hydraulics Division*, v. 105, no. HY9:p. 1103–1122.

Brookes, A. (1990). *Channelized rivers: perspectives for environmental management.* Wiley, New York.

Brorsen, M. and Larsen, T. (2009). *Lærebog i hydraulik*, 2. Edition. Aalborg Universitetsforlag. ISBN: 978-87-7307-978-2.

Camporeale, C., Perona, P., Porporato, A., and Ridolfi, L. (2007). Hierarchy of models for meandering rivers and related morphodynamic processes. *Reviews of Geophysics*, 45(1).

Chambers, P., Prepas, E., Hamilton, H., and Bothwell, M. (1991). Current velocity and its effect on aquatic macrophytes in flowing water. *Ecological Applications*, 1(3):249–257.

Champion, P. D. and Tanner, C. C. (2000). Seasonality of macrophytes and interaction with flow in a New Zealand lowland stream. *Hydrobiologia*, 441:1–12.

Chauhan, M. S., Dikshit, P. K. S., Kumar, V., and Dwivedi, S. (2014). Comparison of discharge data using ADCP and current meter. *International Journal of Advances in Earth Sciences*, 3(2):81–86.

Cheng-Lung, C. (1991). Unified theory on power laws for flow resistance. *Journal of Hydraulic Engineering*, Vol. 117, No. 3:371–389.

Chow, V. T. (1959). *Open Channel Hydraulics*. McGraw-Hill Book Company, Inc.: New York, NY.

Coon, W. F. (1997). *Estimation of Roughness Coefficients for Natural Stream Channels with Vegetated Banks*. U.S. Geological Survey water-supply paper: 2441).

Cowan, W. (1956). *Estimating hydraulic roughness coefficients*. 37. Agricultural Engineering.

Crowder, D. W. and Diplas, P. (2000). Evaluating spatially explicit metrics of stream energy gradients using hydrodynamic model simulation. *Canadian Journal of Fisheries and Aquatic Sciences*, 57:1497–1507.

Dalrymple, T. and Benson, M. (1967). Measurement of peak discharge by the slope-area method. *U.S. Geological Survey Techniques of Water-Resources Investigations*, book 3, chap. A2:p. 12.

Danish Meteorological Institute. Vandstand. https://https://www.dmi.dk/vandstand/. Accessed: 10/02/2023.

Dash, S. S. and Khatua, K. K. (2016). Sinuosity dependency on stage discharge in meandering channels. *Journal of Irrigation and Drainage Engineering*, 142, Issue 9.

Dietrich, W. E. and Smith, J. D. (1983). Influence of the point bar on flow through curved channels. *Water Resources Research*, 19(5):1173–1192.

Doncker, L. D., Troch, P., Verhoeven, R., Bal, K., Meire, P., and Quintelier, J. (2009). Determination of the Manning roughness coefficient influenced by vegetation in the River Aa and Biebrza River. *Environmental Fluid Mechanics*.

Dwinovantyo, A., Manik, H. M., Prartono, T., and Susilohadi, S. (2017). Quantification and analysis of suspended sediments concentration using mobile and static Acoustic Doppler Current Profiler instruments. *Advances in Accustic and Vibrations*, 2017.

Fausch, K. D. and White, R. J. (1981). Competition between brook trout (Salvelinus fontinalis) and brown trout (Salmo truth) for positions in a Michigan stream. *Canadian Journal of Fisheries and Aquatic Sciences*, 38:1220 – 1227.

Ferguson, R. (2010). Time to abandon the Manning equation? *Earth Surf. Process. Landforms*, v.35:p. 1873–1876.

Ferguson, R. I. and Parsons, D. R. (2003). Flow in meander bends with recirculation at the inner bank. *Water Resources Research*, 39(11):1322.

Frasken, G. (1963). *Guide for Selecting Roughness Coefficient "n" Values for Channels*. US Dept. of Agriculture, Soil Conservation Service.

Fulford, J. and Sauer, V. (1986). Comparison of velocity interpolation methods for computing open-channel discharge, in Subitsky, S.Y. *Selected papers in the hydrologic sciences: U.S. Geological Survey Water-Supply*, Paper 2290:154 p.

Gordon, R. (1996). *Acoustic Doppler Current Profiler: principles of operation—a practical primer*. RD Instruments.

Hayes, J. and Jowett, I. (1994). Microhabitat models of large drift-feeding brown trout in three New Zealand rivers. *North American Journal of Fisheries Management*, 14:710 – 725.

Hofmeister, E. (2012). Den store å og bønderne. *Landhistorisk Tidsskrift*, 2:45–70.

Hulsing, H., Smith, W., and Cobb, E. (1966). Velocity-Head Coefficients in Open Channels. Technical report, United States Geological Survey, https://pubs.usgs.gov/wsp/1869c/report.pdf. Water Supply Paper 1869-C.

Jacobsen, L. B. (2010). Lystfiskernes bidrag til dansk økonomi. Technical report, Fødevareøkonomisk Institut Nr. 206.

Jarrett, R. (1984). Hydraulics of high-gradient streams: American Society of Civil Engineers. *Journal of Hydraulic Engineering*, v. 110, no. HY11:p. 1519–1539.

Jarrett, R. D. and Petsch Jr., H. E. (1985). Computer program NCALC user's manual - verification of Manning's roughness coefficient in channels. *U.S. Geological Survey Water Resources Investigations Report*, page 85–4317.

Jensen, K. S. and Mebus, J. R. (1996). Fine-scale patterns of water velocity within macrophyte patches in streams. *Oikos*, 76(1):169–180.

Khatua, K. K., Patra, K. C., and Nayak, P. (2011). Meandering effect for evaluation of roughness coefficients in open channel flow. *WIT Transactions on Ecology and the Environment*, 146:213 – 224.

Kim, J.-S., LEE, C.-J., KIM, W., and KIM, Y.-J. (2010). Roughness coefficient and its uncertainty in gravel-bed river. *Water Science and Engineering*, 3(2):217–232.

Lai, S., Nabil, B., Law, P., Aminuddin, A., Nor, A., and Mahyau, S. (2008). Discharge estimation for equatorial natural rivers with overbank flow. *Journal of River Basin Management*, 6, No. 1:13 – 21.

Limerinos, J. (1970). Determination of Manning's coefficient for measured bed roughness in natural channels. *Geological Survey Water-Supply Paper 1898-B*.

Madsen, J. (2021a). Profilændringer i Binderup Å. Technical report, WSP.

Madsen, J. (2021b). Undersøgelse af vandføringsevne i Binderup Å. Technical report, WSP.

Miljøstyrelsen. Vandløb. https://mst.dk/natur-vand/natur/national-naturbeskyttelse/3-beskyttede-naturtyper/beskyttelse-af-3-naturtyper/vandloeb/. Accessed: 03/11/2022.

Nash, J. and Sutcliffe, J. (1970). River flow forecasting through conceptual models part I—A discussion of principles. *J. Hydrol*, 10:282–290.

Ottevanger, W. (2013). *Modelling and parameterizing the hydro- and morphodynamics of curved open channels*. PhD thesis, Delft University of Technology.

Parsons, D. R., Jackson, P. R., Czuba, J. A., Engel, F. L., Rhoads, B. L., Oberg, K. A., Best, J. L., S.Mueller, D., Johnson, K. K., and Riley, J. (2013). Velocity Mapping Toolbox (VMT): a processing and visualization suite for moving-vessel ADCP measurements. *Earth Surface Processes and Landforms*, 38:1244–1260.

Pedersen, M. L., Kristensen, K. K., and Friberg, N. (2014). Re-meandering of lowland streams: Will disobeying the laws of geomorphology have ecological consequences? *PloS one*, 9(9):e108558.

Pedersen, T. C. M., Pedersen, A. B., and Madsen, T. V. (2005). Effects of stream restoration and management on plant communities in lowland streams. *Freshwater Biology*, 51(1):161–179.

Poulsen, T. G. (2005). Lecture book - advance statistical data treatment, 2005. . Lecture by Jesper Ellerbæk Nielsen, 2021.

Salim, S. M. and Cheah, S. (2009). Wall y+ strategy for dealing with wall-bounded turbulent flows. 2175.

Sand-Jensen, K. and Lindegaard-Petersen, C. (2004). *Ferskvandsøkologi*. Gyldendal.

SCALGO. Scalgo live documentation. https://scalgo.com/en-US/live-flood-risk. Accessed: 15/3/23.

Shields, F. D. and Rigby, J. R. (2005). River habitat quality from river velocities measured using Acoustic Doppler Current Profiler. *Environmental Management*, 36(4):565 – 575.

Shiono, K., Al-Romaih, J. S., and Knight, D. W. (1999). Stage-discharge assessment in compound meandering channels. *Journal of Hydraulic Engineering*, 125, Issue 1.

Siemens (2022). *Simcenter STAR-CCM+ Documentation*. https://www.plm.automation.siemens.com/global/en/products/simcenter/STAR-CCM.html.

Simpson, M. R. and Oltmann, R. N. (1990). An acoustic Doppler discharge measurement system. *Pro-ceedings of the 1990 National Conference on Hydraulic Engineering*, Vol. 2):903–908.

TeledyneMarine (2022). *WinRiver II Software User's Guide*. .

US Army Corps of Engineers (2022). *HEC-RAS Hydraulic Reference Manual*. Hydrologic Engineering Center.

U.S. EPA. Classification and types of wetlands. https://www.epa.gov/wetlands/classification-and-types-wetlands#tidal/. Accessed: 17/01/2023.

US Geological Survey (2022). *QRev—Technical Manual*. https://hydroacoustics.usgs.gov/software/QRev_Tech.pdf.

Verdonschot, P. and Nijboer, R. (2002). Towards a decision support system for stream restoration in the Netherlands: an overview of restoration projects and future needs. *Hydrobiologia*, 478:131–148.

Wiberg-Larsen, P. and Kronvang, B. (2016). Dansk Fysisk Indeks - DFI. Technical report, Aarhus University.

Wilzbach, M. A. and Cummin, K. W. (2019). *Rivers and Streams: Physical Setting and Adapted Biota*. Encyclopedia of Ecology, Second Edition, pages 294-606. Elsevier.

WSP and Miljøstyrelsen. Vandportalen. https://vandportalen.dk/plotsmaps?config=vandloeb&days=8763&end=29122022&id=101208-0-0&id=23953-0-0. Accessed: 11/01/2023.

Zhou, T. and Endreny, T. (2020). The straightening of a river meander leads to extensive losses in flow complexity and ecosystem services. *Water*, 12(6):1680.

Appendices

A Seasonal Variation at Binderup Å

Figure A.1 illustrates a seasonal variation at Binderup Å in water level and flow for the past 10 years. The water level ranges from 1.75 to 3.5 meters, while the flow fluctuates between 0.65 and 2.5 m^3/s. The lowest flow values with high water levels were reported in 2012, 2016, and 2017.

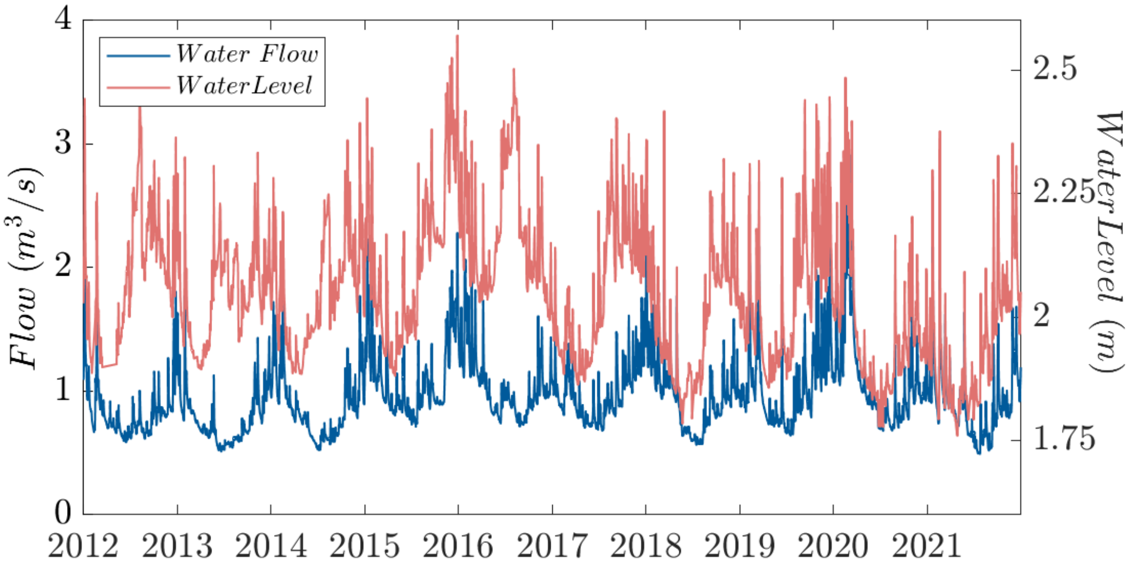

Figure A.1. Seasonal variation in water level and flow throughout 2012 - 2022. Data from WSP and Miljøstyrelsen.

B Measurement Methodology and Data Processing for ADCPs

Acoustic Doppler Current Profilers (ADCPs) are devices that use acoustic pulses to measure flow velocities and bathymetry in bodies of water. The ADCP used in this report was the StreamPro ADCP, which uses four transducers to send and receive an acoustic signal, each at an angle of 20° from the centre.

Particles in the water, assumed to be travelling at the same velocity as the water, reflect a portion of these acoustic signals back to the transducer. As these particles move relative to the ADCP, the frequency of the reflected signal shifts (a phenomenon known as the Doppler effect), correlating with the velocity of the particle through the water. This can be used to give a full velocity profile through the cross-section, as well as the bathymetry.

The measured velocity must account for the velocity of the boat. To account for this, either GPS tracking or bottom-tracking can be used to measure the velocity of the boat, which the measured velocity is then calibrated for. In high flow velocity conditions, sediment transport on the bed of the stream can give a false reading of the velocity of the boat when using the bottom-tracking method. To combat this, the moving-bed test can be carried out to calibrate for this condition.

A series of variables are filled out prior to commencing the measurements. While mostly for documentation, some of these are used by the ADCP software to predict how many measurements are expected, such as the expected maximum depth. This is used to split the water column into cells, or 'bins', the number and height of which are defined by an estimated maximum depth of the water body. For each of these cells, the ADCP takes measurements at a rate of 48 Hz, which are converted and presented as a single weighted mean velocity based on the temperature and pressure of the water, amongst other factors. The water temperature can be independently measured, but there is a thermometer built into the acoustic sensor which can be referred to in the data processing stage.

It is recommended to carry out a minimum of 720 seconds or four individual measurements on any single transect to achieve an accurate measurement. Measurements can not be taken from the edge of the bank, and therefore 10 seconds of measurements must be taken at the closest measurement point (usually 25-50cm from the bank) before proceeding across the stream to obtain a good measurement of this region.

The output of the ADCP is 3-dimensional velocity vectors, describing the flow of water through the given transect, as well as x-y-z values of the stream bed. It is important to carry out quality control in the measurement program, in this case, WINRiver II, before exporting to a program such as QRev to carry out further quality control and adjustment of parameters, as well as analysing velocity vector fields and other measures of hydraulic complexity.

B.1 Equipment Used

The main component required for these measurements to be carried out was the StreamPro ADCP and an accompanying laptop with WinRiver II installed. To ensure the repeatability of the path followed for each transect, a portable pulley-guided cableway was implemented. The following is a list of all of the components used for the ADCP measurements, including the setup of the cableway.

- StreamPro ADCP
- Computer with WinRiver II installed

  Cableway:
- 2x Wooden Stake
- 2x Pulley
- 2x Carabiner
- 2x Circular eye screw
- 20m Rope/String

B.2 Method

The following is a summary of the steps taken in acquiring measurements using the ADCP, as well as some tips and tricks/key things to remember during.

Method:

1. Set up the cableway across the target cross-section
2. Attach the ADCP to the cable and place it in the water to allow the thermometer to acclimatise.
3. Start the WinRiver II program, and set up the USB receiver.
4. Fill out the appropriate site, rating information and configuration dialogue.
5. Press F4 to start pinging. To start a new transect measurement, press F5. Distance to the shore is asked, and the starting position (LEFT or RIGHT bank).
6. Make an initial 10-second measurement at the start bank before dragging the ADCP across the stream at a maximum speed of half of the streamwise velocity.
7. Once ADCP reached the opposite bank, make another 10 seconds measurement in a static position before terminating the measurement. Distance to shore is asked.
8. Make a total of 720 seconds of measurements with at least 4 transects repeating steps 1-7.

Key things to remember:

- Data introduced in the 'Configuration Dialogue' impacts the results
  - 'Max. Water Depth [m]': one of the most important parameters because it defines the maximum measurement depth and the grid distribution. If it is too large, the grid will not be refined enough, and if is too small, some near-to-bottom area will not be measured.
  - 'Secondary Depth [m]': enter a secondary depth, such as the minimum depth you expect to be measuring.
  - 'Transducer Depth [m]': distance from the water surface to the transducer. It means how much the transducer has been submerged in the water.
  - 'Magnetic Variation [deg]': magnetic deviation from the true north of the place where the measurements are being taken. This parameter is not important when the measurement is done in Denmark, only if done in the Arctic.
  - 'Max. Water Speed [m/s]': an estimation of the mean water speed. It can be measured with a floating method.
  - 'Max. Boat Speed [m/s]': enter the expected maximum speed of the boat.
  - 'Temperature [°C]': important parameter because affects calculations. It can be changed during post-processing.
  - 'Water Mode': available options are 12 (normal water temperature) and 13 (cold water/freezing)

  - 'Discharge Top and Bottom Method': select interpolation method for top and bottom discharge. The power method is recommended. It can be changed during post-processing.
  - 'Bank coefficient': select the method to estimate close to bank discharge.
  - 'Shore Pings': number of pings to be considered in the shore discharge calculations. Select at least 10 pings.
- The ADCP can take upwards of 15 minutes to fully acclimatize/ accurately measure the temperature of the water. The temp. setting can be adjusted retroactively but should be kept in mind.
- Start and end points should be where 'a solid two-depth cell measurement' can be made.
- When departing and arriving at edges, slow acceleration and deceleration help ensure a good measurement, particularly at arrival, as overshooting the endpoint will result in poor area measurements.
- Each of the min. of four transects at each transect must be within 5% of the mean discharge calculated for the total set. If any are below (so that the min. of 4 transects is not reached), more transects would be required.
- When asked whether the measurement is taken from the LEFT or RIGHT bank, the choice should be made as though looking downstream. Besides, measurements must always be made from alternating sides.
- It could be an idea to make periodic measurements of water level (permanent ruler sticking in water) to account for tides and other causes of different water levels.

B.3 Data Processing

Once the data had been collected, a software called QRev was used to process and improve the quality of measurements. This program is the same one used by the U.S. Geological Survey to ensure that stream flow measurements are consistent, accurate, and independent of the manufacturer of the instrument used to make the measurement. QRev automates filtering and quality checking of the collected data and provides feedback to the user on potential quality issues with the measurement [US Geological Survey, 2022].

QRev provides an automated selection of an appropriate extrapolation fit for the measurement [US Geological Survey, 2022]. The automatically selected extrapolation method is the default method in QRev. However, the selected method should be reviewed to ensure a valid fit of the profile and make manual adjustments as appropriate.

The method for combining all transects into a single normalized plot and selecting the best-fit extrapolation for the data generates a discharge-weighted median. The measured discharge is the discharge for each valid cell and does not include estimates of the top, bottom, left edge, and right edge. The relative measured discharge of the ensemble is computed by dividing the absolute value of the sum of all valid depth cell discharges in an ensemble by the absolute value of the sum of depth cell discharges in the transect. The weight computed for an ensemble is applied to all cells within the ensemble. The weighted median is then computed using the cross-products and the discharge-derived weights. The weighted median gives more weight to ensembles containing greater discharge when determining the median used in the automatic method.

The automatic fit algorithms in QRev will select the best-fit method as followed. If the top is not represented by a power fit, the top is set to constant, and the bottom is set to no slip. The automatic fit algorithms will not select a constant fit for the top and power for the bottom fit. This is due to the fact that this combination creates a discontinuity at the top of the profile. If the profile does not follow a power fit, the bottom of the profile is better represented by the no-slip fit.

In the same way, the automatic fit algorithms will not select a three-point fit for the top. A three-point fit may be appropriate to some situations and can be manually selected. However, the automatic algorithms do not have the logic to automatically select a three-point fit for the top.

B.4 Flow Calculation

Total discharge is calculated as a sum, as seen in Equation B.1

$$Q = Q_{LeftEdge} + Q_{Top} + Q_{Measured} + Q_{Bottom} + Q_{RightEdge} \tag{B.1}$$

Table B.1. Summary of the available methods for discharge estimation.

Discharge Computational Methods		
Measured	Moving-Vessel Method (Eq. B.3)	TeledyneMarine [2022]
Top	Constant Fit (Eq. B.4)	Simpson and Oltmann [1990]
	Power Fit (Eq. B.6)	Cheng-Lung [1991]
	Three-points Fit (Eq. B.7)	US Geological Survey [2022]
Bottom	Power Fit (Eq. B.10)	Cheng-Lung [1991]
	No Slip	US Geological Survey [2022]
Edges	Ratio Interpolation (Eq. B.12)	Fulford and Sauer [1986]

Measured Discharge

The measured discharge is computed using the cross-product of the water and boat velocities. The equation for discharge in each depth cell, $\mathrm{Q_{bin}}$, can be written in terms of the water- and boat velocity vector components.

$$Q_{bin} = (V_w \times V_b) dt\ dz \tag{B.2}$$

V_w	Water velocity vector
V_b	Boat velocity vector
dt	Duration of the ensemble
dz	Depth cell size

The measured portion of the discharge can then be computed as follows:

$$Q_{Measured} = \sum_{j=1}^{Ensembles} \sum_{i=1}^{Bins} Q_{bin} \tag{B.3}$$

As QRev interpolates invalid depth, boat velocity, and water velocities, all of the necessary data are available to apply Equations B.2 and B.3.

Close surface discharge methods

The top discharge is computed using the selected top extrapolation method—constant, power, or three-point fit.

The **Constant Fit** assumes that the velocity in the topmost cell is a good estimate of the mean velocity between that depth cell and the water surface. With this method the top flow can be estimated with Equation B.4

$$Q_{Top} = \sum_{j=1}^{Ensembles} \chi(Z_{ws} - Z_{tb})dt \tag{B.4}$$

Where:

χ	velocity cross product in the topmost valid depth cell.
Z_{ws}	range from the streambed to the water surface.
Z_{tb}	range from the streambed to the top of the topmost valid depth cell.

The **Power Fit** is based on the power law and is represented in terms of cross product as shown in Equation B.5

$$\chi = \alpha z^b \tag{B.5}$$

Where:

α	Coefficient derived from a least-squares fit of the equation to the measured data.
Z	Range from the streambed to the location of the value of χ.
b	Exponent commonly assumed to be 1/6 (0.1667). However, it should be adjusted to fit the measured data.

The products found by applying the aforementioned equation are integrated over the range from the water surface to the top of the uppermost depth cell with valid water velocities using Equation B.6.

$$Q_{Top} = \sum_{j=1}^{Ensembles} \frac{\alpha}{b+1}(Z_{ws}^{b+1} - Z_{tb}^{b+1})dt \tag{B.6}$$

The **Three-point Fit** is the last possible method to estimate the discharge near the surface. This method uses the top three bins to estimate a slope, and this slope is then applied from the top bin to the water surface, see Equation B.7.

$$Q_{Top} = \left(\frac{Ad_T^2}{2} + Bd_T\right) dt \tag{B.7}$$

Where:

A and B	Parameters estimated using Equation B.8 and B.9, respectively.
$\mathrm{d_T}$	The range from the water surface to the top of the topmost valid bin.
$\mathrm{d_i}$	One of the top three valid bins.

$$A = \frac{3\sum_{i=1}^{3}\chi_i d_i - \sum_{i=1}^{3}\chi_i \sum_{i=1}^{3} d_i}{3\sum_{i=1}^{3} d_i^2 - \left(\sum_{i=1}^{3} d_i\right)^2} \tag{B.8}$$

$$B = \frac{\sum_{i=1}^{3}\chi \sum_{i=1}^{3} d_i^2 - \left(\sum_{i=1}^{3}\chi_i d_i\right)\left(\sum_{i=1}^{3} d_i\right)}{3\sum_{i=1}^{3} d_i^2 - \left(\sum_{i=1}^{3} d_i\right)} \tag{B.9}$$

Bottom discharge methods

ADCP, used for measuring water velocity, can face issues with side-lobe interference near the streambed, resulting in inaccurate readings. However, it is known that the water velocity at the streambed is zero, and fluid mechanics theory provides a logarithmic velocity profile to estimate the velocity in the boundary layer. Therefore, the power law equation is used to determine the discharge in the unmeasured portion of the water column, see Eqaution B.10.
Although this method is commonly used, it should be noted that it relies on certain assumptions and may not always reflect the true conditions in the stream or river [US Geological Survey, 2022].

$$Q_{Bottom} = \sum_{j=1}^{Ensembles} \frac{\alpha}{b+1} \mathbf{z}_{bb}^{b+1} dt \tag{B.10}$$

Where:

$\mathbf{z}_{\mathrm{bb}}$	Range from the stream-bed to the bottom of the bottom-most valid depth cell.

In cases where a logarithmic velocity distribution does not hold, such as for bidirectional flow, the **No Slip** method can improve the accuracy of discharge estimation. This method uses the power law equation B.5 but limits the least-squares determination of α to the bottom 20% of the water column. When valid depth cells are not available in the bottom 20%, the last valid depth cell is used instead to calculate α. By applying this method, it is possible to obtain more accurate results of water velocity and discharge in the unmeasured sections of the water column.

Edge discharge methods

Here, the mean flow velocity through the first or last segment, V_m, is multiplied by the specified length to the shore, L, and the depth of the adjacent segment (first or last), d_m.

$$Q_{Edge} = A_{Edge} V_{L/2} = 0.5 L d_m * V_m \frac{\sqrt{0.5 d_m}}{\sqrt{d_m}} = 0.3535 L d_m V_m \tag{B.11}$$

Where:

$\mathrm{Q_{Edge}}$	Estimated discharge in the unmeasured edge.
$\mathrm{A_{Edge}}$	Area of the unmeasured edge.
$\mathrm{V_{L/2}}$	Velocity midway between the bank and the first or last measured ensemble.
L	Distance from the last valid ensemble to the edge of the water.

Equation B.11 can be written in a more general form, which uses an edge-shape coefficient (C). The edge-shape coefficient depends on the shape of the bank; 0.355 for a triangular or 0.91 for a squared bank.

$$Q_{Edge} = C V_m L d_m \tag{B.12}$$

B.5 GPS Coordinates of performed cross sections

Table B.2. Spacial coordinates of the beginning and end of the cross-sections during low-flow conditions.

	Left Bank		Right Bank	
	Easting	**Northing**	**Easting**	**Northing**
$\mathbf{M1_1}$	540720.6996	6318118.5002	540722.6006	6318120.8990
$\mathbf{M1_2}$	540725.6001	6318126.4663	540728.6773	6318127.9999
$\mathbf{M1_3}$	540728.1564	6318133.8102	540731.3516	6318135.8214
$\mathbf{M1_4}$	540721.9865	6318135.3285	540722.6900	6318138.0283
$\mathbf{M1_5}$	540715.0017	6318131.4052	540716.8049	6318135.4028
$\mathbf{M2_1}$	540699.0011	6318151.6016	540700.7944	6318153.6128
$\mathbf{M2_2}$	540703.3778	6318157.1424	540705.7803	6318158.7474
$\mathbf{M2_3}$	540702.8725	6318163.9686	540705.8794	6318166.0641
$\mathbf{M2_4}$	Corrupted GPS Data			
$\mathbf{M2_5}$	540689.8986	6318163.6962	540691.0974	6318166.3118
S1	540628.5068	6318209.3599	540631.3205	6318209.6571
S3	540587.92566	6318341.3625	540590.0211	6318342.6604

Table B.3. Spacial coordinates of the beginning and end of the cross-sections during high-flow conditions.

	Left Bank		Right Bank	
	Easting	**Northing**	**Easting**	**Northing**
$\mathbf{M1_5}$	540710.3611	6318131.1958	540707.7591	6318126.7331
$\mathbf{M2_1}$	540685.5889	6318140.7521	540689.0020	6318144.5918
$\mathbf{M2_2}$	540698.2636	6318151.7913	540702.0678	6318154.4223
$\mathbf{M2_3}$	540702.0500	6318162.6350	540706.2097	6318165.7282
$\mathbf{M2_4}$	540689.8552	6318163.7550	540691.6151	6318167.3992
$\mathbf{M2_5}$	540677.2517	6318156.3777	540680.0959	6318159.5775

B.6 Chosen methods and Discharge Results

Table B.4. Methods and values selected to estimate discharge in the Top, Bottom, and Edge of the cross sections, and discharge, for low-flow conditions.

	Top Discharge	**Bottom Discharge**		**Edge Discharge**		**Discharge $[m^3/s]$**
	Method	**Method**	**Power Coefficient**	**Left Type**	**Right Type**	
$\mathbf{M1_1}$	Constant	No Slip	0.3685	Triangular	Triangular	0.720
$\mathbf{M1_2}$	Constant	No Slip	0.3040	Triangular	Triangular	0.715
$\mathbf{M1_3}$	Constant	No Slip	0.1677	Triangular	Triangular	0.805
$\mathbf{M1_4}$	Constant	No Slip	0.1460	Triangular	Triangular	0.752
$\mathbf{M1_5}$	Constant	No Slip	0.2606	Triangular	Triangular	0.720
$\mathbf{M2_1}$	Constant	No Slip	0.1667	Triangular	Triangular	0.645
$\mathbf{M2_2}$	Constant	No Slip	0.1667	Triangular	Triangular	0.798
$\mathbf{M2_3}$	Constant	No Slip	0.1667	Triangular	Triangular	0.744
$\mathbf{M2_4}$	Constant	No Slip	0.2424	Triangular	Square	0.740
$\mathbf{M2_5}$	Constant	No Slip	0.1667	Triangular	Triangular	0.670
S1	Constant	No Slip	0.2053	Triangular	Triangular	0.750
S3	Constant	No Slip	0.3825	Triangular	Triangular	0.774

Table B.5. Methods and values selected to estimate discharge in the Top, Bottom, and Edge of the cross sections, and discharge, for high-flow conditions.

	Top Discharge	**Bottom Discharge**		**Edge Discharge**		**Discharge $[m^3/s]$**
	Method	**Method**	**Power Coefficient**	**Left Type**	**Right Type**	
$\mathbf{M1_5}$	Constant	No Slip	0.3459	Triangular	Triangular	1.524
$\mathbf{M2_1}$	Constant	No Slip	0.1667	Triangular	Triangular	1.506
$\mathbf{M2_2}$	Constant	No Slip	0.2915	Triangular	Triangular	1.381
$\mathbf{M2_3}$	Constant	No Slip	0.1667	Triangular	Triangular	1.421
$\mathbf{M2_4}$	Power	Power	0.0500	Triangular	Triangular	1.426
$\mathbf{M2_5}$	Constant	No Slip	0.1498	Triangular	Triangular	1.504

C ADCP Bathymetry and Velocity Results

The following appendix includes a description of the methods used to process the bathymetry and velocity data from the ADCP. The methods applied by the software Velocity Mapping Toolbox (VMT) for the processing of the cross-sectional data are described.

Besides, a collection of figures of the bathymetries and velocities measurements done both by ADCP and propeller current meter methods are presented.

C.1 Data processing with Velocity Mapping Toolbox

The Velocity Mapping Toolbox (VMT) is a Matlab-based software developed by U.S. Geological Survey (USGS). It allows the processing and visualization of ADCP data collected along transects in rivers [Parsons et al., 2013]. The routines presented in the software permit the generation of a unique depiction of the 3-D velocity profile from multiple ADCP transect data.

VMT is capable of reading ASCII files of ADCP data exported from WinRiver II, software provided by the ADCP manufacturer TeledyneMarine [2022]. For each single cross-section, a group of repeat transects can be imported into VMT. For computational proposes, VMT only utilizes the measured velocity data from ADCP, and it does not account for unmeasured areas near the surface, banks or bed, and no attempts to extrapolate these missing data are done. Once the transects belonging to a cross-section are loaded to VMT, the following computational steps are performed automatically.

Firstly, the mean cross-section orientation is calculated from the cloud to points. There are two possible methods to define the orientation of the cross-section onto which data for individual transects will be mapped. The former consists of fitting the GPS position of the ensembles to the best-fit linear pattern using the least squares regression method. On the other hand, the latter consists of using user-supplied UTM coordinates for the endpoints of the cross-section.

Secondly, the data from individual transects are projected onto the generated bets fitting plane. An orthogonal projection of the velocity data from irregular transects onto the straight-line plane of the cross-section is performed. The projected coordinates (X_{proj} and Y_{proj}) of a point on the mean cross-section for a point originally located at (X, Y) are given by Equations C.1 and C.2.

$$X_{proj} = \frac{X - mb + mY}{m^2 + 1} \tag{C.1}$$

$$Y_{proj} = \frac{b + mX + m^2Y}{m^2 + 1} \tag{C.2}$$

Where m and b are the slope and intercept of the cross-section line. The projection is performed for every transect loaded into VMT for the cross-section under analysis.

The following step consists of the linear interpolation of the projected data from individual transects into a user-defined grid node in the cross-section. Utilizing the median plus one standard deviation of the projected ensemble spacing along the cross-section for all the transects, VMT computes the recommended minimum grid node spacing. A visualization example of two transects treated with VMT for cross-section M_1 of Binderup Å is displayed in Figure C.1.

Finally, using the projected and interpolated data from all transects, a simple arithmetic mean is applied to obtain a composite representation of the properties at the cross-section. Afterwards, velocity components in Earth coordinates are rotated into components in the plane of the cross-section. In this way, the final velocity components, acoustic backscatter and bed depth are obtained.

After performing the described routine, data can be extracted in the form of an Excel Spreadsheet or ASCII files. Besides, VMT presents interesting plotting capabilities of both cross-sectional and plan view velocities distribution.

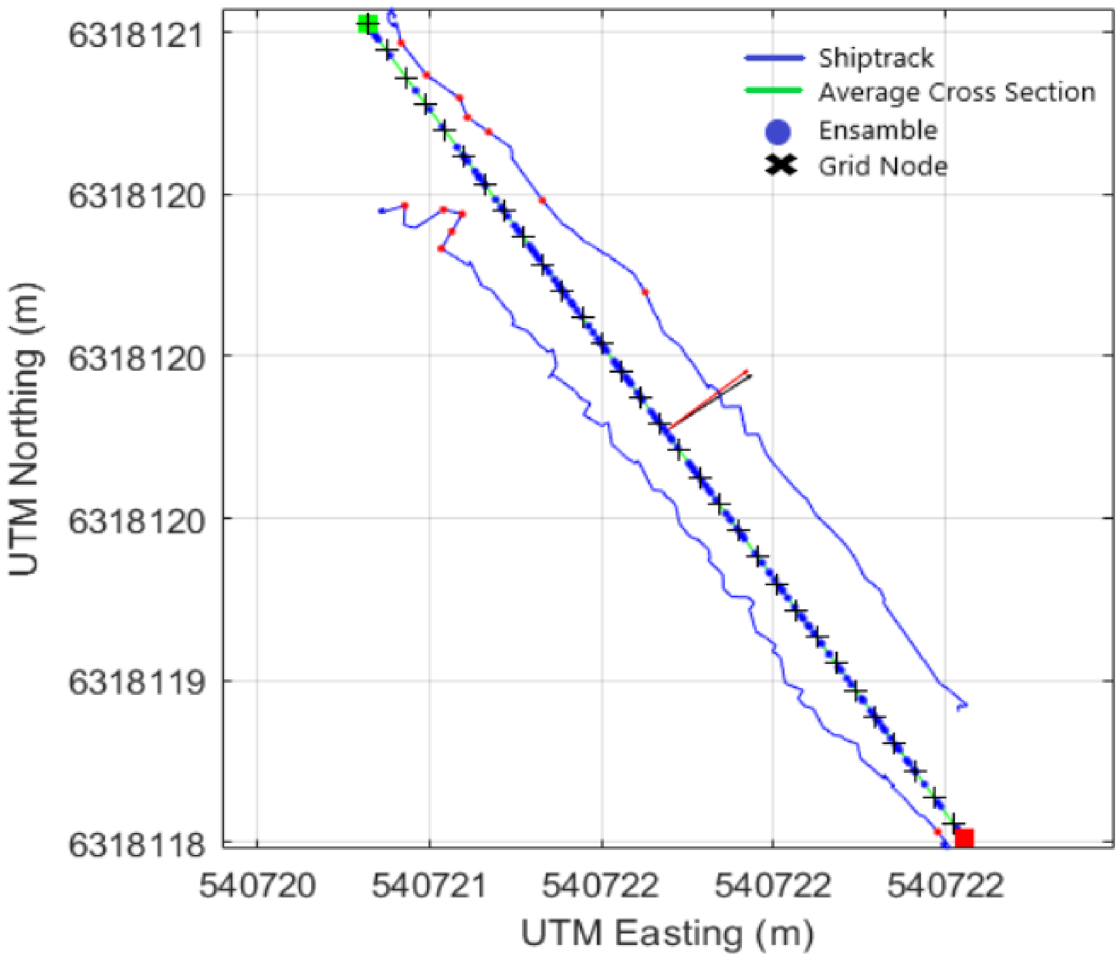

Figure C.1. Example of two ADCP transects from $M1_1$ of Binderup Å mapped to an average cross-section line in the VMT averaging procedure. Cross-section line (green line); ship tracks (blue lines); projected ensembles (blue circles); uniform mean cross-section grid nodes (black 'x').

C.2 Measured bathymetries

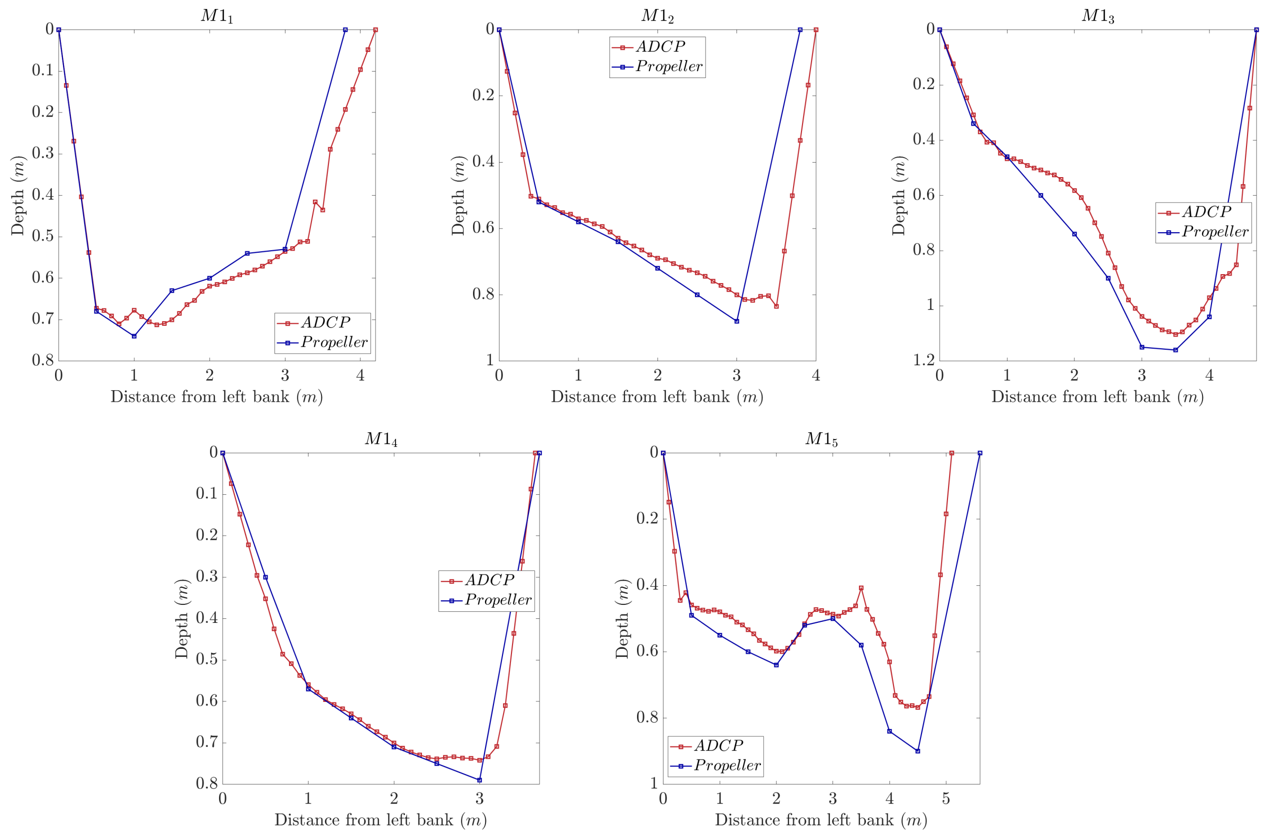

Figure C.2. Measured bathymetry with ADCP and propeller method for cross-sections $M1_1$, $M1_2$, $M1_3$, $M1_4$, $M1_5$ located in the first meander.

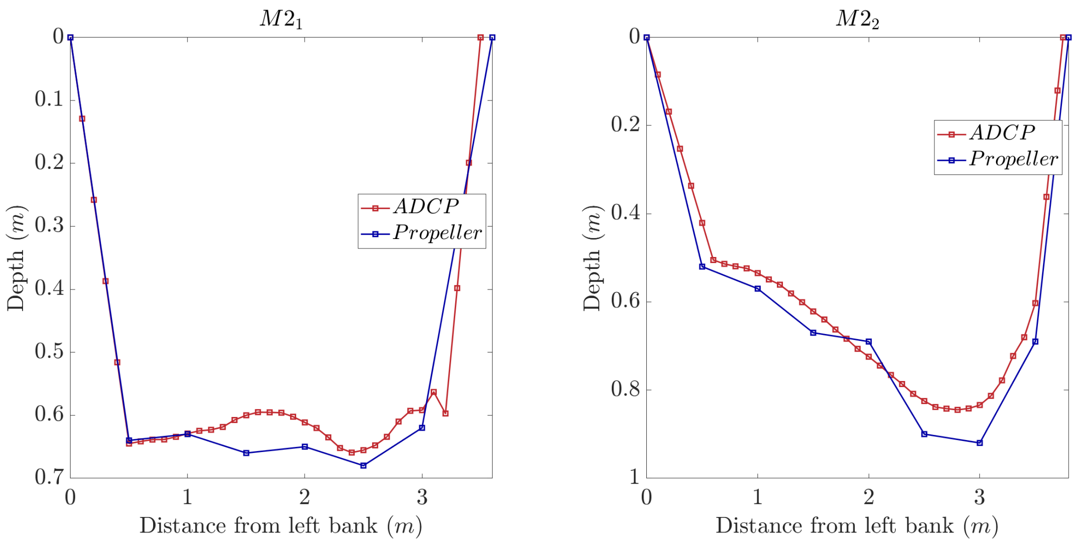

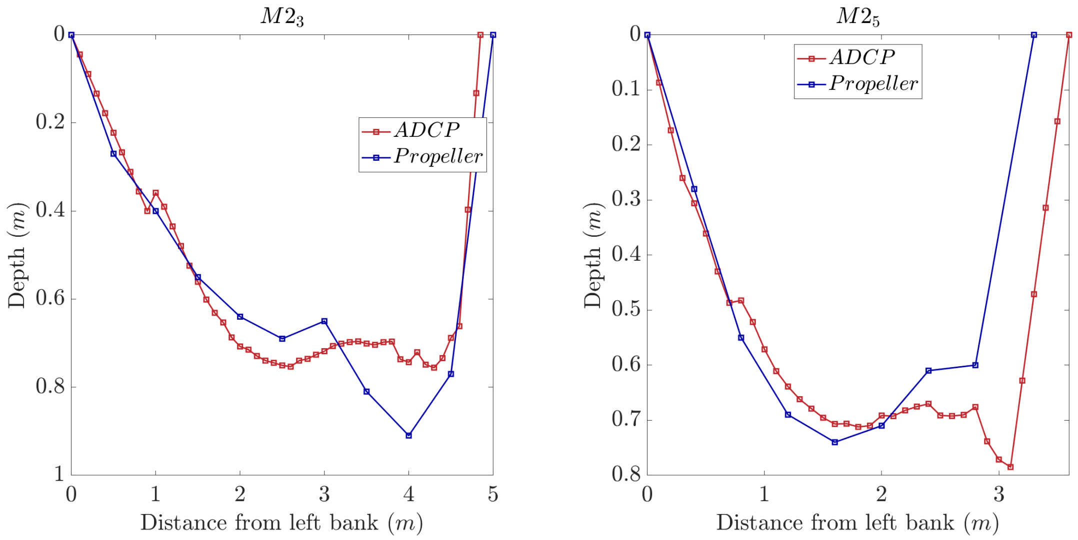

Figure C.2. Measured bathymetry with ADCP and propeller method for cross-sections $M2_1$, $M2_2$, $M2_3$, $M2_5$ located in the second meander.

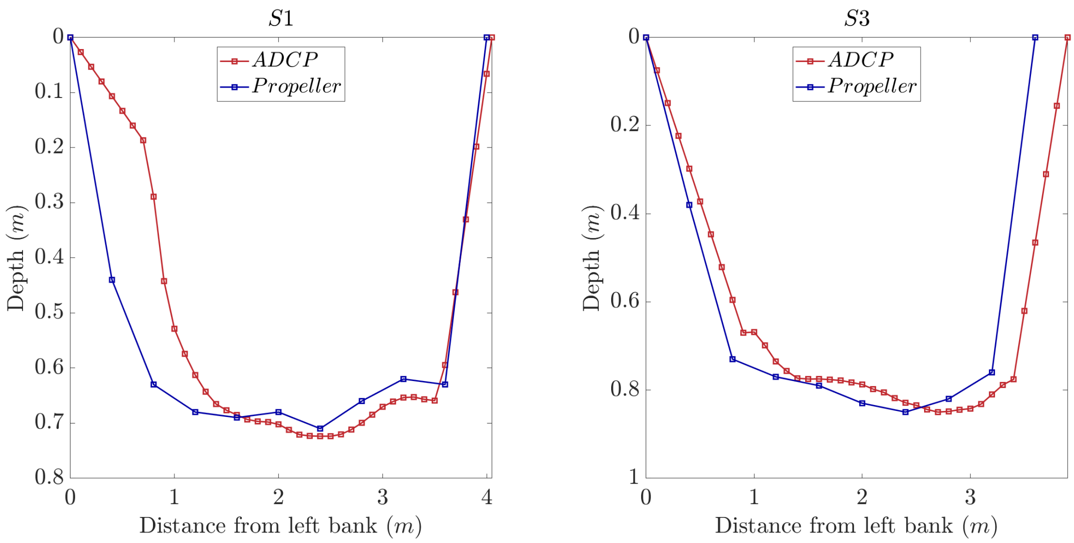

Figure C.3. Measured bathymetry with ADCP and propeller method for cross-sections S1 and S3, located in the straight section.

C.3 Measured velocities

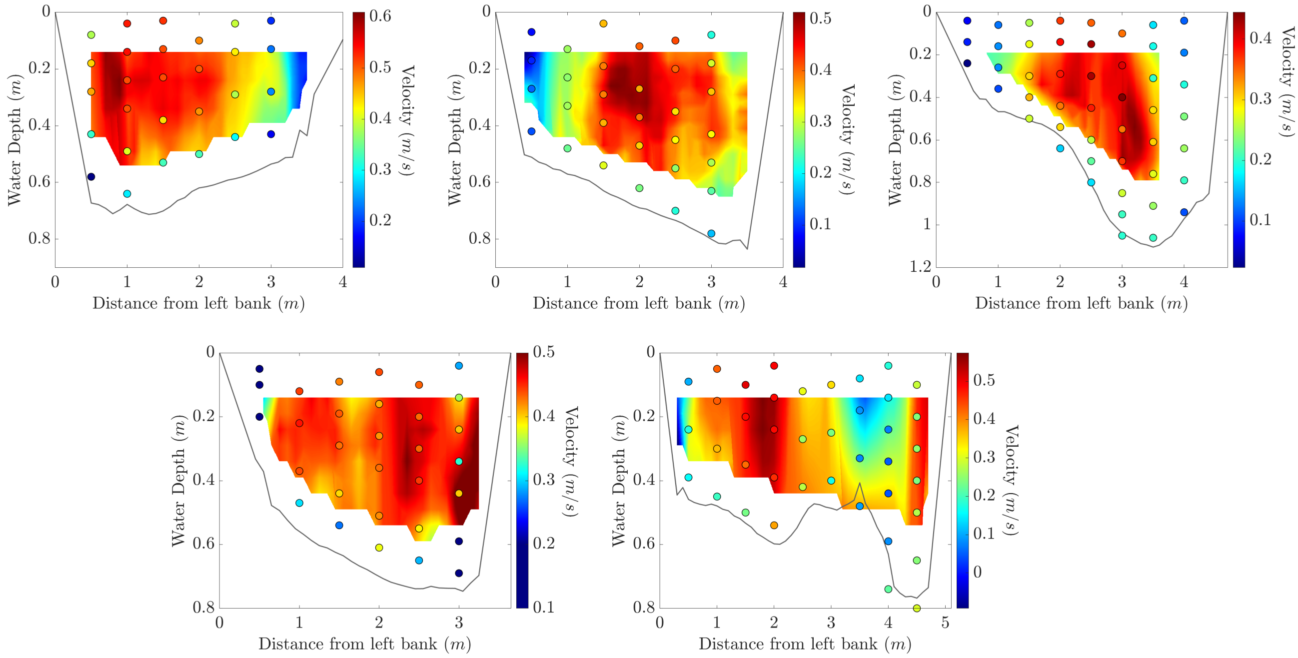

Figure C.4. Measured velocity with ADCP (surface) and propeller (dots) method for cross-sections $M1_1$, $M1_2$, $M1_3$, $M1_4$, $M1_5$ located in the first meander.

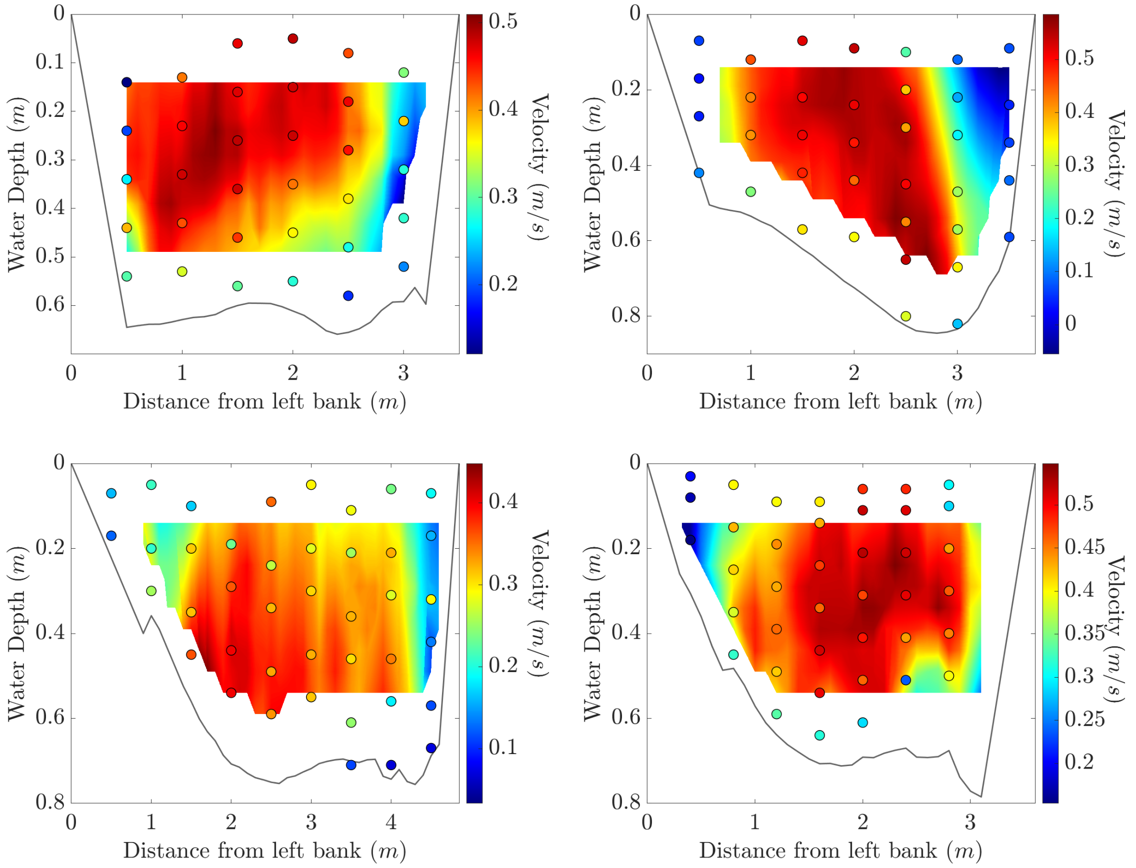

Figure C.5. Measured velocity with ADCP (surface) and propeller (dots) method for cross-sections $M2_1$, $M2_2$, $M2_3$, $M2_5$ located in the second meander.

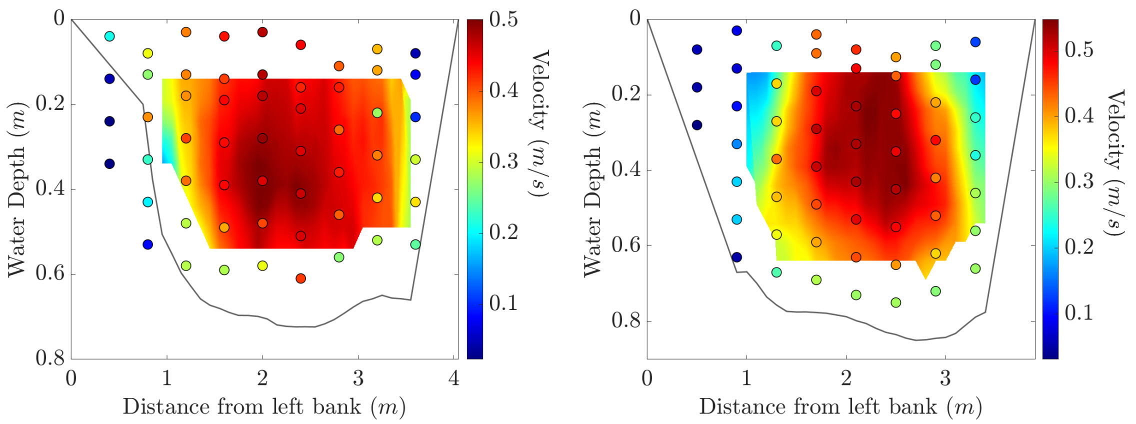

Figure C.6. Measured velocity with ADCP (surface) and propeller (dots) method for cross-sections S1 and S3, located in the straight section.

D Methods Comparison Data

This appendix contains the data used for the flow, geometry and velocity distribution coefficient comparison in Chapter 5.

Table D.1. Discharge data obtained with the propeller current meter and ADCP methods at Binderup Å.

	Propeller Disch. $[m^3/sec]$	**ADCP Disch.** $[m^3/sec]$
$\mathbf{M1_1}$	0.675	0.720
$\mathbf{M1_2}$	0.596	0.715
$\mathbf{M1_3}$	0.790	0.805
$\mathbf{M1_4}$	0.644	0.752
$\mathbf{M1_5}$	0.745	0.720
$\mathbf{M2_1}$	0.639	0.645
$\mathbf{M2_2}$	0.689	0.798
$\mathbf{M2_3}$	0.665	0.744
$\mathbf{M2_4}$	0.643	0.740
$\mathbf{M2_5}$	0.641	0.670
S1	0.700	0.750
S3	0.740	0.774

Table D.2. Calculated cross-sectional area (A), wetted perimeter (P) and hydraulic radius (R) with propeller and ADCP data.

	Propeller			**ADCP**		
	A $[m^2]$	**P** $[m]$	**R** $[m]$	**A** $[m^2]$	**P** $[m]$	**R** $[m]$
$\mathbf{M1_1}$	1.94	4.32	0.45	2.15	4.74	0.45
$\mathbf{M1_2}$	2.20	4.44	0.50	2.40	4.74	0.51
$\mathbf{M1_3}$	3.30	5.51	0.60	3.16	5.58	0.57
$\mathbf{M1_4}$	1.96	4.22	0.46	2.01	4.22	0.48
$\mathbf{M1_5}$	3.08	6.22	0.50	2.62	5.92	0.44
$\mathbf{M2_1}$	1.97	4.18	0.47	1.92	4.21	0.46
$\mathbf{M2_2}$	2.41	4.58	0.53	2.24	4.43	0.51
$\mathbf{M2_3}$	2.85	5.59	0.51	2.73	5.50	0.50
$\mathbf{M2_5}$	1.70	3.79	0.45	1.98	4.26	0.47
S1	2.30	4.59	0.50	2.07	4.58	0.45
S3	2.37	4.35	0.54	2.47	4.57	0.54

Table D.3. Velocity distribution coefficient (α) obtained with the propeller current meter and ADCP data.

	Propeller $\boldsymbol{\alpha}$	**ADCP** $\boldsymbol{\alpha}$
$\mathbf{M1_1}$	1.29	1.14
$\mathbf{M1_2}$	1.28	1.19
$\mathbf{M1_3}$	1.49	1.21
$\mathbf{M1_4}$	1.28	1.02
$\mathbf{M1_5}$	1.80	1.38
$\mathbf{M2_1}$	1.33	1.23
$\mathbf{M2_2}$	1.91	1.43
$\mathbf{M2_3}$	1.36	1.11
$\mathbf{M2_5}$	1.14	1.07
S1	1.39	1.08
S3	1.53	1.20

E HEC-RAS Theoretical Basis for 1-D hydrodynamic calculations

This appendix describes the methodologies used in performing the one-dimensional steady flow calculations by HEC-RAS. The basic equations are presented, and the solution schemes for them are described.

E.1 Equations for Basic Profile Calculations

Water surface profiles are computed from one cross-section to the next by solving the Energy equation, as shown in Equation E.1, with an iterative procedure called the standard step method. A schematic view of the energy change between two cross-sections is displayed in Figure E.1.

$$Z_2 + Y_2 + \frac{\alpha_2 V_2^2}{2g} = Z_1 + Y_1 + \frac{\alpha_1 V_1^2}{2g} + h_e \tag{E.1}$$

Where:

$Z_{1,2}$	elevation of the main channel inverts.
$Y_{1,2}$	depth of water at cross sections
$V_{1,2}$	average velocities
$\alpha_{1,2}$	velocity weighting coefficients
g	gravitation acceleration
h_e	energy head loss

The energy head loss between two cross sections is comprised of friction losses and contraction or expansion losses. The equation for the energy head loss is as follows:

$$h_e = L\bar{S_f} + C\left(\frac{\alpha_2 V_2^2}{2g} - \frac{\alpha_1 V_1^2}{2g}\right) \tag{E.2}$$

Where:

L	discharge weighted reach length.
$\bar{S_f}$	representative friction slope between two sections.
C	expansion or contraction loss coefficient.

The distance weighted reach length (L) is calculated as:

$$L = \frac{L_{lob}\bar{Q_{lob}} + L_{ch}\bar{Q_{ch}} + L_{rob}\bar{Q_{rob}}}{\bar{Q_{lob}} + \bar{Q_{ch}} + \bar{Q_{rob}}} \tag{E.3}$$

Where:

L	cross-section reach lengths specified for flow in the left overbank, main channel, and right overbank.
$\bar{Q}$	arithmetic average of the flows between sections for the left overbank, main channel, and right overbank, respectively

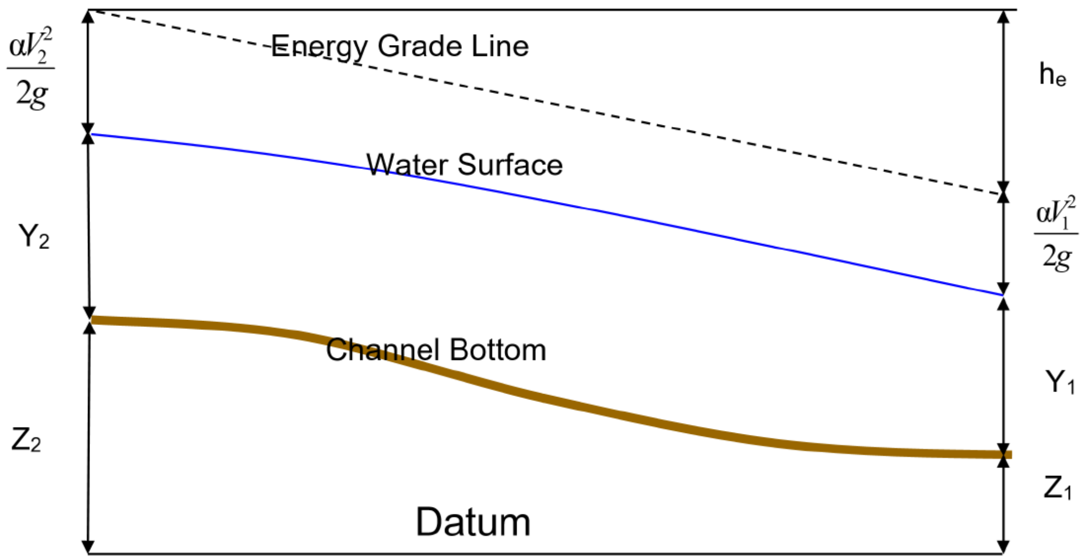

Figure E.1. Schematic view of the change in energy line between two cross-sections. Extracted from US Army Corps of Engineers [2022].

E.2 Cross-Section Subdivision for Conveyance Calculations

The determination of total conveyance and the velocity coefficient in HEC-RAS requires that flow be divided into units for which the velocity is uniformly distributed, as displayed in Figure E.2. The over-bank areas are subdivided using the input cross-section n-value breakpoints as the basis for subdivision. Conveyance is calculated within each subdivision as shown in Equation E.5. The program sums up all the incremental conveyances in the over banks to obtain a conveyance for the left overbank and the right overbank. The main channel conveyance is normally computed as a single conveyance element. The total conveyance for the cross-section is obtained by summing the three subdivision conveyances (left, channel, and right).

$$Q = KS_f^{1/2} \tag{E.4}$$

$$K = \frac{1}{n}AR^{2/3} \tag{E.5}$$

Where:

K	conveyance for subdivision.
n	Manning's roughness coefficient for subdivision.
A	Flow area for the subdivision.
R	Hydraulic radius for the subdivision.
S_f	Slope of the energy grade line.

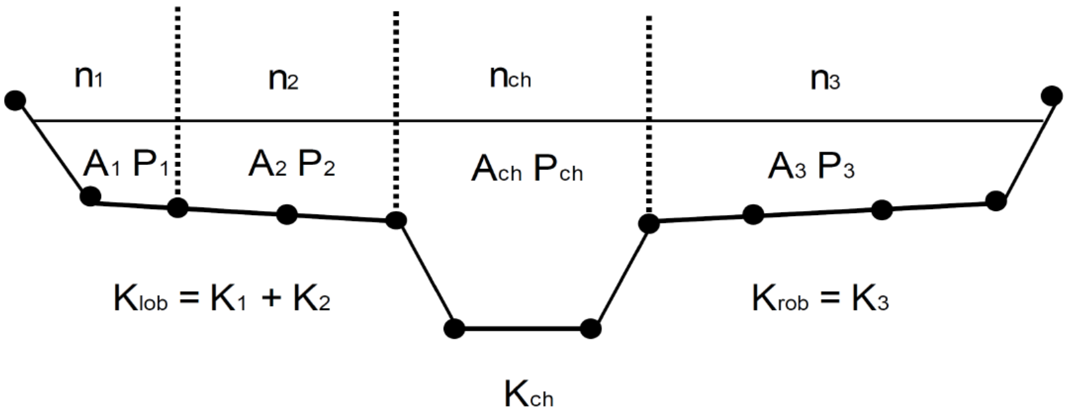

Figure E.2. Cross-section division for the conveyance calculations. Extracted from US Army Corps of Engineers [2022].

E.3 Evaluation of the Mean Kinetic Energy Head

Within the 1D river reach segments, only a single water surface and, therefore, a single mean energy is computed at each cross-section. For a given water surface elevation, the mean energy is obtained by computing flow-weighted energy from the three subsections of a cross-section (left overbank, main channel, and right overbank). In order to compute the mean kinetic energy, it is necessary to obtain the velocity head weighting coefficient (α). The velocity coefficient is computed based on the conveyance in the three flow elements: left overbank, right overbank, and channel, accordingly to Equation E.6.

$$\alpha = \frac{(A_t^2)\left[\frac{K_{lob}^3}{A_{lob}^2} + \frac{K_{ch}^3}{A_{ch}^2} + \frac{K_{rob}^3}{A_{rob}^2}\right]}{K_t^3} \tag{E.6}$$

Where:

A_t	Total flow area of the cross-section.
$A_{lob,ch,rob}$	Flow areas of left overbank, main channel and right overbank, respectively.
K_t	Total conveyance of the cross-section.
$K_{lob,ch,rob}$	Conveyances of left overbank, main channel and right overbank.

E.4 Friction Loss Evaluation

Friction loss is evaluated in HEC-RAS as the product of $\bar{S_f}$ and L, where $\bar{S_f}$ is the representative friction slope for a reach, and L is defined by Equation E.3. The friction slope at each cross-section is computed from Manning's equation as follows:

$$S_f = \left(\frac{Q}{K}\right)^2 \tag{E.7}$$

E.5 Computational Procedure

The unknown water surface elevation at a cross-section is determined by an iterative solution of Equation E.1 and Equation E.2. The computational procedure is as follows:

1. Assume a water surface elevation at the upstream cross-section for a sub-critical profile or downstream if a super-critical profile is being calculated.

2. Based on the assumed water surface elevation, determine the total conveyance and velocity head.
3. Compute $\bar{S_f}$ and solve the energy head lost (h_e) with Equation E.2.
4. Solve the energy equation with Equation E.1 for the Water Surface Elevation of the next iteration.
5. Compare the new water surface elevation with the value assumed in step 1 and repeat steps 1 to 5 until the values agree within 0.003 m or other user-defined tolerance.

In the iterative procedure, the criterion used to estimate water surface elevations varies from trial to trial. For the first trial, the water surface is determined by projecting the previous cross-section's water depth onto the current one. In the second trial, the assumed water surface elevation is adjusted by adding 70% of the error from the first trial (computed W.S. - assumed W.S.). For the third and subsequent trials, a "Secant" method is typically used. This method projects the rate of change of the difference between computed and assumed elevations for the previous two trials. The equation for the secant method is as follows:

$$WS_I = WS_{I-1} - Err_{I-1} \times \frac{Assum_{Diff}}{Err_{Diff}} \tag{E.8}$$

Where:

WS_I	New assumed water surface.
WS_{I-1}	The previous iteration's assumed water surface.
WS_{I-2}	The assumed water surface from two previous trials.
Err_{I-2}	The error from two trials previous.
$Assum_{Diff}$	The difference in assumed water surface from the previous two trials. $Assum_{Diff} = WS_{I-2} - WS_{I-1}$
Err_{Diff}	The difference between the previous error and the current error. $Err_{Diff} = Err_{I-2} - Err_{I-1}$

When obtaining a balanced water surface elevation for a cross-section, it's important to check that the elevation is on the correct side of the critical water surface elevation. If it's not, the program assumes critical depth for the cross-section and displays a warning message. It's essential for the program user to understand the reasons for critical depth assumptions, as they can result from reach lengths being too long or from misrepresentation of effective flow areas of cross sections.

For a subcritical profile, the program checks the Froude number as a preliminary measure to ensure a proper flow regime. The Froude number of the balanced water surface is calculated for both the main channel and the entire cross-section. If either of these numbers is greater than 0.94, the program calculates critical depth using the minimum specific energy method. A Froude number of 0.94 is used instead of 1.0 because the calculation of the Froude number in irregular channels is not accurate.

For a supercritical profile, critical depth is automatically calculated for every cross-section, allowing for a direct comparison between balanced and critical elevations.

The critical water surface elevation is the elevation for which the total energy head is minimum. Defining the total energy head as follows:

$$H = WS + \frac{\alpha V^2}{2g} \tag{E.9}$$

Where:

H	Total energy head.
WS	Water surface elevation.
$\frac{\alpha V^2}{2g}$	Velocity head.

E.6 Applications of the Momentum Equation

When the water surface goes through critical depth, the energy equation is invalid. The energy equation only works for gradually varied flow situations, and the shift from subcritical to supercritical or vice versa is a rapidly changing flow situation. There are several situations where this can happen, such as significant changes in channel slope, bridge constrictions, drop structures and weirs, and stream junctions. Empirical equations can be used in some of these cases, while in others, the momentum equation must be used to obtain a solution. HEC-RAS uses the momentum equation for specific problems, such as hydraulic jumps, low-flow hydraulics at bridges, and stream junctions.

The momentum equation is derived from Newton's second law of motion:

$$\sum F_x = ma \tag{E.10}$$

For a body of water moving between two cross sections, that equation can be written as:

$$P_2 - P_1 + W_x - F_F = Q\rho\Delta V_x \tag{E.11}$$

Where:

P	Hydrostatic pressure force at locations 1 and 2.
W_x	Force due to the weight of water in the X direction.
F_f	Force due to external friction losses from 2 and 1.
Q	Discharge.
ρ	Density of water.
ΔV_z	Change on velocity from 2 to 1 in the X direction.

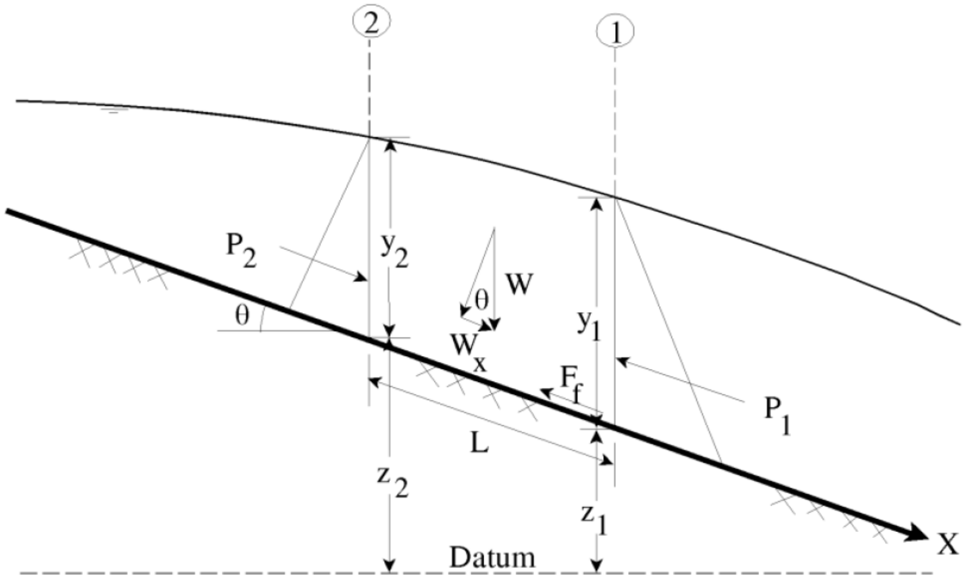

Figure E.3. Schematic representation of the forces involved in the momentum equation calculations. Extracted from US Army Corps of Engineers [2022].

E.7 1-D Steady Flow Program Limitations

The following assumptions are implicit in the analytical expressions used in 1-D steady flow in HEC-RAS:

1. Flow is steady.
2. Flow is gradually varied. (Except at hydraulic structures such as: bridges; culverts; and weirs. At these locations, where the flow can be rapidly varied, the momentum equation is used.)
3. Flow is one-dimensional.
4. River channels have "small" slopes, less than 1:10.

F Star CCM+ Model Setup & Results

- Two-layer All y+ Wall Treatment
- Gradients
- Segregated Flow
- Implicit Unsteady
- Solution interpolation
- VOF Waves Zone Distance
- VOF Waves
- Gravity
- Wall distance
- Realizable K-Epsilon Two-Layer
- Reynolds-Averaged Navier Stokes
- Turbulent
- Volume of Fluid (VOF)
- Multi-phase Interaction
- Multi-phase
- Three Dimensional

F.1 Mesh Discretization

Table F.1. Total Cell Count and Surface Area Comparison for Inner and Outer Banks Across Different Geometries

Curvatures	**C=0**		**C=0.31**		**C=0.63**	
Banks	Inner	Outer	Inner	Outer	Inner	Outer
Surface Area [m^2]	6.2645		5.6519	6.3206	5.5059	7.0335
The total amount of cells	962828		908809		783535	

F.2 Steady State and boundary impact analysis

Water surface slope along inlet channel

The water surface elevation along the centerline of the inlet channel for each model;

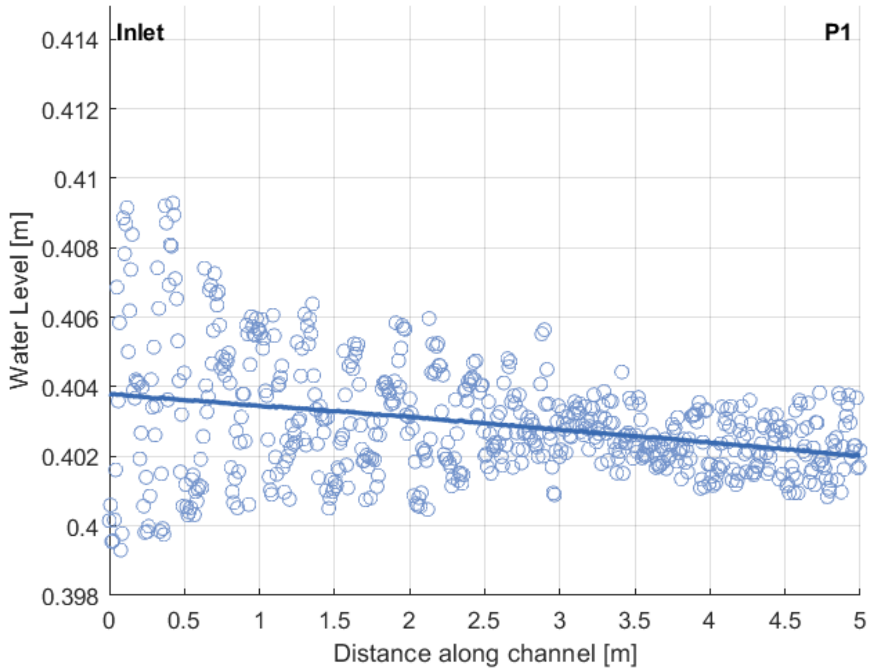

Figure F.1. Water surface elevation along centerline of inlet channel, model C = 0.00

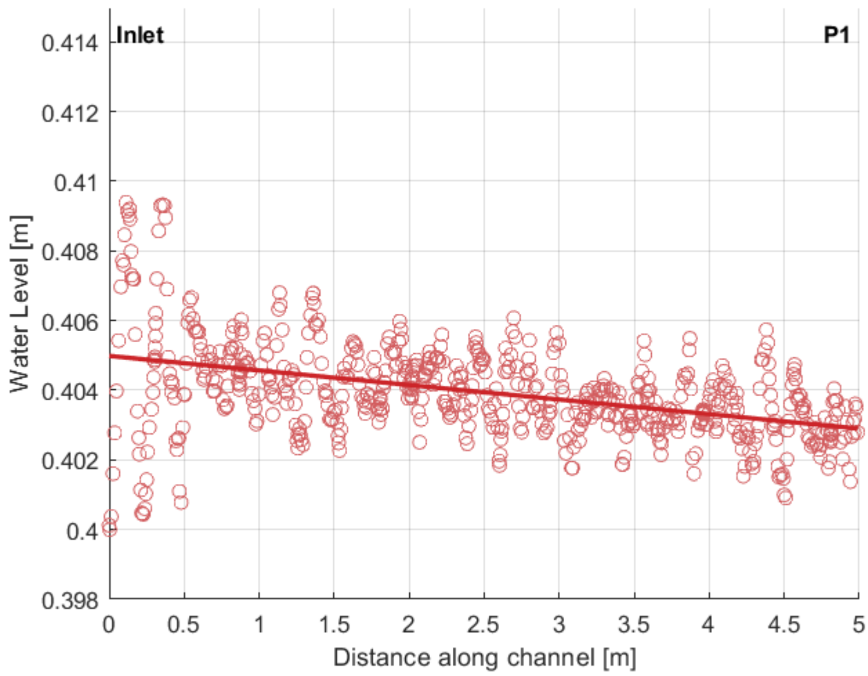

Figure F.2. Water surface elevation along centerline of inlet channel, model C = 0.31.

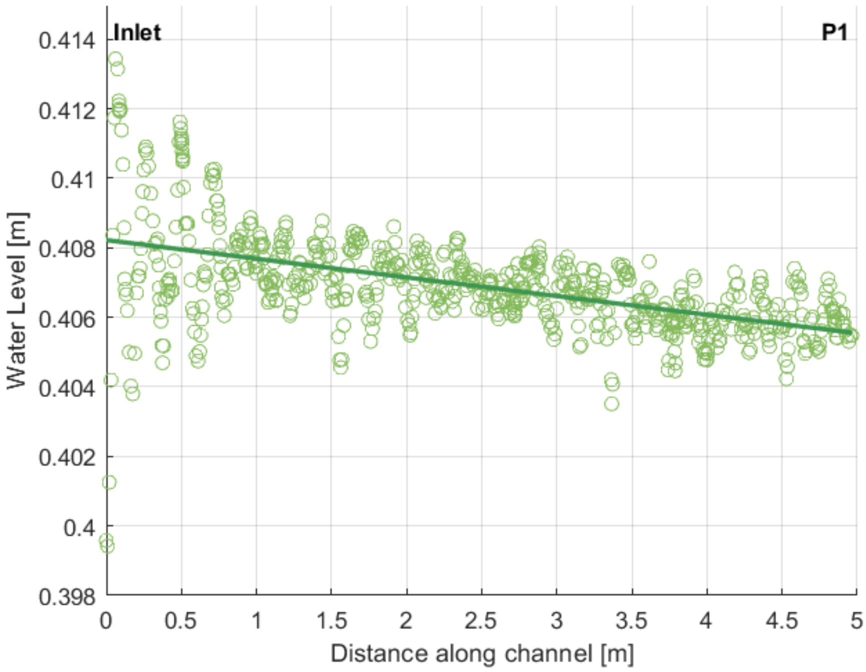

Figure F.3. Water surface elevation along centerline of inlet channel, model C = 0.63.

In each of the models, an initial unsteady period lasting approximately the first two meters is clearly visible, after which the surface reaches a state of relative steadiness.

F.3 Electronic appendix

The full collection of velocity profiles of the planes in the inlet and outlet channels can be found in the electronically attached file.

From Pi1 to Pi5 in all models the velocity profile can be seen to develop rapidly along the walls, as well as the initially low velocity at the surface developing to match the central region. In models C = 0.31 and C = 0.63, the development of the higher velocity region towards the inner bank can be seen developing from P9 to Pi11. In the outlet channel, the region of high velocity has shifted to the outer bank, while a region of low velocity has developed at the inner bank.